PHOTOCATALYST ACTIVITY TEST OF TiO_2-ACTIVE CHARCOAL FROM PALM SHELLS FOR DEGRADATION OF SYNTHETIC DYE REMAZOL BRILLIANT BLUE R

THESIS

By:
RANGGA DWI PRAYOGA
NIM. 220603110075

CHEMISTRY DEPARTMENT
SCIENCE AND TECHNOLOGY FACULTY
THE STATE ISLAMIC UNIVERSITY MAULANA MALIK IBRAHIM
MALANG
2026

PHOTOCATALYST ACTIVITY TEST OF TiO_2-ACTIVE CHARCOAL FROM PALM SHELLS FOR DEGRADATION OF SYNTHETIC DYE REMAZOL BRILLIANT BLUE R

THESIS

By:
RANGGA DWI PRAYOGA
NIM. 220603110075

A Thesis Submitted to:
The Science and Technology Faculty,
The State Islamic University of Malang, in Partial Fulfillment of
The Requirements for the Degree of
Bachelor of Science (S.Si)

CHEMISTRY DEPARTMENT
SCIENCE AND TECHNOLOGY FACULTY
THE STATE ISLAMIC UNIVERSITY MAULANA MALIK IBRAHIM
MALANG
2026

PHOTOCATALYST ACTIVITY TEST OF TiO_2-ACTIVE CHARCOAL FROM PALM SHELLS FOR DEGRADATION OF SYNTHETIC DYE REMAZOL BRILLIANT BLUE R

THESIS

By:
RANGGA DWI PRAYOGA
NIM. 220603110075

Approved By:
Date: 22, May, 2026

Supervisor I	Supervisor II
Lulu'atul Hamidatu Ulya, M.Sc	A. Ghanaim Fasya, M.Si
NIP. 19900906 202321 2 033	NIP. 19820616 200604 1 002

Acknowledged
Head of Chemistry Department

A. Ghanaim Fasya, M.Si
NIP. 19820616 200604 1 002

PHOTOCATALYST ACTIVITY TEST OF TiO_2-ACTIVE CHARCOAL FROM PALM SHELLS FOR DEGRADATION OF SYNTHETIC DYE REMAZOL BRILLIANT BLUE R

THESIS

By:
RANGGA DWI PRAYOGA
NIM. 220603110075

Has Been Examined by Committee Member of Examiner as The Requirements for the Degree of Bachelor of Science (S.Si)
Date: 06, June, 2026

Head Examiner	:	**Dr. Suci Amalia, M.Sc** **NIP. 19821104 200901 2 007**	(.....)
Examiner Member I	:	**Lilik Miftahul Khoiroh, M.Si** **NIP. 19831226 201903 2 008**	(.....)
Examiner Member II	:	**Lulu'atul Hamidatu Ulya, M.Sc** **NIP. 19900906 202321 2 033**	(.....)
Examiner Member III	:	**A. Ghanaim Fasya, M.Si** **NIP. 19820616 200604 1 002**	(.....)

Approved by,
Head of Chemistry Department

A. Ghanaim Fasya, M.Si
NIP. 19820616 200604 1 002

MOTTO

"وَعَسٰٓى اَنْ تَكْرَهُوْا شَيْـًٔا وَّهُوَ خَيْرٌ لَّكُمْۚ وَعَسٰٓى اَنْ تُحِبُّوْا شَيْـًٔا وَّهُوَ شَرٌّ لَّكُمْۗ وَاللّٰهُ يَعْلَمُ وَاَنْتُمْ لَا تَعْلَمُوْنَ"

“But perhaps you hate a thing, and it is good for you, and perhaps you love a thing, and it is bad for you. Allah knows, while you know not.”

— (Surah Al baqarah [2:216])

"Life's simple. You make choices, and you don't look back."

— Han Lue, *The Fast and the Furious: Tokyo Drift*

"Jangan bandingkan jarak terbangnya, tapi bagaimana dan apa yang dilaluinya”

"Do not compare how far it flies, but rather the journey it has gone through."

— *Pesawat Kertas 365 Hari*, JKT48

"Les soldats batailleront et Dieu donnera la victoire."

"The soldiers will fight, and God will give the victory."

— Joan of Arc

DEDICATION PAGE

To Mom, Wakinianti
Thank you for always being the calmest haven for me.
Ever since I was little, you've always been firm. You'd often get angry when I made mistakes, and that used to scare me back then. But the more I grew up, the more I realized that behind that firmness lay such immense love. You never forced me to be someone else. You always let me try many things, choose my own path, and always supported me as long as it was good for me. I still remember the first time I went to a school far away and had to live in a dormitory. You looked strong, but your eyes were teary. To this day, that remains the warmest form of love I've ever felt. And funny enough, even though I'm in my twenties now, I still want to be pampered by you. I ask to be fed when I come home, and Mom always complies without ever thinking I'm too grown up for that. If I had to describe Mom, maybe she's like the atmosphere of dawn. Calm, warm, and always giving strength to get through the day. Sometimes people wake up late and miss the beauty of the morning, just like sometimes I'm late in realizing how precious Mom is in my life.

To Dad, Samikun
Thank you for loving me in ways that aren't often spoken.
Dad isn't the type who's good at expressing feelings with words. But from Dad's hard work and sacrifices, I know how deep that love is. I know there are many things Dad gave up so I could go to school this far, even when it meant sacrificing many of the things Dad had. I still remember Dad's words that have stayed with me to this day: "Study hard; once you're successful, what matters most is that you're happy." That simple sentence always feels heavy to me. I might rarely say it directly because of pride, but I love Dad so much. And as time keeps moving forward, deep down, I just want Dad to stay by my side a little longer.

To my older and younger siblings, Siti Zulaikah & Izatul
Thank you for always being the warmest part of our home.
We often joke around, and we fight too, but we always come back to talking like nothing happened. There are so many simple moments that turned out to mean so much to me, having coffee in front of the house, walking together, eating while sharing random stories about anything and everything. To my older sibling, thank you for always being a place where I can share my stories without being judged. Even though I'm often too proud to open up, I know there's always a place to come home to and be heard.

To the friends
Honorable Mention: Eva, Meli, Hanik, Izzud, Karis, Hilmy, All *Member Pemuda Introvert, Kimia Lanang* and Member of *Wacana Tanpa Acara.*
Thank you to all of you, I can't name each of you individually, who were there during my college years, especially during these exhausting final days. Thank you for sticking around. Amid revisions, research, and the urge to give up, you made everything feel lighter. With you, I can be myself without having to wear any masks. Thank you for listening, for calling me out, for being there, and for sticking with me this far in life.

And finally, to myself.
Thank you for hanging in there until today.
I know this journey hasn't been easy. I've felt out of place, I've been disappointed in life, and I've been afraid of failing and falling behind others. But it turns out I've managed to get through it all, bit by bit. I'm proud that I've kept going, kept trying, and kept being brave enough to be myself even though not everyone likes it. If one day I feel tired again, I hope I remember that the person I am today has managed to get through many things that once felt impossible. And that's more than enough to be proud of.

x

ORIGINALITY STATEMENT

I, Rangga Dwi Prayoga, hereby declare that this thesis and the work reported herein were composed by and originated entirely from me. I certify that my thesis does not infringe upon anyone's copyright nor violate any proprietary rights and that any ideas, techniques, quotations, or any other material from the work of other people. Information derived from the published and unpublished work of others has been acknowledged in the text, and references are given in the list of sources.

Malang, April 20, 2025

The Author

Rangga Dwi Prayoga

NIM. 220603110075

ACKNOWLEDGEMENT

All praise and gratitude are due to Allah Swt. for His mercy, guidance, and blessings. By His grace, the author has been able to complete this undergraduate thesis entitled **"Photocatalyst Activity Test of TiO_2-Active Charcoal from Palm Shells for Degradation of Synthetic Dye Remazol Brilliant Blue R."** This thesis is submitted as one of the requirements to obtain a Bachelor's degree in Chemistry at the Faculty of Science and Technology, Maulana Malik Ibrahim State Islamic University of Malang.

The journey of completing this thesis was not easy. There were many challenges, difficulties, and moments of doubt. However, through prayers, support, and assistance from many parties, the author accomplished this work. Therefore, with sincere humility, the author would like to express the deepest gratitude to:

1. Prof. Dr. Hj. Ilfi Nur Diana, M.Si, as the Rector of Maulana Malik Ibrahim State Islamic University of Malang.
2. Dr. Agus Mulyono, M.Kes, as the Dean of the Faculty of Science and Technology, UIN Malang.
3. A. Ghanaim Fasya, M.Si., as the Head of the Chemistry Study Program as well as the religious academic advisor, has provided guidance, advice, and spiritual support to the author.
4. Lulu'atul Hamidatu Ulya, M.Sc., as the main thesis supervisor, and also the Academic Advisor who patiently provided guidance, suggestions, and motivation throughout the completion of this thesis.
5. Dr. Suci Amalia, M.Sc., and Lilik Miftahul Khoiroh, M.Si., as the thesis examiners, for their valuable suggestions, constructive criticism, and insightful feedback that greatly improved the quality of this thesis.
6. Isnaeni Hartiningsih, S.Si., as Laboratory Assistant in the Inorganic Chemistry Laboratory, for her assistance, technical support, and guidance during the experiments and laboratory activities throughout this research.
7. All lecturers, laboratory assistants, and administrative staff of the Chemistry Study Program, UIN Malang, for their knowledge, guidance, support, and valuable insights that have significantly contributed to the author's academic and personal development.
8. To the late Susi Nurul Khalifah, M.Si., who served as the author's academic advisor throughout the years of study at the university, for her kindness, guidance, encouragement, and invaluable support. Although she is no longer with us, her dedication and contributions will always be remembered and appreciated by the author.

The author is aware that the preparation and writing of this thesis are not yet perfect. Therefore, the author apologizes to all parties for any errors that may have occurred during the preparation process. Hopefully, this work will be useful and contribute to the readers' knowledge. May this thesis provide benefits, especially for the development of chemistry and environmentally friendly technology.

Malang, April 20, 2025

The Author

TABLE OF CONTENTS

LIST OF FIGURES

LIST OF TABLES

APPENDICES LIST

ABSTRAK

Prayoga. R. D. 2026. ***UJI AKTIVITAS FOTOKATALIS TiO_2-KARBON AKTIF DARI TEMPURUNG KELAPA SAWIT TERHADAP DEGRADASI REMAZOL BRILLIANT BLUE R***. *Skripsi*. Program Studi Kimia, Fakultas Sains dan Teknologi, Universitas Islam Negeri Maulana Malik Ibrahim Malang. Pembimbing I: Lulu'atul Hamidatu Ulya, M.Sc., Pembimbing II: Ahmad Ghanaim Fasya, M.Si.

Kata kunci: *Degradasi, Fotokatalis, Impregnasi, TiO_2-Arang Aktif.*

Pencemaran air akibat limbah industri tekstil merupakan permasalahan lingkungan yang serius, terutama karena keberadaan zat warna sintetis seperti Remazol Brilliant Blue R (RBBR) yang bersifat toksik, stabil, dan sulit terdegradasi secara alami. Senyawa ini dapat menurunkan kualitas air serta membahayakan organisme akuatik dan kesehatan manusia, sehingga diperlukan metode pengolahan yang efektif dan berkelanjutan. Penelitian ini bertujuan untuk mengevaluasi aktivitas fotokatalitik komposit TiO_2-arang aktif dalam mendegradasi RBBR di bawah iradiasi sinar ultraviolet (UV). Arang aktif disintesis melalui proses karbonisasi dan aktivasi kimia untuk meningkatkan luas permukaan dan kapasitas adsorpsi, kemudian TiO_2 diimpregnasikan ke dalam matriks arang aktif guna membentuk material komposit yang sinergis. Karakterisasi material dilakukan menggunakan X-Ray Diffraction (XRD), X-Ray Fluorescence (XRF), Fourier Transform Infrared Spectroscopy (FTIR), dan UV-Visible Diffuse Reflectance Spectroscopy (UV-DRS) untuk mengidentifikasi struktur kristal, komposisi unsur, gugus fungsi. Uji fotodegradasi dilakukan dengan variasi massa fotokatalis 10–50 mg dan konsentrasi awal zat warna 10–50 ppm. Efisiensi degradasi ditentukan berdasarkan penurunan absorbansi menggunakan spektrofotometer UV-Vis. Hasil penelitian menunjukkan bahwa komposit TiO_2-arang aktif berhasil disintesis, ditandai oleh terbentuknya fase anatase TiO_2. Analisis UV-DRS menunjukkan penurunan energi celah pita dari 3,19 eV menjadi 2,89 eV yang mengindikasikan peningkatan kemampuan penyerapan cahaya. Kondisi optimum diperoleh pada massa fotokatalis 30 mg dalam 25 mL larutan dengan efisiensi degradasi 86,07% dan total remediasi 87,52%, sedangkan konsentrasi awal optimum 10 ppm dengan efisiensi degradasi 91,47%. Secara keseluruhan, komposit TiO_2-arang aktif menunjukkan kinerja yang lebih baik dibandingkan TiO_2 murni, arang aktif, maupun sistem tanpa katalis, yang menunjukkan adanya efek sinergis antara adsorpsi dan fotokatalisis dalam meningkatkan degradasi RBBR.

ABSTRACT

Prayoga. R. D. 2026. ***ACTIVITY TEST OF TiO_2-ACTIVATED CARBON FROM PALM SHELLS AS PHOTOCATALYST FOR THE DEGRADATION OF REMAZOL BRILLIANT BLUE R.*** *Thesis*. Department of Chemistry, Faculty of Science and Technology, Maulana Malik Ibrahim State Islamic University, Malang. Consultant Lecturer I: Lulu'atul Hamidatu Ulya, M.Sc., Consultant Lecturer II: Ahmad Ghanaim Fasya, M.Si.

Keywords: *Degradation*, *Photocatalyst, Impregnation, TiO_2-Activated Carbon.*

Water pollution caused by textile industry wastewater is a serious environmental problem, particularly due to the presence of synthetic dyes such as Remazol Brilliant Blue R (RBBR), which are toxic, stable, and difficult to degrade naturally. These compounds reduce water quality and pose risks to aquatic organisms and human health; therefore, effective and sustainable treatment methods are required. This study aimed to evaluate the photocatalytic activity of a TiO_2-activated carbon composite for RBBR degradation under ultraviolet (UV) irradiation. Activated carbon was synthesized through carbonization and chemical activation to enhance its surface area and adsorption capacity, followed by TiO_2 impregnation to form a synergistic composite. Material characterization was conducted using XRD, XRF, FTIR, and UV-DRS. Photodegradation experiments were performed using photocatalyst masses of 10–50 mg and initial dye concentrations of 10–50 ppm. Degradation efficiency was determined from the decrease in absorbance measured by UV-Vis spectrophotometry. The results confirmed the successful synthesis of the TiO_2-activated carbon composite, indicated by the formation of the anatase phase of TiO_2. UV-DRS analysis showed a decrease in band gap energy from 3.19 eV to 2.89 eV, indicating enhanced light absorption. The optimum condition was achieved using 30 mg photocatalyst in 25 mL solution, resulting in a degradation efficiency of 86.07% and total remediation of 87.52%. The optimum initial dye concentration was 10 ppm, with a degradation efficiency of 91.47%. Overall, the TiO_2-activated carbon composite performed better than pure TiO_2, activated carbon, and the system without a catalyst, demonstrating a synergistic effect between adsorption and photocatalysis for RBBR degradation.

مستخلص البحث

فرايوكا.ر.د.٢٠٢٦. **اختبار نشاط المحفز الضوئي TiO_2–الكربون النشط من قشرة جوز نخيل الزيت على تحلل ريمازول بريلينت بلو R**. بحث جامعي. قسم الكيمياء، كلية العلوم والتكنولوجيا، جامعة مولانا مالك إبراهيم الإسلامية الحكومية مالانج. المشرفة الأولى: لؤلؤة الحميدة العليا، الماجستير ، المشرف الثاني: أحمد غنائم فاسيا، الماجستير.

الكلمة الرئيسيات: التحلل، التحفيز الضوئي، التشريب، TiO_2–الفحم النشط.

التلوث المائي الناتج عن نفايات صناعة النسيج يعد مشكلة بيئية خطيرة، خاصة بسبب وجود أصباغ صناعية مثل ريمازول بريليانت بلو آر (RBBR) التي تتميز بالسمية والثبات وصعوبة تحللها طبيعيًا. هذه المركبات يمكن أن تقلل من جودة المياه وتضر بالكائنات المائية وصحة الإنسان، لذا هناك حاجة إلى أساليب معالجة فعالة ومستدامة. تهدف هذه الدراسة إلى تقييم النشاط التحفيزي الضوئي لمركب- TiO_2 الفحم النشط في تحلل RBBR تحت إشعاع الأشعة فوق البنفسجية .(UV) يتم تصنيع الفحم النشط عبر عملية الكربنة والتنشيط الكيميائي لزيادة مساحة السطح وقدرة الامتزاز، ثم يُشرب TiO_2 داخل مصفوفة الفحم النشط لتكوين مادة مركبة متآزرة. تم إجراء توصيف المواد باستخدام حيود الأشعة السينية(XRD) ، وفلورة الأشعة السينية(XRF) ، وطيفية الأشعة تحت الحمراء بتحويل فوريه(FTIR) ، وطيفية الامتصاص المنتشر للأشعة فوق البنفسجية-المرئية (UV-DRS) للتعرف على البنية البلورية، وتركيب العناصر، والمجموعات الوظيفية. تم إجراء اختبار التحلل الضوئي مع تغيّر كتلة المحفز الضوئي من ١٠– ٥٠ ملغ وتركيز أولي لصبغة ١٠–٥٠جزء في المليون. تم تحديد كفاءة التحلل بناءً على انخفاض الامتصاص باستخدام مقياس الطيف الضوئي .UV-Vis أظهرت نتائج البحث أن مركب- TiO_2 الفحم النشط تم تصنيعه بنجاح، وتم تمييز ذلك بتكوّن طور أناتاز TiO_2. تحليل الأشعة فوق البنفسجية-الانعكاس الانتشاري أشَار إلى انخفاض فجوة الطاقة من ٣.١٩إلكترون فولت إلى ٢.٨٩ إلكترون فولت، مما يدل على زيادة قدرة الامتصاص الضوئي. حصلت الظروف المثلى عند كتلة المحفز الضوئي ٣٠ملغ في ٢٥مل من المحلول مع كفاءة تحلل ٨٦.٠٧٪ وإجمالي المعالجة ٨٧.٥٢٪، بينما كانت التركيز الابتدائي الأمثل ١٠جزء في المليون مع كفاءة تحلل ٩١.٤٧٪. بشكل عام، أظهر المركب- TiO_2 الفحم النشط أداءً أفضل مقارنة بـ TiO_2 النقي، الفحم النشط، أو النظام بدون محفز، مما يشير إلى وجود تأثير تكافلي بين الامتزاز والتحفيز الضوئي في تعزيز تحلل RBBR .

CHAPTER I
INTRODUCTION

1.1 Background

The global textile industry is growing rapidly. According to Statista, there are over 1.29 million factories worldwide, with around 660,000 dedicated to garment manufacturing alone. Key textile production has concentrated in Asia, particularly in China, Bangladesh, and Vietnam. Every year, the textile industry continues to grow and develop. With the growth of the textile industry, the use of dyes is increasing. There is no denying that textile dye is the most widely used because it is cheap, durable, and easy to obtain. However, using textile dye can leave harmful residue.

Textile residue is a non-biodegradable compound that can be very harmful to the environment. Especially to the aquatic environment. This matter will disturb the lives of the surrounding community. Allah says in the Quran, Surah ar Rum, verse 41:

ظَهَرَ الْفَسَادُ فِى الْبَرِّ وَالْبَحْرِ بِمَا كَسَبَتْ اَيْدِى النَّاسِ لِيُذِيْقَهُمْ بَعْضَ الَّذِيْ عَمِلُوْا لَعَلَّهُمْ يَرْجِعُوْنَ ﴿٤١﴾

Mean: *"Corruption has appeared throughout the land and sea by [reason of] what the hands of people have earned so He [i.e., Allāh] may let them taste part of [the consequence of] what they have done that perhaps they will return (to righteousness)".* (QS. ar Rum: 41)

The verse above states that humans on this earth have caused significant damage, yet they are unaware of it. Scholars state that the damage in question is damage related to environmental destruction, sin, and moral exploitation (Nurhayati et al., 2018). In the interpretation of Al-Misbah, Surah ar Rum verse 41 describes that damage has been seen on land, such as drought and famine, and at sea in the form of ecological damage, reduced marine yields, sinking fish, and damage to coral reefs, caused by the actions of disobedient humans, so that Allah sends disasters so that they return to His path. The interpretation of the word *fasad* in the verse by contemporary scholars is understood as environmental damage because it includes the words *al-bar* (land) and *al-bahr* (sea). Ibn' Ashur in al-Tahrir wa al-Tanwir also explains that fasad refers to the condition of land and sea damaged by human actions (Shihab, 2002). Environmental pollution caused by the textile industry is a form of human-caused damage. One cause is textile dye waste.

Remazol Brilliant Blue R (RBBR) is a textile dye frequently used in the industry, characterized by its bright, attractive blue colour. However, the use of this dye has the potential to cause environmental pollution. This is because RBBR is a dye that is difficult to decompose naturally. In addition, RBBR can cause cancer development, pose health risks, reduce the amount of dissolved oxygen in water, affect the pH of aquatic environments, and disrupt microorganisms and aquatic organisms (Hidayati et al., 2024).

Conventional dye wastewater treatment is still the main method used in many industrial sectors, especially in the textile industry, which generates large volumes of coloured wastewater. Methods such as coagulation, flocculation, adsorption using activated carbon, and

aerobic or anaerobic biological processes have been widely applied due to their technological availability. However, the effectiveness of these methods in degrading complex dye compounds remains low, especially for synthetic dyes with stable aromatic structures that are resistant to biological degradation. In addition, high operational costs, the need for additional chemicals, and the production of secondary sludge present major challenges that limit their long-term application. The resulting sludge must be further treated to prevent secondary pollution, which ultimately increases both economic and environmental burdens. In the long term, these conventional approaches are considered unsustainable and inconsistent with the principles of the SDGs. Therefore, more efficient, economical, and sustainable alternatives are required to treat industrial dye wastewater. New technologies must be capable of eliminating pollutants without generating harmful by-products (Oko et al., 2022).

Heterogeneous photocatalysis, particularly through photodegradation, is a promising alternative for dye wastewater treatment. This process uses ultraviolet or visible light to activate a semiconductor, generating hydroxyl radicals (•OH) and other reactive species that oxidize organic compounds into harmless substances such as carbon dioxide and water. The main advantage of this process is its ability to destroy harmful organic compounds, in contrast to conventional methods that only transfer or stabilize contaminants. Photocatalysis also operates at ambient temperature and pressure, requires minimal additional chemicals, and does not produce sludge or toxic byproducts. These features make it environmentally friendly and suitable for large-scale applications. The process is also easy to control and can be integrated with existing treatment systems. Given its efficiency and sustainability, photocatalysis is a highly viable option for further development (Siswanti et al., 2023).

Titanium dioxide (TiO_2) is the most widely utilized semiconductor photocatalyst due to its chemical stability, corrosion resistance, and environmental non-toxicity. The anatase phase of TiO_2 exhibits high photocatalytic activity, enabling efficient degradation of a broad range of organic pollutants. Despite these advantages, its relatively small surface area restricts pollutant contact with the active catalytic surface, limiting broader application. With a band gap energy of 3.28 eV, TiO_2 is considered an effective semiconductor for photocatalytic processes. Its long-term chemical stability, resistance to light-induced degradation, and high photocatalytic activity further contribute to its utility. The efficiency of TiO_2 in degrading organic pollutants can be enhanced by incorporating adsorbent materials, which increase pollutant proximity to the active surface and accelerate degradation (Ulya et al., 2025).

An effective strategy to enhance the efficiency of TiO_2 involves employing a support material with a large surface area and high adsorption capacity, such as activated carbon. Activated carbon, a porous material with a strong affinity for organic compounds, can increase dye adsorption before the photodegradation process (Ruliza et al., 2018). Oil palm shells are an abundant and renewable biomass resource, making them a suitable raw material for activated carbon production, particularly given their high availability in tropical countries such

as Indonesia and Malaysia. Utilization of oil palm shells aligns with circular economy principles by converting agricultural waste into value-added products. The chemical composition of oil palm shell further supports its application as a precursor for activated carbon. Analytical data indicate that oil palm shell contains 47.38% carbon, 5.94% hydrogen, 0.47% nitrogen, 43.54% oxygen, and a minimal sulfur content of 0.05%. Its high fixed carbon and low ash content make oil palm shell a promising material for producing activated carbon with high surface area and porosity. These properties facilitate more effective interactions between pollutants and the photocatalyst. Consequently, the use of biomass-based activated carbon not only promotes sustainability but also improves the performance of photocatalytic systems (Yankovych et al., 2024).

The integration of TiO_2 with activated carbon (AC) derived from oil palm shells results in a composite system that mitigates the limitations of each component. Activated carbon functions as a support, preventing TiO_2 particle agglomeration, improving particle dispersion, and increasing the overall surface area. Furthermore, activated carbon serves as an initial adsorbent by capturing dye molecules on its surface, which increases the local concentration of pollutants near the active sites of TiO_2. According to Yankovych et al.(2024), TiO_2 activated carbon photocatalysts achieved a dye degradation efficiency of 72%, with 42% attributed to adsorption and 30% to photocatalysis for Acid Red 88 (AR88) at an initial concentration of 200 mg-L. Additionally, TiO_2-AC demonstrated effective photocatalytic performance for Basic Red 13 (BR13), with 47% adsorption and 11% photocatalysis, and for Basic Red 5 (BR5), with 25% adsorption and 16% photocatalysis. These results indicate accelerated and more efficient photodegradation, as reactions occur at sites with a higher concentration of adsorbed pollutants. Activated carbon also reduces the recombination rate of electron-hole pairs by providing additional electron transfer sites, which enhances the generation of reactive radicals. This synergy has been shown to improve photocatalytic activity significantly. Safni et al. (2024) reported that the addition of a TiO_2-activated carbon catalyst increased the degradation of Remazol Yellow FG from 8.34% without a catalyst to 95.02% during photolysis, and from 6.86% to 52.62% during sonolysis. The reduction of the band gap from 3.2 eV to 3.10 eV after combining with activated carbon further contributed to improved photocatalytic efficiency. Therefore, the development of TiO_2-activated carbon composites presents significant potential for treating industrial wastewater containing complex dye pollutants.

Variations in photocatalyst mass and dye concentration have been shown to influence degradation efficiency. Poluakan et al. (2015) reported that a TiO_2-activated carbon photocatalyst achieved a maximum degradation of 95% at a dye concentration of 30 ppm and a photocatalyst mass of 0.05 g, whereas TiO_2-zeolite reached only 83% at a concentration of 20 ppm with the same mass. In contrast, Safni et al. (2021) investigated photocatalyst masses ranging from 0.05 to 0.20 g and dye concentrations from 10 to 40 ppm, finding that the optimal mass was 0.15 g with a degradation efficiency of 91.63%, and the optimal dye concentration

was 20 ppm with a degradation efficiency of 87.45%. These findings suggest that the optimal mass and concentration are dependent on the specific composite and experimental conditions.

This study evaluates the effectiveness of a TiO_2-activated carbon composite for the photodegradation of Remazol Brilliant Blue R (RBBR). The synthesized composite is expected to operate efficiently under UV light via a combined adsorption and photocatalytic mechanism. Material characterization was performed using X-ray Diffraction (XRD) to identify crystal structure, X-ray Fluorescence (XRF) and Energy-Dispersive X-Ray Spectroscopy (EDX) to determine elemental composition, Attenuated Total Reflectance–Fourier Transform Infrared (ATR-FTIR) to analyze carbon functional groups, and UV–Vis Diffuse Reflectance Spectroscopy (UV-Vis DRS) to assess optical properties and band gap energy. The performance of the composite was evaluated by varying both the mass of the TiO_2-AC and the initial RBBR concentration to assess their impact on degradation efficiency.

1.2 Research Questions

1. What are the characteristics of the TiO_2-AC photocatalyst derived from oil palm shells as determined by XRD, XRF, EDX, FTIR, and UV–Vis DRS characterization?
2. What is the optimum mass of the TiO_2-AC photocatalyst for RBBR degradation?
3. What is the optimum concentration of RBBR in the degradation process using the TiO_2-activated carbon catalyst?

1.3 Research Objectives

1. To synthesize and characterize a TiO_2-AC photocatalyst derived from oil palm shells.
2. To determine the optimum photocatalyst mass for RBBR degradation.
3. To determine the optimum concentration of RBBR for degradation.

1.4 Scope and Limitations

1. The dye used in this study is Remazol Brilliant Blue R.
2. The synthesis method employed is impregnation.
3. The source of activated carbon is oil palm shell.
4. The independent variables are photocatalyst mass and dye concentration.
5. Characterization techniques include XRD, XRF, EDX, FTIR, UV–Vis DRS characterization, and UV-Vis spectrophotometry.
6. The degradation experiments are conducted under UV irradiation.

1.5 Significance of the Study

This research aims to offer an alternative solution for textile wastewater treatment by employing an environmentally friendly technology that integrates adsorption and photocatalysis. Utilizing biomass waste, specifically oil palm shells, reduces waste generation

and adds value by converting it into activated carbon for use as a photocatalyst support. Additionally, the study advances the development of locally sourced photocatalytic materials derived from abundant natural resources, thereby supporting technological self-reliance and reducing reliance on imported materials. This strategy aligns with sustainability objectives and promotes the adoption of circular economy principles in environmental management.

CHAPTER II
LITERATURE REVIEW

2.1 Islamic Perspective on Waste Management

Waste refers to the byproducts of industrial and household activities that are typically no longer reusable. It can be categorized into several types, including organic waste, which is naturally decomposable, and inorganic waste, which is resistant to or unable to be degraded by microorganisms. Textile manufacturing primarily generates inorganic waste, often in the form of liquid effluent from dyeing processes. The direct discharge of industrial wastewater into the environment, particularly into water bodies, can result in environmental degradation and pose significant threats to the sustainability of aquatic ecosystems. The accumulation of substantial waste poses a considerable challenge, as it negatively affects both humans and other organisms that depend on contaminated water sources for their daily needs.

Islam is regarded as a comprehensive religion that regulates not only the relationship between humans and God but also interactions among individuals and with the environment. Waste management and prudent resource utilization are considered integral to human responsibility as stewards (Khalifah) of the Earth. The Qur'an offers guidance and warnings to prevent excessive behavior and environmental destruction (Matsna Afwi Nadia & M. Riyan Hidayat, 2023). This principle is emphasized in the Qur'an, specifically in Surah al A'raf (7:56):

وَلَا تُفْسِدُوْا فِى الْاَرْضِ بَعْدَ اِصْلَاحِهَا وَادْعُوْهُ خَوْفًا وَّطَمَعًاۗ اِنَّ رَحْمَتَ اللّٰهِ قَرِيْبٌ مِّنَ الْمُحْسِنِيْنَ ﴿٥٦﴾

Translation: "And cause not corruption upon the earth after its reformation. And invoke Him in fear and aspiration. Indeed, the mercy of Allāh is near to the doers of good." (QS. al A'raf:56)

Surah al A'raf, verse 56, prohibits causing فساد (corruption or destruction) on Earth after Allah has made it good. Hamka explains that such destruction may manifest as ظلم (injustice), arrogance, or actions that disrupt the natural order. He emphasizes that if humans cannot improve conditions, they should at least avoid damaging what is already good (Hamka, 2015). This principle is particularly relevant to environmental pollution resulting from industrial waste, including textile effluents that contain hazardous substances and pose risks to the environment, water bodies, and human health.

A hadith narrated by Imam Abu Dawud further reinforces the prohibition against actions that result in environmental harm:

سنن أبي داوود ٢٤ :حَدَّثَنَا إِسْحَاقُ بْنُ سُوَيْدٍ الرَّمْلِيُّ وَ عُمَرُ بْنُ الْخَطَّابِ أَبُوْ حَفْصٍ وَ حَدِيْثُهُ أَتَمُّ أَنَّ سَعِيْدَ بْنَ الْحَكَمِ

:حَدَّثَهُمْ قَالَ :أَخْبَرَنَا نَافِعُ بْنُ يَزِيْدَ حَدَّثَنِيْ حَيْوَةُ بْنُ شُرَيْحٍ أَنَّ أَبَا سَعِيْدٍ الْحِمْيَرِيَّ حَدَّثَهُ عَنْ مُعَاذِ بْنِ جَبَلٍ قَالَ

.قَالَ رَسُوْلُ اللهِ صَلَّى اللهُ عَلَيْهِ وَ سَلَّمَ اتَّقُوا الْمَلَاعِنَ الثَّلَاثَةَ الْبَرَازَ فِي الْمَوَارِدِ وَ قَارِعَةِ الطَّرِيْقِ وَ الظِّلِّ

Translation:
Sunan Abu Dawud 24: It was narrated to us by Ishaq bin Suwaid Ar-Ramli and ‘Umar bin Al-Khattab Abu Hafsh, whose narration is more complete, that Sa‘id bin Al-Hakam narrated to them, who said: Nafi‘ bin Yazid informed us, Haiwah bin Shuraih narrated to us, that Abu Sa‘id Al-Himyari narrated to him from Mu‘adh bin Jabal, who said: The Messenger of Allah (peace be upon him) said: “Beware of the three acts that bring curses: relieving oneself at water sources, in the middle of the road, and in places of shade.” (HR. Abu Dawud: 24)

The hadith of the Prophet Muhammad (peace be upon him) referenced above explicitly prohibits relieving oneself in three locations: water sources, public roads, and places of shade. Scholars interpret this prohibition as a strict directive aimed at safeguarding public welfare. Imam An-Nawawi explains that the term *al-malā‘in* refers to actions that incur both the curse of Allah and public disapproval, as they cause widespread harm (An-Nawawi, 2014). The term al-mawārid encompasses all sources of water, including rivers, springs, wells, and lakes, thereby rendering the prohibition comprehensive. Imam Asy-Shaukani asserts that the prohibition applies irrespective of the quantity of water, as the principle of caution in maintaining water purity is paramount (Asy-Syaukani, 2006). Consequently, this hadith addresses not only personal hygiene but also the broader prohibition of environmental degradation, particularly the pollution of water sources.

Contemporary scholars emphasize that the prohibition against contaminating water sources remains highly relevant to current environmental challenges. Yusuf Al-Qaradawi asserts that Islam places significant importance on maintaining the cleanliness of water, as it is a communal resource that must remain unpolluted. This perspective is directly applicable to modern contexts, such as the textile industry, which frequently generates colored and toxic liquid waste. Discharging untreated waste into rivers constitutes a violation of others’ rights to clean water. From an Islamic standpoint, such actions are classified as ḍirār (harm), which is explicitly forbidden. Accordingly, this hadith obligates all industrial sectors, including textiles, to adopt environmentally responsible waste management practices as a matter of both moral and religious duty (Al-Qaraddawi, 2001).

2.2 Remazol Brilliant Blue R

Dyes are chemical compounds that impart colour to various materials and are widely used in the textile industry. As textile production and demand have increased, the use of synthetic dyes has also risen substantially. Reactive dyes are widely used for their ability to form covalent bonds with textile fibers, producing colors that are highly resistant to washing and light exposure. Remazol Brilliant Blue R (RBBR), a member of the anthraquinone dye group, exemplifies such reactive dyes and is recognized for its high color intensity (Siswanti et al., 2023).

Remazol Brilliant Blue R (RBBR) possesses a complex chemical structure that includes sulfonate groups ($–SO_3Na$), which confer water solubility. The presence of chromophore groups is responsible for its coloration, while auxochrome groups enhance its bonding with

textile substrates. This molecular composition renders RBBR highly stable in the environment and resistant to natural microbial degradation. RBBR has the chemical formula $C_{22}H_{16}N_2Na_2O_{11}S_3$ and a molecular weight of approximately 626.54 g-mol. The complete chemical structure is presented in Figure 2.1.

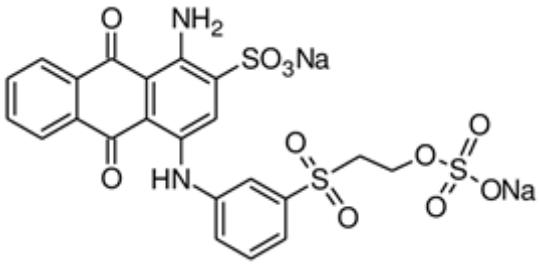

Figure 2.1 Chemical Structure of Remazol Brilliant Blue R (Hidayati et al., 2024)

The presence of RBBR in textile industrial wastewater represents a significant environmental concern. The intense blue coloration of this compound diminishes the aesthetic quality of water bodies and disrupts aquatic ecosystems by limiting sunlight penetration. Consequently, phytoplankton photosynthesis is impaired, resulting in reduced dissolved oxygen levels. Furthermore, due to its non-biodegradable nature, RBBR can persist in the environment, and its long-term accumulation may disrupt ecosystem balance (Farhan et al., 2023).

Multiple studies have shown that prolonged exposure to reactive dye wastewater, including RBBR, can cause skin irritation, respiratory disorders, and mutagenic or carcinogenic effects. These adverse outcomes arise because RBBR can generate reactive, harmful intermediates during incomplete degradation. Consequently, it is essential to develop effective wastewater treatment methods that fully degrade this dye into simple, non-toxic compounds such as carbon dioxide and water (Hidayati et al., 2024).

Previous research has demonstrated that RBBR wastewater can be treated using various methods. Safni et al. (2020) reported that a TiO_2-activated carbon photocatalyst achieved optimal degradation at an initial RBBR concentration of 20 ppm with a photocatalyst mass of 0.1 g, resulting in up to 86% degradation within 120 minutes. Studies employing natural bio-adsorbents indicated that activated dried banana peels reduced RBBR concentration by up to 78% under optimal conditions of 25 ppm and an adsorbent dose of 1 g per 100 mL of solution (Safni et al., 2024). In addition to photocatalysis and adsorption, biological methods have also demonstrated considerable potential. Moyo et al. (2022) found that bacterial isolates such as *Pseudomonas* sp. and *Bacillus subtilis* degraded more than 70% of RBBR within 5 to 7 days, depending on environmental factors such as pH and nutrient availability.

2.3 Photodegradation of Dyes

Photodegradation is a method for treating organic waste that uses light energy to break down complex compounds into simpler, more environmentally benign substances (Khan et al., 2020). This approach shows significant potential for treating toxic, non-biodegradable textile dye wastewater. Typically, the photodegradation process employs a photocatalyst, such as titanium dioxide (TiO_2), which is activated by ultraviolet (UV) light to generate reactive free radicals, including •OH and $O_2^{\bullet -}$. These radicals facilitate the cleavage of chemical bonds in dye molecules, resulting in the formation of harmless compounds (Zaaboul et al., 2024).

The photodegradation mechanism generally consists of three primary stages: activation of the photocatalyst by light, formation of electron–hole pairs (e^--h^+), and subsequent degradation reactions with contaminants. When TiO_2 is exposed to UV light with energy equal to or exceeding its band gap, electrons are promoted from the valence band to the conduction band, creating holes in the valence band. These electrons and holes subsequently react with water or dissolved oxygen to produce highly reactive free radicals (Pingmuang et al., 2017).

Figure 2.2 presents a general schematic of the photodegradation process utilizing a TiO_2 photocatalyst:

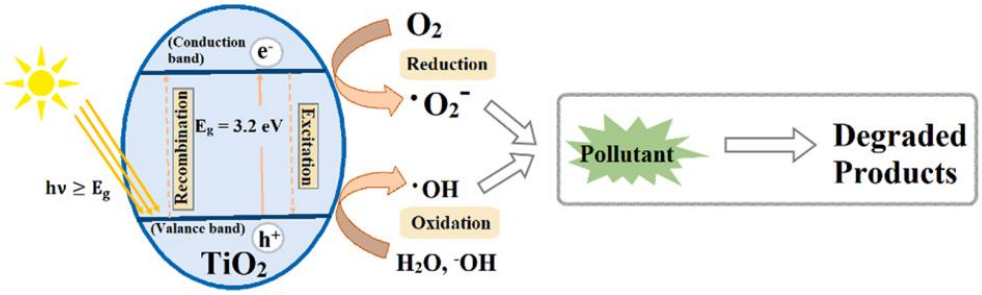

Figure 2.2 Photodegradation Mechanism by TiO_2 Photocatalyst (Nabi et al., 2021)

Ulya et al. (2022) utilized TiO_2 -natural zeolite as a photocatalyst for the degradation of Indigosol Blue dye, achieving an optimal degradation efficiency of 58.7% at a concentration of 600 ppm, a reaction time of 30 minutes, and a photocatalyst mass of 0.02 g (Ulya et al., 2022). Similarly, Michelle Poluakan et al. (2015) investigated TiO_2-activated carbon and TiO_2-zeolite combinations, demonstrating that TiO_2-activated carbon degraded Remazol Yellow dye by up to 95% at an initial concentration of 30 ppm.

These findings suggest that photocatalytic photodegradation technology offers an effective approach for mitigating water pollution from textile wastewater. Incorporating support materials such as zeolite or activated carbon is recommended to enhance photocatalyst efficiency by increasing surface area or reducing the electron–hole recombination rate. Accordingly, this study uses a TiO_2-activated carbon composite photocatalyst synthesized by the impregnation method, which is expected to significantly enhance the degradation of Remazol Brilliant Blue R.

2.4 TiO_2 as a Photocatalyst

Titanium dioxide (TiO_2) is among the most extensively utilized semiconductor materials in photocatalytic technology. Its advantages include high chemical and thermal stability, non-toxicity, low cost, and abundance in nature. Crystallographically, TiO_2 exists in three primary phases: anatase, rutile, and brookite. The anatase phase demonstrates the highest photocatalytic activity, attributed to its larger specific surface area and crystal structure that enhances electron mobility (Rizkiana et al., 2020).

The effectiveness of TiO_2 tioas a photocatalyst is primarily determined by its band gap, which is approximately 3.2 eV for the anatase phase. This band gap enables electron excitation under ultraviolet light irradiation. When TiO_2 absorbs photons with energy exceeding its band gap, electrons are promoted from the valence band to the conduction band, resulting in the formation of electron–hole pairs that initiate redox reactions with environmental pollutants (Anucha et al., 2022).

Figure 2.3 presents the energy band diagram and illustrates the mechanism of electron excitation in TiO_2 semiconductors.

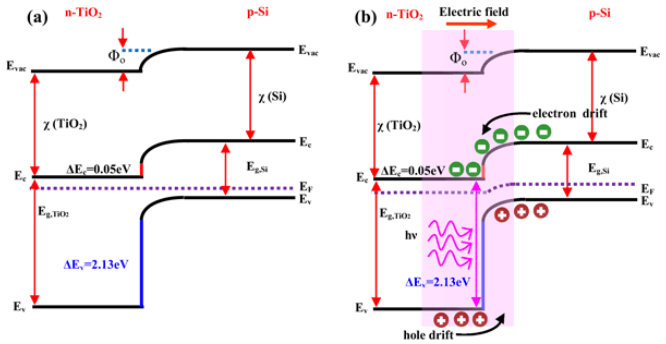

Figure 2.3 a) band alignment under dark conditions (equilibrium). b) band alignment under light irradiation (non-equilibrium), showing the mechanism of electron–hole excitation and charge separation. (Dewasi & Mitra, 2017).

In addition to its widespread application as a white pigment in paints and cosmetics, TiO_2 is widely recognized as a leading semiconductor for photocatalysis due to its unique properties. TiO_2 occurs in three primary crystalline phases: anatase, rutile, and brookite. Of these, anatase exhibits the highest photocatalytic activity, which is attributed to its open crystal structure and relatively large surface area. Approaches to improve TiO_2 photocatalytic performance include doping with metals and nonmetals, forming composites with carbon-based materials, and synthesizing nanoparticles to increase surface area. Zaleska (2008) demonstrated that reducing TiO_2 particle size to the nanometer scale significantly enhances reactivity by increasing the number of available active sites (Zaleska, 2008).

Tichapondwa et al. (2020) reported that anatase- and rutile-phase TiO_2 photocatalysts efficiently degraded methylene blue, achieving 81.4% degradation after 100 minutes of UV irradiation. X-ray diffraction (XRD) and UV–Vis diffuse reflectance

spectroscopy (DRS) analyses indicated that both the crystal phase and band gap energy play significant roles in determining degradation efficiency. Additionally, Ulya et al. (2025) observed that TiO_2 modified with natural zeolite reduced the band gap from 3.31 eV to 3.29 eV, enhanced light absorption at longer wavelengths, and increased degradation efficiency to 99.74% for a 10 ppm methyl violet solution (Ulya et al., 2025)

Mattle and Thampi (2013) reported that synthesized TiO_2 outperformed TiO_2–zeolite composites, achieving up to 90% degradation of Remazol Brilliant Blue R within 40 minutes of irradiation. TiO_2 is widely used as a primary component in composite photocatalysts because of its ability to generate highly reactive free radicals and its proven effectiveness in textile wastewater treatment (Mattle & Thampi, 2013). The incorporation of activated carbon with TiO_2 is expected to further increase surface area and enhance interactions with dye molecules.

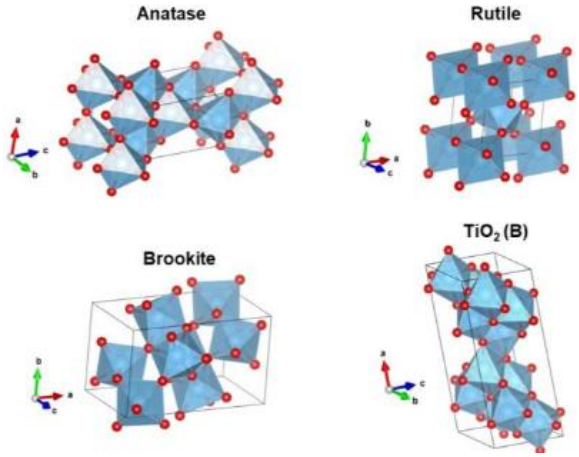

Figure 2.4 Comparison of TiO_2 Crystal Structures of Anatase, Rutile, and Brookite TiO_2 Phases (Eddy et al., 2023)

Table 2.1 Comparison of Crystal Structure and Band Gap of TiO_2 Phases (Eddy et al., 2023)

Phase	Crystal System, Space Group	Lattice Parameters	Density (g-cm³)	Band Gap Energy (eV)
Brookite	Ortombik, *Pbca*	a = 9.148 Å b = 5.447 Å c = 5.145 Å V = 257.38 Å³	4.12	3.14 – 3.31
Rutile	Tetragonal, $P4_2$-*mnm*	a = b = 4,594 Å c = 2.959 Å V = 62.45 Å³	4.25	3.02 – 3.04
Anatase	Tetragonal, $I4_1$-*amd*	a = b = 3,784 Å c = 9.515 Å V = 136.24 Å³	3.89	3.20 – 3.23

Based on the table above, the crystal structure of TiO_2 comprises several primary phases, each exhibiting distinct physical and optical properties: anatase, rutile, brookite, and TiO_2 (B). These phase differences have a significant impact on photocatalytic performance. Anatase, characterized by a tetragonal crystal system, possesses a density of 3.89 g-cm³ and a band gap energy of approximately 3.20–3.23 eV. This phase is most frequently employed as a photocatalyst due to its high specific surface area, low electron–hole recombination rate, and stable phase behavior at low to moderate temperatures. The indirect band gap of anatase

extends the lifetime of electron–hole pairs, thereby enhancing the efficiency of photocatalytic reactions (Eddy et al., 2023).

Rutile also exhibits a tetragonal crystal system, with a higher density of 4.25 g-cm^3 and a narrower band gap of 3.02–3.04 eV. Although the band gap of rutile is closer to the visible light region, its smaller surface area and higher charge recombination rate generally result in lower photocatalytic activity compared to anatase. However, rutile demonstrates greater thermal stability and is commonly utilized in high-temperature applications or as a component in multiphase systems. Brookite, which possesses an orthorhombic crystal system and a band gap of 3.14–3.31 eV, is challenging to synthesize in pure form and remains stable primarily at larger crystal sizes. The presence of structural defects, such as excess Ti^{4+} ions, can enhance the photocatalytic activity of brookite. TiO_2 (B), another phase, features a monoclinic crystal structure and a band gap of approximately 3.09–3.22 eV. Initially recognized for its application in batteries due to its open lattice structure, recent studies have demonstrated its potential in photocatalysis when combined with doping or specific oriented synthesis techniques (Eddy et al., 2023). Among these phases, anatase remains the most effective for photocatalytic applications, as its optical and structural properties facilitate efficient charge separation and high surface reactivity.

2.5 Activated Carbon from Palm Shells

Activated carbon, a porous carbon material, is widely utilized in environmental applications, particularly as an adsorbent in wastewater treatment. Its high specific surface area, large pore volume, and superior adsorption capacity make it a suitable support material for photocatalyst composites. Oil palm shells represent a promising raw material for activated carbon production, given their abundant availability in Indonesia as a solid waste byproduct of the palm oil industry (Hartanto & Ratnawati, 2010).

The chemical composition of oil palm shell supports its use as a raw material for activated carbon. Ultimate analysis indicates a carbon content of 47.38%, hydrogen 5.94%, nitrogen 0.47%, oxygen 43.54%, and a very low sulfur content of 0.05%. Proximate analysis reveals a moisture content of 9.01%, a volatile matter of 68.00%, a fixed carbon of 20.37%, and an ash content of 2.62%. The high fixed carbon and low ash contents suggest that oil palm shell can yield activated carbon with a favorable surface area and porosity. These properties are significant because activated carbon is frequently used as a support material for TiO_2 in photocatalytic applications (Yuliusman et al., 2017; Hendriansyah et al., 2018).

Due to its high carbon content and hard structure, oil palm shells can produce activated carbon with a stable and durable pore structure. The production process typically involves two main stages: carbonization and activation. Carbonization converts organic material into char through incomplete combustion at elevated temperatures. Activation, which enlarges pore volume and increases active surface area, can be performed physically using steam or CO_2

gas, or chemically with activating agents such as KOH, HCl, $ZnCl_2$, or H_3PO_4 (Hartanto & Ratnawati, 2010).

Utilizing activated carbon as a support in TiO_2 photocatalysts offers several advantages. Activated carbon enhances the adsorption of pollutant molecules onto the catalyst surface, thereby accelerating degradation. It also inhibits the recombination of electron–hole pairs in TiO_2, which increases photocatalytic efficiency. Additionally, activated carbon broadens the light absorption spectrum and improves the dispersion of TiO_2 particles within the composite. The TiO_2–activated carbon combination achieves a degradation efficiency of Remazol Yellow dye up to 95% within 60 minutes, compared to only 76% for the TiO_2–zeolite combination under similar conditions. This improvement is attributed to the higher adsorption capacity and larger surface area of activated carbon. Furthermore, studies report that activated carbon derived from oil palm shell can attain a surface area exceeding 1000 m²-g after chemical activation with $ZnCl_2$, making it highly effective as a photocatalyst support in wastewater treatment (Yuliusman et al., 2017).

This study employs activated carbon derived from oil palm shell as a supporting material for TiO_2, due to its environmental sustainability, high availability, and demonstrated effectiveness in enhancing photocatalytic efficiency. The resulting composite is anticipated to provide optimal degradation of Remazol Brilliant Blue R.

Surface morphology characterization of activated carbon derived from oil palm shell using Scanning Electron Microscopy (SEM) reveals substantial changes following chemical activation. Before activation, SEM images indicate that the char surface remains covered by impurities and carbonization residues, resulting in suboptimal pore development. Consequently, the effective surface area available for adsorption is relatively low (Hartanto & Ratnawati, 2010).

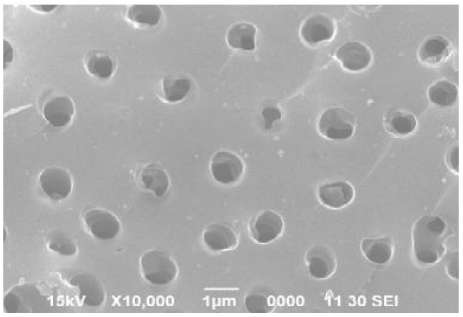

Figure 2. 5 SEM results of palm shell activated carbon with NaOH activator, activation time 4 hours (Hartanto & Ratnawati, 2010).

Following chemical activation with NaOH for 4 hours, the morphology of the activated carbon demonstrates significantly improved pore opening. The carbon surface is cleaner, and the pores are widely open and uniformly distributed. This enhancement in pore openness is crucial for increasing the specific surface area and adsorption capacity of the material. These findings align with the iodine adsorption data, which indicate values up to 851.88 mg-g, thereby meeting the quality standards for activated carbon as specified in SNI No. 06-3730-1995

(Hartanto & Ratnawati, 2010). Consequently, chemical activation not only optimizes the pore structure but also directly enhances the performance of activated carbon as an adsorbent in photocatalytic and wastewater treatment applications.

2.6 Synthesis of TiO_2-Activated Carbon by Impregnation Method

The synthesis of TiO_2-activated carbon via the impregnation method is designed to integrate the adsorption capacity of activated carbon with the photocatalytic properties of TiO_2 within a single composite material. In this process, TiO_2 particles are uniformly distributed on the surface of activated carbon to maximize interfacial contact and improve pollutant degradation efficiency.

Impregnation methods can be categorized as dry or wet. In dry impregnation, the solution volume matches or slightly exceeds the pore volume, allowing capillary action to distribute the solution evenly within the pores. Conversely, wet impregnation uses a significantly larger solution volume, which leads to slower diffusion driven mass transport and less uniform adsorption (Coronel et al., 2021).

The impregnation method has demonstrated superiority in synthesizing TiO_2-activated carbon composites by uniformly distributing TiO_2 particles across the carbon surface, maintaining effective interfacial contact, and enhancing charge-transfer efficiency during photocatalysis (Martínez et al., 2020). This approach typically yields uniform particle distributions with crystallite sizes of 20-30 nm. However, excessive TiO_2 loading, specifically above 20 wt% of the total composite weight, may result in pore blockage (Ghamarpoor et al., 2024). The impregnation method remains widely employed for metal and oxide-based catalysts, as it achieves precursor distribution efficiencies of 80-90% on the support surface. Additionally, this method offers flexibility in adjusting the TiO_2 precursor ratio without necessitating specific operational conditions (Munnik et al., 2015).

2.6.1 Crystal Structure Analysis using X-Ray Diffraction (XRD)

X-Ray Diffraction (XRD) is an important technique for identifying the crystal structure of solid materials. It works by X-rays diffracting off crystal planes in a sample. When X-rays hit a crystal lattice, some radiation is reflected by the atomic planes, forming a diffraction pattern unique to each crystal structure. This pattern reveals information about the crystal type, purity, and crystallite size (Adams, 2005).

In this study, XRD was used to confirm that the crystal phase of TiO_2 in the TiO_2-activated carbon composite remained in the anatase phase after synthesis using the impregnation method. Identifying the crystal phase is important because the anatase phase has higher photocatalytic activity than the rutile or brookite phases. The characteristic diffraction peak for the anatase phase is at $2\theta = 25.3°$, while the rutile phase appears at $2\theta = 27.4°$ (Aguilar et al., 2023). The presence of these peaks serves as the main indicator in XRD analysis.

The XRD technique also allows the calculation of crystallite size using the Scherrer Equation:

$D = K\lambda - (\beta \cos \theta)$ 2.1

Where:

D = crystallite size (nm)

K = shape constant (usually 0.9)

λ = X-ray wavelength (Cu Kα = 1.5406 Å)

β = peak width at half maximum (FWHM) in radians

θ = diffraction angle (degrees)

This equation allows estimation of the crystallite size of TiO_2 dispersed in activated carbon. A smaller crystallite size generally provides a larger specific surface area, which can enhance photocatalytic performance by increasing the number of active sites available for adsorption and photocatalytic reactions. In addition, smaller crystallites shorten the migration distance of photogenerated charge carriers, thereby reducing the probability of electron–hole recombination and improving photocatalytic efficiency. XRD analysis is also useful for identifying the crystalline phases present in the material, such as anatase, rutile, or brookite, as well as evaluating the crystallinity and structural changes that may occur after composite formation. The XRD instrument commonly used is a Bragg–Brentano type powder diffractometer equipped with a scintillation counter detector. Prior to analysis, the sample is usually dried and finely ground to ensure homogeneity, then mounted on a sample holder and scanned over a 2θ range of 5°–80°. The resulting diffraction pattern is presented as a plot of intensity versus diffraction angle (2θ), where each crystalline phase produces characteristic diffraction peaks. These peaks are subsequently analyzed and compared with reference databases such as the Joint Committee on Powder Diffraction Standards (JCPDS) to determine the crystal structure, phase composition, and degree of crystallinity of the material (Ulya et al., 2025)

Research by Simamora & Sukmawati (2020), which used XRD to characterize TiO_2-carbon composites, showed that the impregnation process did not alter the anatase phase but caused only a slight decrease in crystallinity, which did not significantly affect photocatalytic activity (Siswanti et al., 2023). A similar result was also reported by Marwan et al. (2022), who found that TiO_2 combined with activated carbon retained the main anatase peak at 25.3°, indicating the stability of its crystal structure after modification (Eddy et al., 2023).

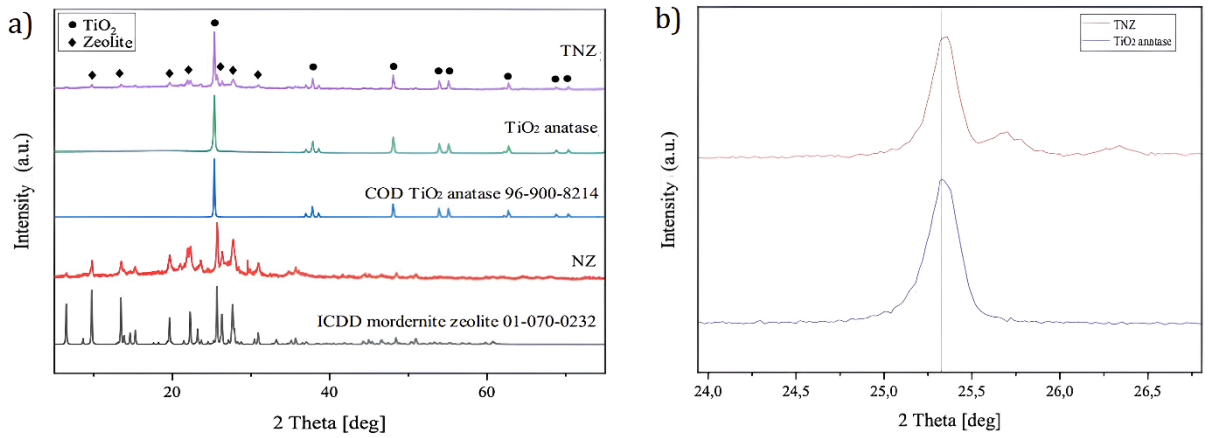

Figure 2.6 (a) XRD plot of TNZ and its comparison with commercial anatase TiO_2 and natural zeolite as well as standard TiO_2 samples (96-900-8214-CO) and standard mordenite zeolite (01-070-0232-ICDD); (b) Enlargement of XRD plot of anatase TNZ and TiO_2 (Ulya et al., 2022)

In this study, XRD was used not only to identify the crystal phase of TiO_2 but also to determine whether the impregnation process affects crystallinity or induces any phase transition. This information is important to ensure the resulting composite material maintains good crystal quality and is suitable for photodegradation applications.

2.6.2 Analysis of TiO_2-Activated Carbon Composition Using XRF (X-ray Fluorescence) and EDX (Energy-Dispersive X-Ray Spectroscopy)

X-Ray Fluorescence (XRF) is a non-destructive analytical technique employed to determine the qualitative and quantitative elemental composition of materials. In this method, X-rays interact with atoms in the sample, producing characteristic X-rays specific to each element. The intensity of the emitted fluorescence is directly proportional to the concentration of the corresponding element in the material (Adams, 2005).

In this study, XRF was utilized to confirm the presence of titanium (Ti) in the TiO_2-activated carbon composite and to identify additional elements, including carbon (C) from the activated carbon and potential metallic impurities. This analysis is essential for evaluating the effectiveness of TiO_2 impregnation onto activated carbon and for assessing the purity of the resulting composite material.

XRF instruments can also provide information on the homogeneity of elemental distribution across the photocatalyst surface, although their spatial resolution is lower than that of scanning electron microscopy with energy-dispersive X-ray spectroscopy (SEM-EDX). XRF results present the weight or atomic percentages of elements detected in the sample. Previous studies, including Handayani et al. (2020), have demonstrated that the addition of TiO_2 to activated carbon is clearly detectable by XRF and is associated with enhanced photocatalytic activity.

Table 2. 2 XRF Analysis Shows Oxide Concentration in Charcoal (Adekunle et al., 2020)

Major Oxides	Concentration (Wt%)		
	Activated Carbon	Sawdust Charcoal	Rice Husk Charcoal
SiO_2	80.80	80.04	80.20
Al_2O_3	3.03	2.11	2.00
Fe_2O_3	0.05	0.72	0.15
TiO_2	0.07	-	0.20
CaO	0.10	0.18	2.75
P_2O_5	0.02	0.65	0.02
K_2O	0.11	2.16	3.45
MnO	0.01	0.06	0.41
MgO	0.01	3.12	0.01
Na_2O	0.02	0.44	0.14
LOI	-	10.52	10.60
Ash	15.60	-	-

In addition to using X-Ray Fluorescence (XRF), the elemental composition analysis of materials can also be carried out using Energy-Dispersive X-ray (EDX). This instrument is generally integrated with a Scanning Electron Microscope (SEM). It is used to identify the elements present on the surface of a sample. The working principle of EDX is based on the interaction between an electron beam and atoms within the sample, which produces characteristic X-rays for each element. The emitted X-ray energy is then detected and displayed in the form of an energy spectrum, allowing the constituent elements of the material to be identified and their composition percentages to be determined in terms of weight percent (wt%) or atomic percent (at%) (Skoog et al., 2016).

Table 2. 3 Elemental percentages in Activated Carbon-TiO_2 based on EDX analysis

Element	Weight (%)	Atom (%)
O	51.27	56.53
C	23.36	34.30
Ti	23.09	8.50
Zr	1.17	0.23
Cu	0.64	0.18
K	0.25	0.11

Through the EDX spectrum, the elements contained in the material can be identified from the energy peaks that appear on the graph. For example, research conducted by Sugandi et al. (2024) showed that the results of elemental composition analysis using EDX on TiO_2–coconut carbon composites indicated the presence of several main elements, namely oxygen (O), carbon (C), and titanium (Ti). Based on the analysis results, the oxygen element has a weight percentage of 51.27% with an atomic percentage of 56.53%, while carbon is 23.36% (34.30 at%) and titanium is 23.09% (8.50 at%). In addition to these main elements, other elements were also detected in small amounts, such as zirconium (1.17 wt%), copper (0.64 wt%), and potassium (0.25 wt%). The presence of Ti and O elements indicates the formation of a TiO_2 phase in the composite material, while the C element comes from coconut fiber used

as a carbon matrix. In addition, Ruliza et al. (2018) showed that the TiO_2-activated carbon composite contains several main elements, such as carbon (C), oxygen (O), and titanium (Ti), which are visible from the peaks in the EDX spectrum. The carbon element comes from activated carbon, while titanium and oxygen come from TiO_2 deposited on the surface of activated carbon. These results indicate that EDX analysis can be used to identify the elemental composition in TiO_2-AC composite materials (Ruliza et al., 2018).

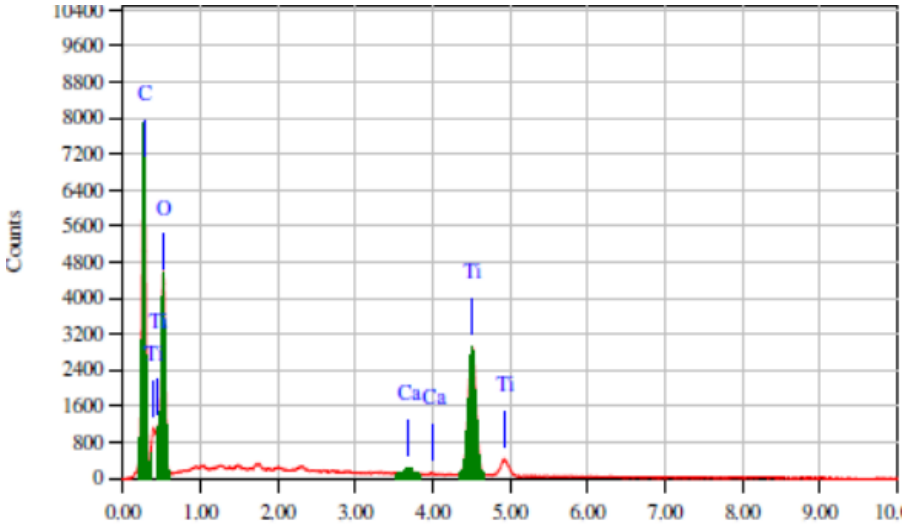

Figure 2. 7 EDX Spectrum of TiO_2-Activated Carbon Composite (Ruliza et al., 2018)

2.6.3 UV-Vis DRS

UV-Visible Diffuse Reflectance Spectroscopy (UV-DRS) is used to analyze a material's optical properties, particularly light absorption and band gap energy. In this study, UV-DRS assessed the TiO_2-activated carbon photocatalyst's light absorption at specific wavelengths and its band gap value (Morozzi et al., 2021).

UV-DRS measures diffusely reflected light from a solid sample. The resulting reflectance spectrum is converted to an absorption coefficient using the Kubelka–Munk transformation. A Tauc Plot is then used to determine the band gap by extrapolating the linear portion of the $(F(R)hv)^n$ versus photon energy (hv) graph, where *n* depends on the electronic transition type (*n* = 1-2 for direct transitions) (Siswanti dkk., 2023).

The band gap is a key parameter in photocatalysis, as it defines the minimum energy of light needed to activate the photocatalyst. A smaller band gap allows the material to absorb a broader light spectrum, including visible light. Consequently, reducing the TiO_2 band gap is a common strategy in photocatalyst development (Ulya et al., 2022).

Combining TiO_2 with activated carbon can reduce the band gap by creating oxygen vacancies in the TiO_2 crystal structure. Heating TiO_2 with carbon removes oxygen from the lattice, forming vacancies that introduce localized electrons and new energy levels within the

band gap. These levels lower the energy needed for electron excitation, narrowing the band gap and enhancing visible light response (Guan et al., 2023).

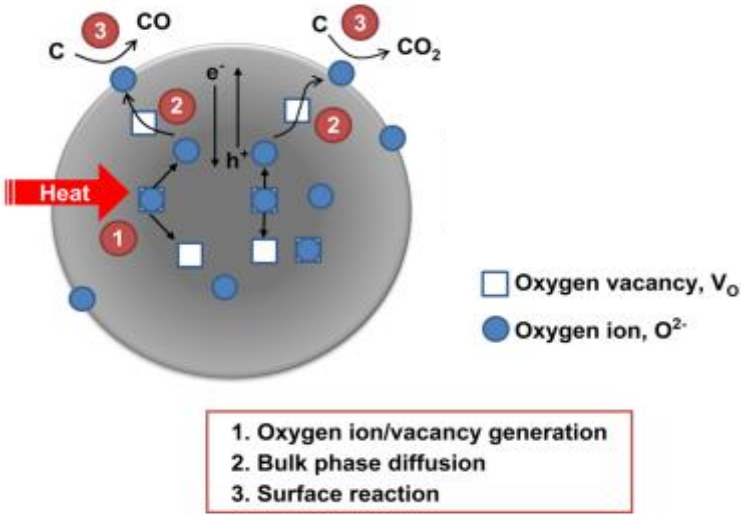

Figure 2. 8 Mechanism of oxygen depletion due to heating (Zheng et al., 2022)

The illustration above depicts the formation of oxygen vacancies resulting from high-temperature heating of metal oxides. Elevated temperatures weaken the bond between oxygen and the semiconductor metal, causing oxygen molecules to be released from the metal oxide crystal. In the presence of carbon molecules, the liberated oxygen bonds with carbon to form CO or CO_2 compounds (Zheng, Jiang, Gao, & Tong, 2022). Furthermore, oxygen vacancies induced by heating can cause structural modifications in TiO_2, resulting in the formation of Ti–O–C. In this process, carbon atoms enter the TiO_2 crystal and occupy the positions of missing oxygen atoms in the TiO_2 lattice, which are released by heating (Kumar et al., 2022).

Handayani et al. (2020) demonstrated that combining TiO_2 with activated carbon derived from oil palm shells reduced the band gap from 3.2 eV to approximately 2.8 eV, resulting in enhanced photocatalytic activity under visible light. Consistent findings were reported by Ren et al. (2007), who observed that doping TiO_2 with carbon materials increased light absorption and extended the spectral response to wavelengths greater than 45 nm.

In this study, UV–Vis diffuse reflectance spectroscopy (DRS) was used to confirm that the TiO_2-activated carbon composite derived from oil palm shells had an appropriate band gap and could absorb both UV and a portion of visible light. The band gap values obtained from UV–Vis DRS analysis serve as a basis for evaluating the photocatalyst's effectiveness in dye degradation.

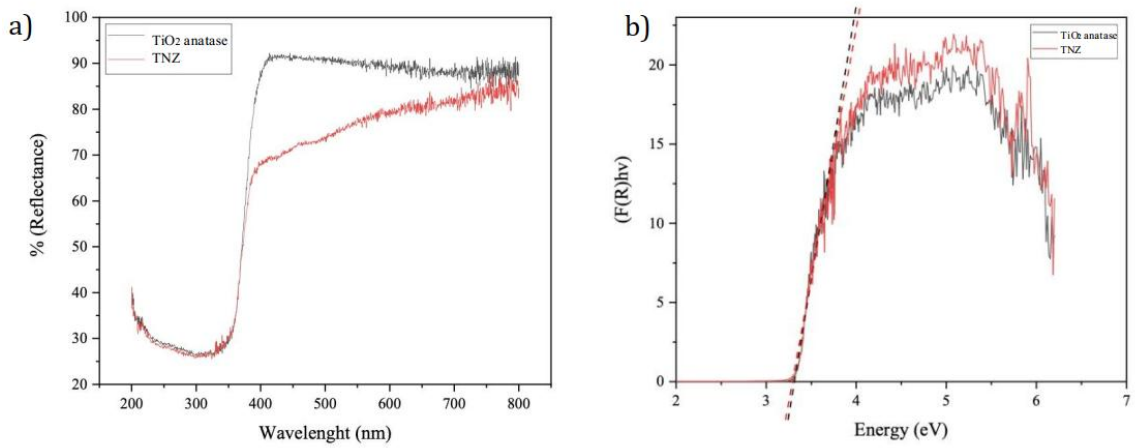

Figure 2. 9 UV-DRS Curves and Tauc Plots of TiO_2-Activated Carbon Photocatalysts (a) Plot of reflectance vs. wavelength; (b) Tauc plots of TNZ and anatase TiO_2 plotted using the Kubelka Munk function (Ulya et al., 2022).

2.6.4 Analysis of TiO_2-Activated Carbon Functional Groups Using Attenuated Total Reflectance–Fourier Transform Infrared (ATR-FTIR)

Attenuated Total Reflectance–Fourier Transform Infrared (ATR-FTIR) is a widely used FTIR testing technique due to its speed and efficiency, making it widely used as the initial stage of material analysis. The advantage of ATR-FTIR lies in its simple sample preparation, eliminating complex processes such as KBr mixing or grinding. Furthermore, this technique can produce a wider spectrum range and minimize the influence of differences in sample size (Thompson et al., 2009).

The working principle of ATR-FTIR is based on the total internal reflection of IR light reflected by ATR crystals, which then interacts with molecules on the sample surface. This interaction then causes changes in the sample's intensity, which are monitored and then analyzed. The crystals used in ATR-FTIR are typically zinc selenide (ZnSe) or diamond, which have optical properties suitable for this internal reflection process (Beasley et al., 2014).

FTIR spectra are interpreted by identifying absorption peaks at specific wavenumbers that correspond to vibrations of specific functional groups. Generally, the 4000–400 cm^{-1} wavenumber region is divided into several important regions: the O–H stretching region at around 3200–3600 cm^{-1}, the C–H stretching region at 2800–3000 cm^{-1}, and the fingerprint region below 1500 cm^{-1}, which is unique to each compound. Furthermore, metal–oxygen bond vibrations, such as Ti–O, generally appear at lower wavenumbers, around 400–700 cm^{-1}. Identification of these peaks provides the basis for determining the chemical composition and interactions between components in the analyzed material (Habibullah et al., 2025).

The FTIR spectrum of TiO_2 generally shows a strong absorption band at wavenumbers around 400–700 cm^{-1}, which corresponds to Ti–O–Ti bond vibrations. Meanwhile, activated charcoal exhibits several characteristic functional groups, such as the hydroxyl group (O–H) at around 3400 cm^{-1}, the carbonyl group (C=O) at around 1700 cm^{-1}, and the C–O group in

the range of 1000–1300 cm^{-1}. The presence of these groups indicates that activated charcoal has a surface rich in active sites that can play a role in the adsorption process. The differences in spectral characteristics between inorganic TiO_2 and organic carbon-based activated charcoal provide the basis for understanding the interactions that occur in composite materials (Beasley et al., 2014).

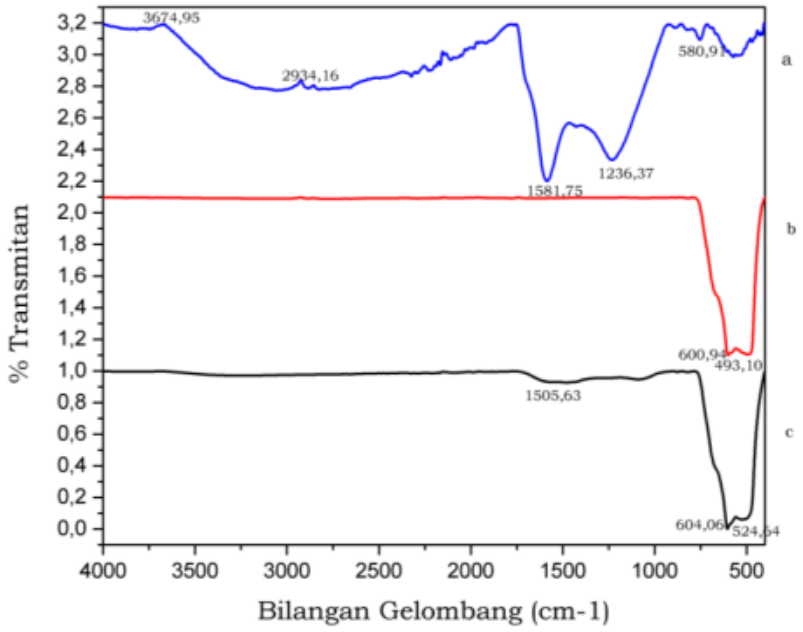

Figure 2.10 The FTIR spectrum of TiO_2 and activated carbon (Mustafidah & Ikhsan, 2022)

The FTIR spectrum of activated carbon generally indicates the presence of various oxygen- and carbon-containing functional groups that play important roles in adsorption processes and surface interactions. Based on previous research, activated carbon derived from coffee grounds exhibited an absorption peak at 3674.95 cm^{-1} corresponding to O–H stretching vibrations, which are associated with hydroxyl groups on the carbon surface. These hydroxyl groups can enhance the hydrophilicity of the material and provide active sites for interactions with pollutant molecules. The absorption peak at 2934.16 cm^{-1} is attributed to C–H stretching vibrations originating from aliphatic carbon structures. Furthermore, the peak at 1581.75 cm^{-1} indicates the presence of C=C bonds, reflecting the aromatic carbon framework commonly found in activated carbon. Peaks at 1236.37 cm^{-1} and 580.91 cm^{-1} are assigned to C–O and C–C vibrations, respectively, suggesting the existence of oxygenated functional groups and a developed carbonaceous structure. These functional groups contribute to the adsorption capacity of activated carbon by facilitating interactions between the adsorbent surface and dye molecules.

In contrast, pure TiO_2 exhibits a relatively simpler FTIR spectrum dominated by metal–oxygen vibrations. Characteristic absorption bands at 600.94 cm^{-1} and 493.10 cm^{-1} are attributed to Ti–O–Ti stretching vibrations, which confirm the formation of the titanium dioxide

crystal framework. These bands are commonly observed in TiO_2-based materials and serve as indicators of the metal oxide structure. The distinct differences between the FTIR spectra of activated carbon and TiO_2 demonstrate that activated carbon possesses a more complex surface chemistry, whereas TiO_2 is characterized by an inorganic crystalline structure. The combination of these two materials in a composite is expected to integrate the high adsorption capacity of activated carbon with the photocatalytic activity of TiO_2, thereby enhancing the overall performance of the material in pollutant removal applications. (Mustafidah, 2022).

Table 2. 4 Identification of Vibrational Bands of TiO_2-Activated Carbon (Mustafidah, 2022)

Sample	Wavenumber (cm^{-1})	Functional Group
Activated Carbon	3674.95	O–H
	2934.16	C–H
	1581.75	C=C stretching
	1236.37	C–O
	580.91	C–C stretching
TiO_2	600.94 and 493.10	Ti–O–Ti
TiO_2-Activated Carbon	600.94 and 524.64	Ti–O–Ti
	1505.63	Ti–O–C

FTIR spectrum analysis of the TiO_2-activated charcoal composite material was carried out by comparing the spectra of each component, as shown in the FTIR spectrum image and summarized in the functional group identification table. Based on the data in Figure 4 and Table 2 from previous research, the TiO_2-activated charcoal composite shows absorption peaks at 600.94 cm^{-1} and 524.64 cm^{-1}, which represent Ti–O–Ti vibrations, as well as the emergence of a new peak at 1505.63 cm^{-1} attributed to the Ti–O–C bond. The emergence of the Ti–O–C group is a strong indication of a chemical interaction between TiO_2 and activated charcoal, not simply a physical mixture. Furthermore, changes in the position and intensity of the peaks compared to the starting material indicate a modification of the surface structure due to the composite synthesis process (Mustafidah, 2022).

The presence of the Ti–O–C bond in the TiO_2-activated charcoal composite indicates that activated carbon not only functions as a support but also interacts directly with the TiO_2 particles. This is in line with research that reports that the formation of Ti–O–C bonds can increase the stability of TiO_2 dispersions and expand the active area on the surface of the material. In addition, the presence of functional groups such as O–H and C–O in activated charcoal contributes to increasing the adsorption capacity of organic molecules through hydrogen interactions and van der Waals forces. Thus, the combination of the adsorptive properties of activated charcoal and the photocatalytic properties of TiO_2 can produce a synergy that increases the efficiency of dye degradation.

CHAPTER III
RESEARCH METHODOLOGY

3.1 Time and Place of Research

This research was conducted from October 2025 to February 2026 at the Inorganic Chemistry Laboratory, Maulana Malik Ibrahim State Islamic University of Malang.

3.2 Tools and Materials

The tools used in this research consisted of porcelain crucibles, a furnace, an oven, an analytical balance, beakers, measuring cylinders, glass funnels, a spatula, a mortar and pestle, an X-ray diffractometer (XRD), X-Ray Fluorescence (XRF), Energy-Dispersive X-ray (EDX), UV-Vis DRS spectrophotometer, Attenuated Total Reflectance–Fourier Transform Infrared (ATR-FTIR) and UV-Vis spectrophotometer. In addition, a UV light source was used in the photodegradation activity test.

The materials used in this research included oil palm shells, titanium dioxide (TiO_2) as a photocatalyst, and hydrochloric acid (HCl) as a chemical activator. Remazol Brilliant Blue R (RBBR) was used as a model pollutant, and distilled water was used as a solvent.

3.3 Research Design

This laboratory experimental study evaluates the ability of a TiO_2-activated carbon photocatalyst to degrade Remazol Brilliant Blue R (RBBR) dye. The research design includes several main stages: synthesis of activated carbon from oil palm shells, impregnation of TiO_2 into the activated carbon, testing of the activated carbon, characterization of the synthesized material, and photodegradation activity tests with variations in photocatalyst mass and dye concentration.

The synthesized photocatalyst was characterized using three primary methods: X-ray diffraction (XRD) to determine the crystal structure and phase of TiO_2, X-ray fluorescence (XRF) to analyze the morphology and elemental distribution on the composite surface, and ultraviolet-diffuse reflectance spectroscopy (UV-DRS) to assess the optical properties and band gap value. Following characterization, degradation tests were conducted by placing the photocatalyst in RBBR solution and exposing it to ultraviolet light.

Degradation effectiveness was evaluated by measuring the reduction in RBBR concentration using a UV-Vis spectrophotometer. The study employed variations in photocatalyst mass (0.01, 0.02, 0.03, 0.04, and 0.05 g) and initial dye concentrations (10, 20, 30, 40, and 50 ppm) to identify the optimum degradation conditions.

3.4 Research Stages

The stages of this research consist of:

1. Preparation of samples and proximate analysis of activated carbon derived from oil palm shells, including determination of moisture content, volatile matter, ash content, and fixed carbon.
2. Chemical activation of the prepared activated carbon from oil palm shells.
3. Synthesis of TiO_2-activated carbon composites using the impregnation method.
4. Characterization of materials using XRD, FTIR, XRF, EDX, and UV-Vis DRS.
5. Photodegradation experiments of Remazol Brilliant Blue R (RBBR) were conducted using TiO_2-activated carbon, with variations in catalyst mass and dye concentration.
6. Comparative analysis of catalyst mass, RBBR concentration, and photocatalyst mass was performed.
7. Activity tests were conducted using a UV–Vis spectrophotometer.
8. Data analysis.

3.5 Research Procedures

3.5.1 Preparation and Activation of Oil Palm Shell Carbon

Oil palm shells were cleaned of remaining fibers and pulp, then weighed (1 kg). The cleaned shells were ground into powder and dried in an oven at 110°C for 2 hours to remove moisture. The dried sample was then calcined in a furnace at 500°C for 3 hours to obtain charcoal. The hot charcoal was cooled in a desiccator to prevent moisture absorption (Babatunde et al., 2025).

Chemical activation was performed by sieving the charcoal to 200 mesh. The obtained powder was soaked in 1 M HCl for 4 hours to open pores and remove impurities. The sample was filtered and washed with distilled water until a neutral pH was achieved. The activated carbon was then dried at 350°C for 1 hour to obtain activated carbon ready for use as a support material (Hartanto & Ratnawati, 2010).

3.5.2 Moisture Content Test

One gram of the sample was placed in a pre-weighed crucible and dried at 110°C for 1 hour until a constant mass. After cooling in a desiccator, the sample was weighed. Moisture content (KA) was calculated using:

$$AC = \frac{a-b}{a} x100\% \quad \text{.....3.1}$$

where *a* is the mass before drying and *b* is the mass after drying (Manurung, 2019)

3.5.3 Volatile Matter Content

One gram of dried sample was heated in a furnace at 900°C for 15 minutes, cooled, and weighed. The volatile matter content (KZMM) was calculated as:

$$KZMM = \frac{b-c}{b} x100\% \quad (3.2)$$

where *b* is the initial mass and *c* is the mass after heating (Manurung, 2019)

3.5.4 Ash Content

One gram of sample was ashed in a furnace at 650°C for 4 hours. After cooling, the ash was weighed. Ash content (KAT) was calculated using:

$$KAT = \frac{d}{a} x100\% \quad (3.3)$$

where *a* is the mass before ashing and *d* is the mass after ashing (Manurung, 2019)

3.5.5 Fixed Carbon Content

Fixed carbon was calculated by:

$$KK = 100\% - (KA + KZMM + KAT) \quad (3.4)$$

3.5.6 Synthesis of TiO_2-Activated Carbon

TiO_2-Activated Carbon was synthesized using the impregnation method. Activated carbon and TiO_2 were weighed at a 50:50 w-w mass ratio and mixed in Aquademin solvent until fully immersed. The mixture was stirred for 6 hours, then left to soak at room temperature for 12 hours to achieve a homogeneous suspension. Subsequently, the mixture was filtered and dried in an oven at 100°C for 2 hours. The dried material was then heated in a furnace at 550°C for 3 hours and cooled in a desiccator to room temperature to obtain the impregnated TiO_2-Activated Carbon material (Sugandi et al., 2024).

3.5.7 Material Characterization

3.5.7.1 Identification of the Crystal Structure of TiO_2-Activated Carbon Photocatalyst Using X-Ray Diffraction (XRD)

X-ray diffraction (XRD) was employed to determine the crystal structure and phase of the synthesized TiO_2-palm shell activated carbon material. The analysis utilized an XRD instrument with Cu-Kα radiation (λ = 1.5406 Å), operating at 40 kV and 30 mA, and scanned over a 2θ range of 5–60°. The fine powder sample was mounted in a sample holder and irradiated with X-rays to generate a diffractogram. The resulting diffraction peak patterns were compared with JCPDS standard data to identify the crystal phases of TiO_2 and the activated carbon support (Al'Adawiyyah, 2022).

3.5.7.2 Identification of the Elemental Composition of TiO_2-Activated Carbon Photocatalyst Using X-Ray Fluorescence (XRF) and Energy-Dispersive X-Ray Spectroscopy (EDX)

Identification using X-Ray Fluorescence (XRF) aims to determine the elemental composition of TiO_2-palm shell activated carbon photocatalysts. A finely powdered sample is placed in a sample holder and then irradiated with X-rays. The XRF instrument detects the fluorescence emissions emitted by the atoms composing the sample. The resulting data is a fluorescence spectrum indicating the percentage of elements in the material (Al' Adawiyyah, 2022).

Energy-Dispersive X-ray (EDX) analysis is performed to determine the elemental composition of the sample surface. The sample is first placed on a holder and analysed using an SEM instrument equipped with an EDX detector. The sample surface is then bombarded with an electron beam to produce characteristic X-rays for each element. The resulting energy spectrum is analysed to identify the type of element based on the position of the energy peak, as well as to determine the percentage of elemental composition in the form of weight percent (wt%) or atomic percent (at%) displayed by the EDX software (Skoog et al., 2016).

3.5.7.3 Determination of Band Gap Energy in TiO_2-Palm Shell Activated Carbon Photocatalysts via UV-Vis Diffuse Reflectance Spectroscopy (UV-Vis DRS)

UV-Vis DRS is employed to determine the band gap energy of TiO_2-palm shell activated carbon photocatalysts. The powder sample is placed in a sample holder, and its reflectance is measured within the 200–800 nm wavelength range. The resulting reflectance data are transformed using the Kubelka-Munk equation and analyzed with the Tauc plot method, plotting $[F(R)\cdot hv]^n$ against photon energy (hv). The band gap energy is identified at the intersection of the linear portion of the curve with the photon energy axis. This value serves as a parameter for evaluating the photocatalytic performance of the material (Al' Adawiyyah, 2022).

3.5.8 Degradation Test of Remazol Brilliant Blue R with Variations in TiO_2-Activated Carbon Mass and RBBR Concentration

Photodegradation experiments were conducted by preparing 25 mL of Remazol Brilliant Blue R (RBBR) solution at an initial concentration of 20 ppm in four 100 mL beakers. TiO_2-palm shell activated carbon photocatalyst was added to each solution at concentrations of 10 mg, 20 mg, 30 mg, 40 mg, and 50mg. The mixtures were placed in a photoreactor and irradiated with UV light for degradation analysis, and were placed in a dark place for an adsorption test for 120 minutes under continuous stirring. After irradiation, the degradation solution was separated from the photocatalyst by centrifugation at 4000 rpm for 20 minutes, followed by filtration to remove catalyst residues. The residual dye concentration was analyzed

using a UV-Vis spectrophotometer at the maximum wavelength (λmax) of RBBR. All experiments were conducted in triplicate to ensure data validity and reproducibility. For evaluating the effect of initial RBBR concentration, the same procedure as in the photocatalyst mass variation was used. RBBR solutions were prepared at different initial concentrations of 10, 20, 30, 40, and 50 ppm in 25 mL volumes. The TiO_2-palm shell activated carbon photocatalyst was added at the optimum mass obtained from the previous experiment.

The mixtures were subjected to adsorption–desorption equilibrium in dark conditions for 120 minutes under continuous stirring, followed by UV irradiation in a photoreactor for degradation analysis. After irradiation, the solutions were centrifuged at 4000 rpm for 20 minutes and filtered to remove photocatalyst residues. The residual dye concentration was measured using a UV–Vis spectrophotometer at the maximum wavelength (λmax) of RBBR. All experiments were performed in triplicate to ensure data validity and reproducibility.

3.5.9 Evaluation of Remazol Brilliant Blue R Degradation Efficiency at Varying RBBR Concentrations and Optimal TiO_2-Activated Carbon Mass

The degradation efficiency of Remazol Brilliant Blue R by TiO_2-activated carbon was evaluated by placing 25 mL of the dye solution in a 100 mL beaker. Five experimental conditions were assessed:

a. RBBR solution exposed to UV irradiation for 120 minutes
b. RBBR solution with the optimal mass of TiO_2, subjected to UV irradiation for 120 minutes
c. RBBR solution with the optimal mass of activated carbon, subjected to UV irradiation for 120 minutes
d. RBBR solution containing both TiO_2-AC at optimal concentrations, subjected to UV irradiation for 120 minutes
e. Conditions a, b, c, and d were also repeated in the absence of UV irradiation (in the dark).

3.5.10 Evaluation of Reusability Performance of TiO_2 and TiO_2-AC Photocatalyst

The reusability test of the TiO_2-AC photocatalyst was conducted under optimum operating conditions obtained from the previous experiments (10 ppm with 30 mg Mass). After each photocatalytic remediation process, the photocatalyst was separated from the solution using filtration, washed several times with distilled water to remove residual dye molecules adsorbed on the catalyst surface, and then dried at 100 °C for 2 hours. The recovered photocatalyst was subsequently reused for the next remediation cycle under the same experimental conditions. In each cycle, the remediation efficiency of Remazol Brilliant Blue R (RBBR) was determined by measuring the absorbance of the solution using a UV–Vis spectrophotometer at the maximum wavelength (λmax).

3.5.11 Data Analysis

1. The moisture content of palm shell activated carbon is calculated using the formula:

   $AC = \frac{a-b}{a} x100\%$ 3.1

   where a = mass before drying, and b = mass after drying.

2. The volatile matter content of activated carbon (VAC) is calculated using the formula:

   VAC= $\frac{b-c}{b} x100\%$ 3.2

   where b = mass of the starting material, and c = mass after determining the moisture content.

3. The ash content of activated carbon is calculated using the formula:

   ACC=$\frac{d}{a} x100\%$ 3.3

   where a = mass before ashing, and d = mass after ashing.

4. The bound carbon content is determined using the equation:

   BC = 100% - (AC+VAC+ACC) 3.4

   Bound carbon = 100% - (moisture content + volatile matter content + ash content)

5. X-Ray Diffraction (XRD) data is in the form of a diffractogram, which is then compared with JCPDS TiO_2 standard data to determine the crystal phase (anatase, rutile, or brookite) and its crystal structure using the Origin and Expert applications.

6. X-Ray Fluorescence (XRF) and Energy-Dispersive X-Ray Spectroscopy (EDX) data are in the form of a table of the percentage of elements contained in the TiO_2-AC photocatalyst. These results are used to determine the chemical composition, the level of TiO_2 impregnation, and the presence of other elements that may play a role in photocatalytic activity.

7. UV-Vis Diffuse Reflectance Spectroscopy (UV-DRS) data are in the form of a diffuse reflectance spectrum, which is then analyzed using the Kubelka-Munk method. The data was used to determine the band gap energy value of the TiO_2-activated carbon photocatalyst by creating a Tauc plot and comparing it with the Origin and Expert applications.

8. The percentage degradation of Remazol Brilliant Blue R (RBBR) was calculated using the absorbance values measured by the UV-Vis spectrophotometer. The absorbance values were converted to concentration using the linear regression equation y=ax+by = ax + by=ax+b, where the x-axis = concentration (ppm) and the y-axis = absorbance. The percentage degradation was determined using the formula:

   % Degradation= $\frac{C0-Ct}{C0} x100\%$ 3.5

   where C_0 = initial concentration of RBBR, and C_t = concentration after photodegradation. The following data is presented in tabular form for analysis and comparison of results:

Table 3. 1 Effect of TiO_2-AC Photocatalyst Mass Variation on RBBR Degradation

No	TiO_2-AC Photocatalyst Mass (mg)	RBBR Concentration (ppm)	Degradation Percentage (%)
1	10	20	
2	20	20	
3	30	20	
4	40	20	
5	50	20	

Table 3. 2 Effect of Initial RBBR Concentration on Degradation Percentage

No	RBBR Concentration (ppm)	Optimum TiO_2-AC Photocatalyst Mass (mg)	Degradation Percentage (%)
1	10		
2	20		
3	30		
4	40		
5	50		

Table 3. 3 Comparison of RBBR Degradation Effectiveness by Various Systems

No	Optimum Mass and Concentration	Irradiation Condition	Degradation Percentage (%)
1	RBBR without catalyst	Without irradiation	
2	RBBR without catalyst	With irradiation	
3	Activated Carbon	Without irradiation	
4	Activated Carbon	With irradiation	
5	TiO_2	Without irradiation	
6	TiO_2	With irradiation	
7	TiO_2-AC	Without irradiation	
8	TiO_2-AC	With irradiation	

9. The adsorption capacity of activated carbon and TiO_2-AC was calculated using the equation:

   $Qe = (C0 - Ce)\ x\ \frac{V}{m}$ 3.6

   Where Qe=equilibrium adsorption capacity, C0= initial concentration, Ce=remaining adsorbate concentration, V=total solution volume, and m = adsorbent mass.

10. The degradation capacity of RBBR by the catalyst was calculated using the equation:

    Activity reductions (%) = $\frac{\%\ Initial\ Degradation - \%\ Degradation\ After\ Use)}{Initial\ Degradation}\ x\ 100\%$ 3.7

CHAPTER IV
RESULT AND DISCUSSION

4.1 Preparation and Activation of Palm Oil Shell

Palm shell activated carbon production commenced with the preparation of palm shell waste as the raw material. The palm shell waste utilized in this study was obtained from a company in the Hanau District, Seruyan Regency, Central Kalimantan. The carbonization process at 500°C changes the oil palm Shell material. This is indicated by the color change from light brown to deep black, indicating that organic components such as cellulose, hemicellulose, and lignin have decomposed and formed a carbon structure. The use of 500°C is also crucial because, within this temperature range, carbon formation occurs optimally, resulting in charcoal with a higher carbon content. Physically, the carbonization product exhibits a more brittle texture and a darker color, indicating successful carbon conversion. This resulting material then serves as a good foundation for the next stage, particularly as a TiO_2 support, where its carbon structure provides a larger active surface area (Hartanto & Ratnawati, 2010).

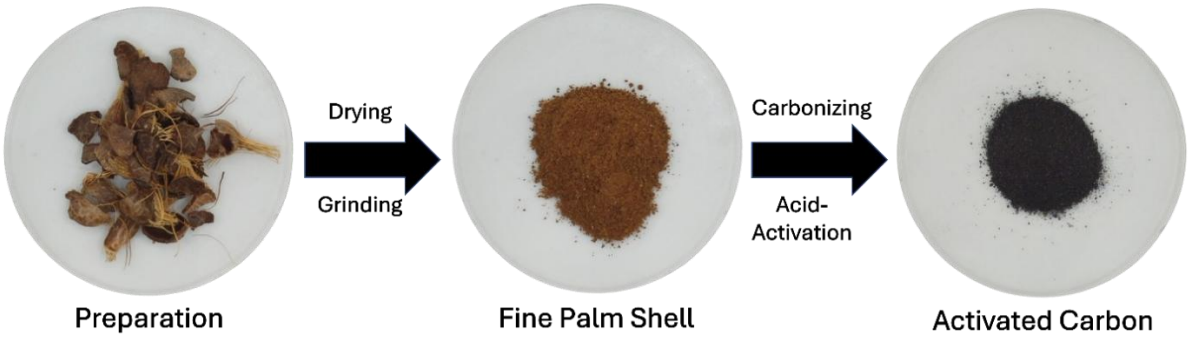

Figure 4. 1 a) Palm shell waste before preparation. b) After grinding and oven-drying. c) After carbonization.

Chemical activation was subsequently performed to enhance the physicochemical properties of the carbon material. The activation process removes residual impurities and opens previously blocked pores, thereby increasing pore volume and surface area. As a result, more active sites become available for TiO_2 deposition and pollutant adsorption during photocatalytic applications. Therefore, activated carbon derived from palm shells is expected to serve not only as a support material for TiO_2 but also as an adsorbent that enhances overall remediation performance through a synergistic mechanism of adsorption and photocatalysis (Diaz et al., 2022).

4.2 Proximate Analysis of Activated Carbon Derived from Oil Palm Shell

A proximate analysis of the activated carbon was performed to assess its quality. Furthermore, proximate analysis was performed to determine the physical properties of the activated carbon to be used as a support for TiO_2 photocatalysts. Parameters in this proximate analysis include air content, volatile matter content, ash content, and bound carbon content. The quality reference for this proximate analysis of activated carbon is SNI 06-3730-1995, which sets minimum standards for activated carbon (Pangestuti et al., 2025). This parameter is one of the key test standards for assessing the quality of activated carbon based on its adsorption capacity. This ability is important for activated carbon to optimise its performance as a supporting material for TiO_2 photocatalysts (Oktaviani et al., 2024).

Table 4. 1 Proximate Analysis Results of Activated Carbon

Parameter	Replicate	Mass (g)	Average Mass (g)	Result (%)	SNI 06-3730-1995 Standard
Moisture Content	1 2 3	0.9497 0.9500 0.9507	0.9501	5.05	Max. 15%
Volatile Matter (VM)	1 2 3	0.9370 0.9191 0.9153	0.9238	2.77	Max. 25%
Ash Content	1 2 3	0.0781 0.0776 0.0875	0.0811	8.10	Max. 10%
Fixed Carbon	-	-	-	84.08	Min. 65%

Based on Table 4.1, the proximate analysis results for activated carbon from oil palm shells meet all Indonesian National Standards stipulated in SNI 06-3730-1995. Activated carbon from oil palm shells meets the standard parameters, with a moisture content of 5.05%, with a maximum standard of 15%; volatile matter content of 2.77%, with a maximum standard of 25%; ash content of 8.10%, with a maximum standard of 10%; and fixed carbon content of 84.08%, with a minimum standard of 65% according to SNI 06-3730-1995.

Activated carbon from oil palm shells has a moisture content of 5.05%, indicating low moisture. Water content in activated carbon can reduce its performance by clogging its pores, thereby inhibiting adsorption on its surface (Pastor et al., 2025). With its low water content, activated carbon from palm kernel shells can have more open pores and maximize the adsorption of RBBR dyes.

Volatile matter content (VM) is a test parameter used to assess the extent of volatile matter resulting from non-carbon compounds adhering to the surface of activated carbon, particularly O atoms tightly bound to C atoms as CO_2 and CO. In activated carbon from palm

kernel shells, the volatile matter content was 2.77%, with a maximum of 25%. This indicates a minimal amount of non-carbon impurities present in the pores of the activated carbon. These non-carbon compounds can act as impurities that clog the pores of the activated carbon, reducing its effectiveness in adsorbing contaminants in water (Masthura et al., 2018).

Proximate analysis of activated carbon from palm kernel shells showed an ash content of 8.10%. This ash content is usually caused by inorganic impurities such as calcium, magnesium, and potassium (Pangestuti et al., 2025). The ash content of 8.10% remains relatively low and is below the maximum limit set by the Indonesian National Standard (SNI). The ash content of palm shell activated carbon significantly impacts the adsorption and photocatalytic processes of RBBR. This is because the high content of inorganic materials dispersed on the surface of the activated carbon can cover the active sites, thereby reducing its effectiveness as a photocatalyst development material (Zulkania et al., 2020).

Fixed carbon was determined by subtracting the sum of moisture, ash, and volatile matter from 100%. In this study, the fixed carbon yield was 84.08%, exceeding the minimum SNI limit of 65%. This figure is considered sufficiently high, indicating high purity of the activated carbon and its suitability for use as a support material for TiO_2 photocatalysts. Fixed carbon is pure activated carbon found in palm flour activated carbon. A higher purity value of activated carbon indicates a higher number of active sites (Pastor et al., 2025). This also increases the adsorption efficiency of activated carbon, making it a good photocatalyst support material (Oktaviani et al., 2024).

The favorable proximate characteristics of palm shell activated carbon indicate that it can be a good support for TiO_2 photocatalysts. The low water and ash content in activated carbon creates space within the pores, allowing more TiO_2 to be evenly dispersed. Furthermore, the low volatile matter content indicates fewer inorganic impurities, creating more active sites for the adsorption of RBBR dye and leading to a more efficient degradation process around TiO_2 (Kusdarini & Budianto, 2022). High purity is also an advantage of palm-shell activated carbon. The higher the carbon purity of activated carbon, the better it can adsorb dyes and serve as a support for TiO_2 photocatalysts (Parvathiraja et al., 2022). The results obtained in this study align with previous research, which states that good proximate content in activated carbon also confers good properties as a supporting material, such as unclogged pores, a large number of active sites, minimal impurities, and high carbon purity. Ali et al. (2025) reported that activated carbon has a significant impact on the surface area and pore volumes of up to 268,789 m^2-g after activation with HCl. Zulkania et al. (2020) also reported that activated carbon meeting SNI standards has a relatively high adsorption capacity, achieving 99.50% removal at 9,950 mg-g.

4.3 Synthesis of TiO_2-Activated Carbon

The TiO_2-AC composite was synthesized via wet impregnation. This method was used to disperse TiO_2 onto activated carbon. Wet impregnation was selected because it is a simple,

solvent-efficient method that is both easier and more cost-effective (Saputra, 2018). Impregnation also shows good dispersion of TiO_2 during activated carbon development, thereby maximizing TiO_2 surface area and improving degradation. The mass ratio between TiO_2 and activated carbon used was 50:50 (wt%). This ratio was chosen to maximize the performance of activated carbon as an adsorbent and TiO_2 as a catalyst in the remediation of RBBR dye wastewater. Demineralized water was selected as the solvent to minimize mineral and foreign ion contamination and to enhance TiO_2 penetration into the carbon pores without leaving salt residues (Řepecká et al., 2026).

The prolonged stirring process was intended to improve the dispersion of TiO_2 particles on the activated carbon surface and enhance their penetration into the pore structure, thereby promoting better contact between the photocatalyst and adsorbent phases. A more homogeneous TiO_2 distribution is expected to increase the number of active sites and improve the synergistic effect between adsorption and photocatalytic activity. Calcination at 550 °C also plays an important role in strengthening the interaction between TiO_2 and activated carbon. The use of a closed crucible during calcination is intended to prevent excessive oxidation of the carbon phase by limiting oxygen exposure. Excessive oxidation can form functional groups with excess oxygen on the carbon surface, thereby increasing the hydrophilic properties of activated carbon. As a result, water molecules can accumulate on the carbon surface and within the micropores, reducing the accessibility of dye molecules to adsorption sites. Additionally, these excess oxygen functional groups can weaken the π–π interactions between the activated carbon and aromatic dye molecules, thereby reducing the material's adsorption performance (Marczewska et al., 2025). The selected calcination temperature and duration were sufficient to remove residual moisture and promote structural stabilization without inducing phase transformation of anatase TiO_2 into rutile (Subagja et al., 2014).

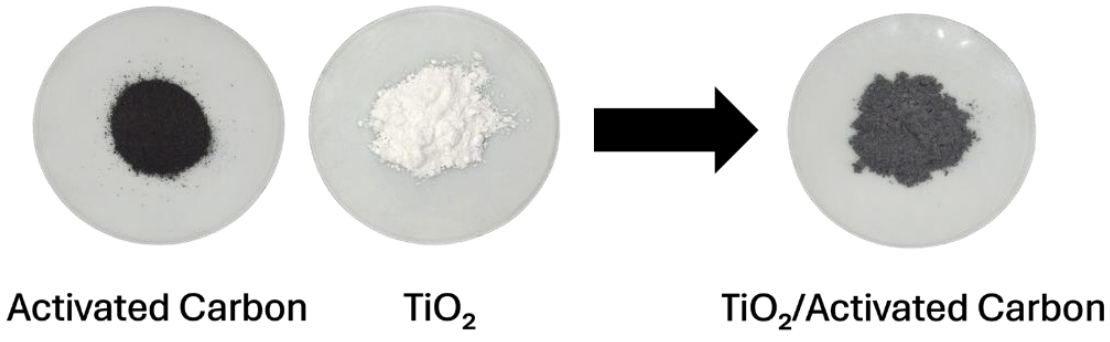

Figure 4. 2 Synthesis of TiO_2-AC composite (50:50 wt%) through wet impregnation and thermal treatment at 550 °C.

The synthesis results of TiO_2-activated carbon show very significant differences compared to before the synthesis. Before synthesis, the activated carbon was dark black with a very soft, fine texture. Meanwhile, TiO_2 was a white powder that tended to agglomerate. After

synthesis, the TiO_2-AC composite exhibited different physical properties. The TiO_2-AC became light gray in color with a fine texture, and no visible macroscopic agglomeration was observed.

Although the initial composition ratio of TiO_2 and activated carbon is 50:50, the material can still be classified as a composite because composites are generally defined as systems consisting of two or more distinct constituent phases that remain identifiable in the final structure. Therefore, composite classification is not determined by a specific composition ratio, but rather by the coexistence and interaction of different material phases. In the TiO_2-AC system, activated carbon and TiO_2 remain as separate phases and do not form new crystalline compounds. The interaction between these two components is largely physical, involving the adhesion and dispersion of TiO_2 particles on the surface of activated carbon via impregnation. Since activated carbon does not replace Ti atoms in the TiO_2 crystal lattice, the material cannot be classified as carbon-doped TiO_2. Instead, each constituent retains its own structural identity and intrinsic properties. With proper separation procedures, the TiO_2 and activated carbon phases can theoretically be distinguished and reisolated, a characteristic of composite materials. Thus, TiO_2-AC materials are more accurately described as composites rather than doped semiconductor systems. In this system, activated carbon acts as a supporting adsorption matrix, while TiO_2 functions as the active photocatalytic phase (Chinta, 2017).

The synthesis of the TiO_2-AC composite aims to enhance interfacial reactions between the composite and RBBR dye wastewater. The interfacial reaction between the TiO_2-AC catalyst and RBBR waste involves both adsorption and charge-transfer processes. Activated carbon acts as an adsorbent, binding RBBR via pore filling, π–π interactions, electrostatic forces, and possible hydrogen-bond formation (Yue et al., 2024). This adsorption process causes dye molecules to accumulate around the TiO_2 surface, which possesses photocatalytically active sites, and prevents agglomeration of TiO_2 particles (Vargas & Núñez, 2009). The successful formation of the TiO_2-activated carbon composite was further confirmed by structural and compositional analyses, as discussed in the following section.

4.4 Characterization of TiO_2 -Activated Carbon

4.5.1 Crystal Structure Analysis of TiO_2- Activated Carbon using X-Ray Diffraction (XRD)

The X-ray Diffraction (XRD) analysis was performed to investigate the crystalline structure, phase composition, and crystallinity of the synthesized TiO_2-Activated Carbon (TiO_2-AC) composite. This characterization is important for confirming whether the crystal structure of TiO_2 is preserved after the composite synthesis process and for identifying the presence of crystalline phases within the material. In addition, XRD analysis can provide information on possible structural changes, phase transformations, or the formation of new phases resulting from interactions between TiO_2 and activated carbon. The diffraction pattern of the sample is presented in Figure 4.3. Measurements were carried out over a 2θ range of approximately 5–90°.

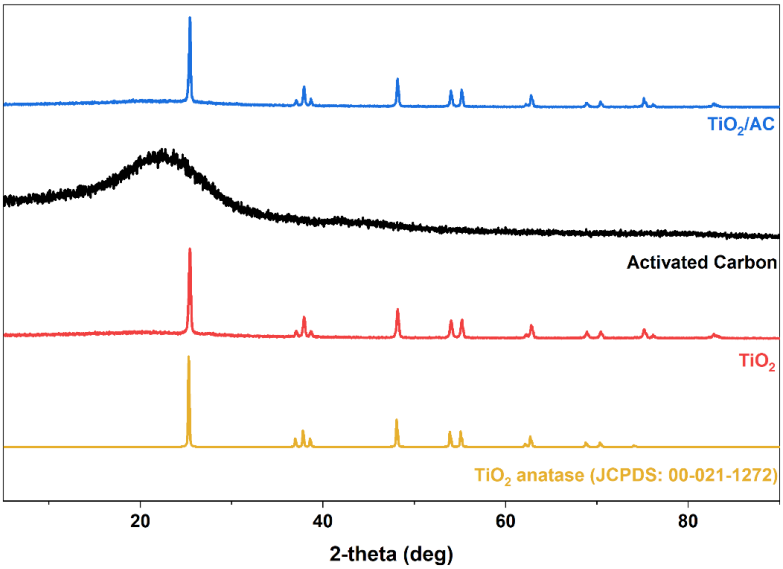

Figure 4. 3 Diffractogram XRD from Activated Carbon, TiO_2, and TiO_2 -AC

Based on Figure 4.3, it can be seen that in the XRD analysis results, activated carbon exhibits a main absorption peak at 2θ around 22.9, which has a broad peak characteristic. This absorption indicates that the activated carbon in this study is amorphous and lacks a crystalline structure, as it does not exhibit sharp, characteristic crystalline peaks. The presence of an amorphous structure in activated carbon can serve as a good support material for TiO_2 because it can inhibit the formation of the rutile phase and maintain the anatase phase (Du et al., 2019). Furthermore, the presence of a porous, amorphous structure in activated carbon enhances photocatalytic efficiency by enabling effective ion adsorption on its surface, thereby optimizing the performance of active sites in the TiO_2-AC photocatalyst (Xia et al., 2014). Meanwhile, TiO_2 exhibits sharp dominant peaks at 2θ of 25.41°, 37.92°, 48.16°, and 54.02°, which are characteristic of the anatase phase (Ahmed et al., 2025). Furthermore, the TiO_2 peaks do not show the absorption bands of rutile and are consistent with the JCPDS data for anatase TiO_2 (JCPDS:00-021-1272). This indicates that the material used in this study has a predominantly anatase crystal structure.

The XRD analysis of the TiO_2 -AC synthesis shows a main peak at 2θ = 25.43°. However, the crystallinity peak in TiO_2-AC exhibits decreased intensity and a slight shift due to interactions between TiO_2 and activated carbon (Shao et al., 2013a). In the TiO_2-AC synthesis results, the dominant anatase phase remains evident, with absorption at 2θ around 25°. Based on the XRD analysis results, no absorption peaks for the rutile phase of TiO_2 (2θ = 27°) or the brookite phase (2θ = 30°) were observed (Y. Wang et al., 2015). This indicates that the TiO_2-AC synthesis successfully retained the dominant anatase crystal structure. The anatase phase of TiO_2 is commonly used in photocatalytic systems. The anatase crystal structure of TiO_2 offers a larger surface area and longer electron-hole lifetimes than other phases (Žerjav et al., 2022).

Although the TiO_2-AC composite was synthesized at a 50:50 ratio, the diffraction peak of activated carbon was not clearly observed in the composite diffractogram. This is because activated carbon is mostly amorphous and generally produces a broad peak with low intensity around 2θ ≈ 20–26° (Shao et al., 2013). In contrast, anatase TiO_2 exhibits sharp and intense diffraction peaks due to its high crystallinity, especially near 25° (Chen et al., 2014). Previous studies also reported that increasing TiO_2 loading can gradually cover the diffraction peak of activated carbon due to the accumulation and dispersion of TiO_2 particles on the carbon surface (Yue et al., 2024). Furthermore, the absence of significant peak shifts or the appearance of new crystalline phases suggests that the crystal structure of TiO_2 remained largely unchanged after composite synthesis. This observation may indicate that activated carbon was not significantly incorporated into the TiO_2 crystal lattice but instead remained as a separate amorphous phase that physically supports the TiO_2 particles. Therefore, the interaction between TiO_2 and activated carbon is likely dominated by physical contact rather than lattice substitution or extensive chemical incorporation. These findings are consistent with the characteristics of TiO_2-AC composites reported in previous studies, in which the anatase structure of TiO_2 remained unchanged after deposition onto activated carbon surfaces.

In addition to the crystal phase, the crystallinity of TiO_2 photocatalysts is a key factor in their effectiveness. The smaller the crystallinity of the composite, the larger the surface area available for contact with the dye, thereby optimizing dye degradation. Smaller crystallite sizes are generally associated with a higher density of exposed surface active sites, which can enhance interactions between the photocatalyst and pollutant molecules. Moreover, the increased surface-to-volume ratio may enhance photocatalytic performance by providing more reaction sites for the generation of reactive oxygen species. Crystal size can be predicted from XRD data using the Scherrer equation, where the FWHM value is inversely proportional to the sample's crystal size. The larger the FWHM value, the smaller the sample's crystal size (Manh et al., 2023).

Table 4. 2 Crystallite Size Calculation Using Scherrer and Monshi–Scherrer Equation

Sample	Main Peak 2θ (°)	FWHM (rad)	Slope	Intercept	Crystallite Size (nm) (Scherrer)	Crystallite Size (nm) (Monshi–Scherrer)
TiO_2 Anatase	25.414	0.00412	-0.863	-5.511	32.8	34.28
TiO_2-AC	25.432	0.00337	1.049	-5.969	40.1	54.2

Table 4.2 shows that the crystallite size of TiO_2-AC is larger than that of pure anatase TiO_2, as determined by the Scherrer and Monshi–Scherrer methods. The crystallite size calculated using the Scherrer equation increased from 32.8 nm for anatase TiO_2 to 40.1 nm

for TiO_2-AC. Similarly, the Monshi–Scherrer method yields crystallite sizes of 34.28 nm and 54.2 nm for anatase TiO_2 and TiO_2-AC, respectively.

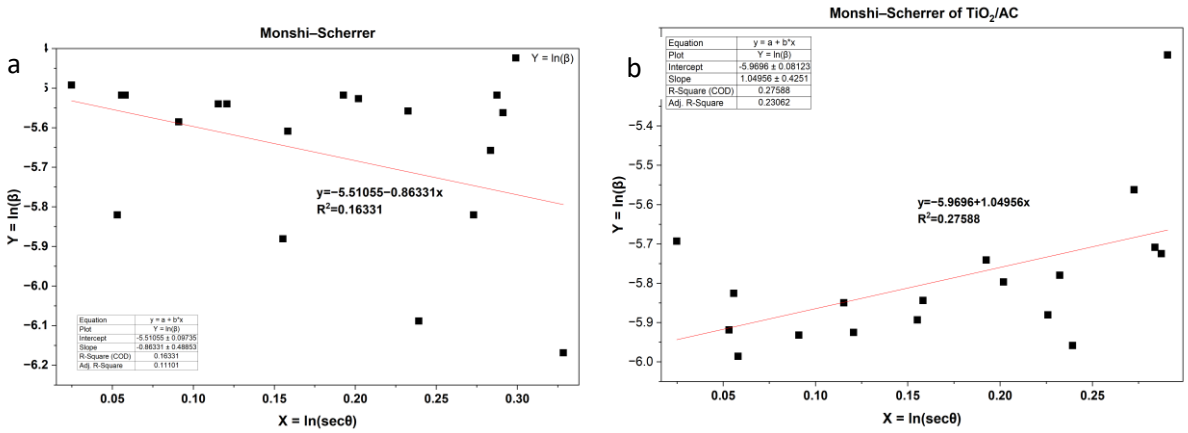

Figure 4. 4 Monshi–Scherrer Plot a)TiO_2 and b)TiO_2-AC

Figure 4.4 shows the analysis of the Monshi–Scherrer method using multiple diffraction peaks, based on the relationship between ln(β) and ln(1-cosθ), yielding a more representative estimate of the crystallite size than the conventional single-peak Scherrer approach (Monshi et al., 2012). The slope and intercept values obtained from the regression analysis indicate the quality of the linear fit used in determining the crystallite size. The larger crystallite size and narrower diffraction peaks observed in the TiO_2-AC composite indicate an increase in crystallinity following composite formation. This increase in crystallinity can be attributed to interactions between TiO_2 and activated carbon during calcination, which promote crystal growth and particle agglomeration (Li et al., 2007). Additionally, activated carbon can influence TiO_2 crystal growth, potentially increasing TiO_2 particle size (Kumar et al., 2022). Despite the increase in crystal size, the TiO_2-AC composite remains within the nanocrystalline range (<100 nm), which is beneficial for photocatalytic applications. Nanocrystalline TiO_2 provides a relatively high surface area, thereby enhancing interactions between the photocatalyst and dye molecules and improving photocatalytic degradation performance.

Even though the Monshi–Scherrer plot shows a relatively low coefficient of determination (R^2), this does not mean that the estimated crystallite size results are invalid. Monshi et al. (2012) also reported data dispersion and deviations from the ideal linear relationship in this method. These conditions may be caused by several factors, such as instrument broadening, overlapping diffraction peaks, and material structural inhomogeneity. The Monshi–Scherrer method was developed to reduce errors that may arise when crystallite size is calculated from a single diffraction peak. Therefore, this method uses multiple diffraction peaks, which are then analyzed via linear regression. In this method, the crystallite size is determined based on the intercept value of the regression result, while the R^2 value only

indicates how well the data follows the linear relationship. Thus, the intercept value becomes a more important parameter in determining the crystallite size compared to the R^2 value.

The XRD analysis results in this study are consistent with previous research reporting that TiO_2 has a dominant anatase phase with a main diffraction peak at approximately 25° in the 2θ angle. In a study conducted by Le et al. (2024), TiO_2-activated carbon also exhibited an anatase phase with a crystallite size of approximately 21 nm and uniform TiO_2 distribution on the activated carbon surface. Furthermore, the presence of activated carbon in the composite did not alter the TiO_2 crystal structure but did enhance particle dispersion. Furthermore, the decrease in peak intensity in the TiO_2-activated carbon composite indicates an interaction between TiO_2 and activated carbon, as well as improved TiO_2 dispersion on the carbon surface. This aligns with the study by Yue et al. (2024), which reported that TiO_2 is uniformly distributed on the activated carbon, thereby increasing the number of active sites available for photocatalysis. The crystal size obtained in this study is also in the nanometer range, approximately 32-54 nm, which is consistent with TiO_2 crystal sizes reported in previous studies, ranging from 18-50 nm. This small crystal size can increase the surface area and photocatalytic activity (Omri & Benzina, 2019).

4.5.2 Elemental Composition Analysis of TiO_2- Activated Carbon using X-Ray Fluorescence (XRF) and Energy Dispersive X-ray Spectrometry (EDX)

The composition of the TiO2-AC material was analyzed to evaluate the success of synthesizing TiO_2 on activated carbon via impregnation. The structural composition analysis of TiO_2-AC was performed using two different chemical instruments: XRF to determine the metal oxide composition of the photocatalyst and EDX to determine the carbon and oxygen composition of the photocatalyst. The composition of the photocatalyst plays a crucial role in determining the catalyst's effectiveness.

Table 4. 3 Elemental composition of samples based on XRF analysis (%)

Component	Before Activation (%)	After Activation (%)	TiO_2-Activated Carbon (%)
SiO_2	18.00	51.00	0.70
P_2O_5	5.20	7.90	0.30
K_2O	32.60	2.50	0.13
CaO	22.80	9.61	0.21
TiO_2	0.35	0.58	97.22
Fe_2O_3	17.40	10.40	0.23

Based on Table 4.3, the XRF characterization results for activated carbon before and after acid activation show a very significant decrease in the amount of metal oxides. The levels of potassium oxide, calcium oxide, and iron(II) oxide decreased drastically. K_2O in the carbon before activation showed a percentage of 32.60%, while CaO and Fe_2O_3 decreased from 22.80% and 17.40%, respectively, to only 9.61% and 10.40%. Meanwhile, the P_2O_5 and TiO_2

compounds showed a slight increase due to changes in the total amount of oxides, which in turn altered their percentages. The decrease in K_2O and CaO contents after HCl activation indicates the removal of inorganic mineral impurities via acid washing and leaching. Previous studies have reported that alkali and alkaline earth metal ions, such as potassium and calcium, can be removed via ion exchange with H^+ ions from HCl. During activation, potassium- and calcium-containing compounds are converted into water-soluble chloride salts, allowing them to dissolve and be removed during the washing process. Therefore, potassium and calcium are suggested to be dissolved in the form of KCl and $CaCl_2$, resulting in the significant reduction of K_2O and CaO composition after activation (Wang et al., 2022).

The SiO_2 content increased drastically from 18% to 51%. This increase occurred because silica has low solubility in common acids such as HCl; therefore, when activated with HCl, the activated carbon still contains a significant amount of silica (Tsaousi et al., 2023). These results demonstrate the success of activating oil palm shell-derived activated carbon in removing inorganic impurities. With a reduction in inorganic impurities that can clog the pores of the activated carbon, the total number of active sites on the activated carbon will also increase, thereby enhancing the photocatalyst's degradation efficiency (Zulkania et al., 2020).

The results of the compositional characterization of TiO_2-AC indicate that TiO_2 is highly dominant, accounting for 97.22%. This figure is quite high and makes TiO_2 the dominant metal oxide in the TiO_2-AC system. This indicates the successful synthesis of TiO_2 with palm shell activated carbon, resulting in the TiO_2-AC composite. The dominance of TiO_2 and the minimal impurities in the activated carbon will enhance photocatalytic degradation efficiency because it possesses more active sites that are not blocked by impurities. However, XRF testing has a limitation: it can only determine the composition of metal oxides in the sample and cannot identify the composition of other compounds within the TiO_2-AC catalyst. Therefore, additional supporting instruments such as EDX are required to determine the composition of carbon and other compounds.

Table 4.4 Elemental composition of TiO_2-activated carbon based on EDX analysis

Element	Energy (keV)	Mass (%)
C	0.277	67.73
O	0.525	8.81
Ti	4.508	23.45
Total		100.00

The results of compositional analysis using an EDX instrument show that the surface of the catalyst material is dominated by carbon at 67.73%, followed by Ti at 23.45% and O at 8.81%. The dominant carbon content indicates that activated carbon still governs the composite's surface characteristics and serves as the supporting matrix for TiO_2 particles. This condition suggests that TiO_2 particles are dispersed on the carbon framework rather than

completely covering the activated carbon surface. The porous structure and high surface area of activated carbon provide adsorption sites for dye molecules as well as attachment sites for TiO_2, allowing the photocatalytic reaction to occur near the active sites of TiO_2. Furthermore, the relatively low Ti content may indicate partial agglomeration of TiO_2 particles, resulting in non-uniform dispersion on the carbon surface. Similar findings were reported by El-Salamony et al. (2017), who observed that TiO_2 particles were distributed throughout the activated carbon framework even in $50TiO_2$–AC composites, confirming the role of activated carbon as the support material.

The EDX analysis showed that carbon was the dominant element in the TiO_2-AC composite, with a mass percentage of 67.73%, while Ti was detected at 23.45%. These results differ considerably from the XRF analysis, which indicated a TiO_2 content of 97.22% and a substantially lower carbon composition. The discrepancy between the two techniques can be attributed to their different analytical principles and detection areas. According to Gavenda and Gedeon (2022), XRF provides bulk compositional analysis by examining a larger volume of material and is therefore representative of the overall composition of the sample. In contrast, EDX primarily analyzes a localized region near the sample surface and is highly dependent on the selected observation area during SEM characterization.

The high carbon content detected by EDX suggests that activated carbon predominantly covers the analyzed surface region of the composite. This observation is consistent with the porous structure and high specific surface area of activated carbon, which tends to occupy a large proportion of the exposed surface. During SEM-EDX measurements, the electron beam interacts mainly with the outer layer of the material; consequently, the detected elemental composition reflects surface characteristics rather than the overall bulk composition. Therefore, the lower Ti content observed in the EDX spectrum does not indicate a low TiO_2 loading in the composite but rather demonstrates that TiO_2 particles are distributed within and on the activated carbon matrix, while the analyzed surface area remains dominated by carbon.(Gavenda, 2022).

4.5.3 Band Gap Energy Determination of TiO_2- Activated Carbon Using UV-Vis Diffuse Reflectance Spectroscopy (UV-DRS)

Characterization of TiO_2-AC using UV-Vis DRS was performed to evaluate the optical properties of the composite. In particular, the photocatalyst's ability to absorb light and determine the bandgap energy plays a crucial role in photocatalytic systems. These optical properties play a vital role in the photocatalysis process because only photons with energy equal to or greater than the bandgap can excite electrons from the valence band to the conduction band, thereby generating electron-hole pairs (e^--h^+) that subsequently participate in the degradation reaction of dyes (Zaaboul et al., 2024).

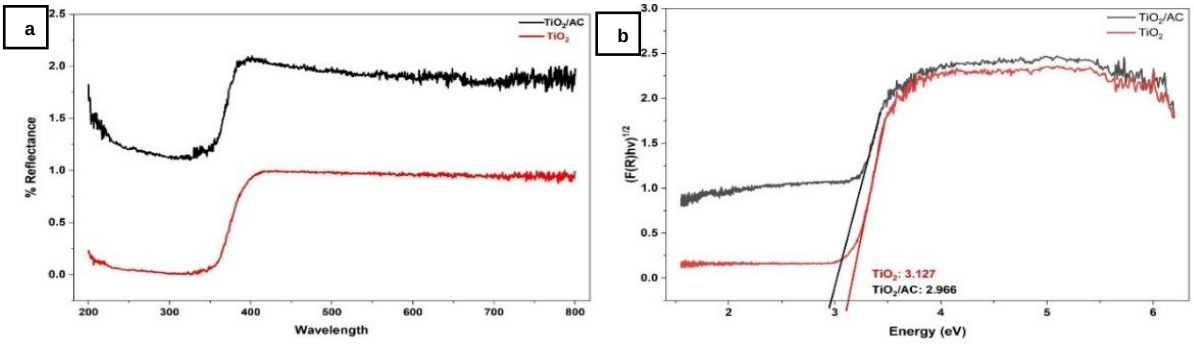

Figure 4. 5 UV–Vis DRS analysis of TiO_2 and TiO_2-Activated Carbon: (a) Reflectance spectra as a function of wavelength, (b) Kubelka–Munk plot for band gap determination.

Figure 4.5 illustrates the optical properties of TiO_2. The graph on the right shows the relationship between % reflectance and wavelength, indicating that TiO_2 and TiO_2-AC materials exhibit different light absorption characteristics in the 200−800 nm range. Pure anatase TiO_2 exhibits low reflectance absorption at wavelengths below 400 nm, then begins to rise sharply at 326.99 nm. This indicates that the optimal absorption edge for electron excitation in TiO_2 lies below 326.99 nm, with decreasing effectiveness at longer wavelengths. In TiO_2-AC, the absorption edge shifts slightly to 325.340 nm. This shift is not very significant and remains within the same range as that of anatase TiO_2. Both TiO_2 and TiO_2-AC exhibit the same absorption range, namely 200–400 nm, indicating that electron excitation occurs within the UV spectrum. Thus, the TiO_2-AC photocatalyst will be active under UV irradiation.

The band gap energy was determined using the Kubelka-Munk equation, which relates the reflectance function to the photon energy. By plotting the Tauc and Kubelka-Munk equations to determine the band gap values, a band gap curve was obtained as shown in Figure 4.4 b. The figure shows a decrease in the band gap of TiO_2 before and after it was supported by activated carbon. TiO_2 before synthesis has a band gap of 3.217 eV, whereas TiO_2 supported by activated carbon has a band gap of 2.966 eV. This decrease in the band gap indicates that the energy required to excite electrons from the valence band to the conduction band is lower, so TiO_2-AC has a better ability to absorb light in the lower energy region and requires less energy to generate electron-hole pairs. The reduction in band gap may be attributed to the interaction between TiO_2 and activated carbon, which can modify the electronic structure of the composite and facilitate charge transfer at the interface. As a result, the TiO_2-AC composite is expected to exhibit enhanced photocatalytic activity due to improved light absorption and more efficient generation of reactive species during the photocatalytic process.

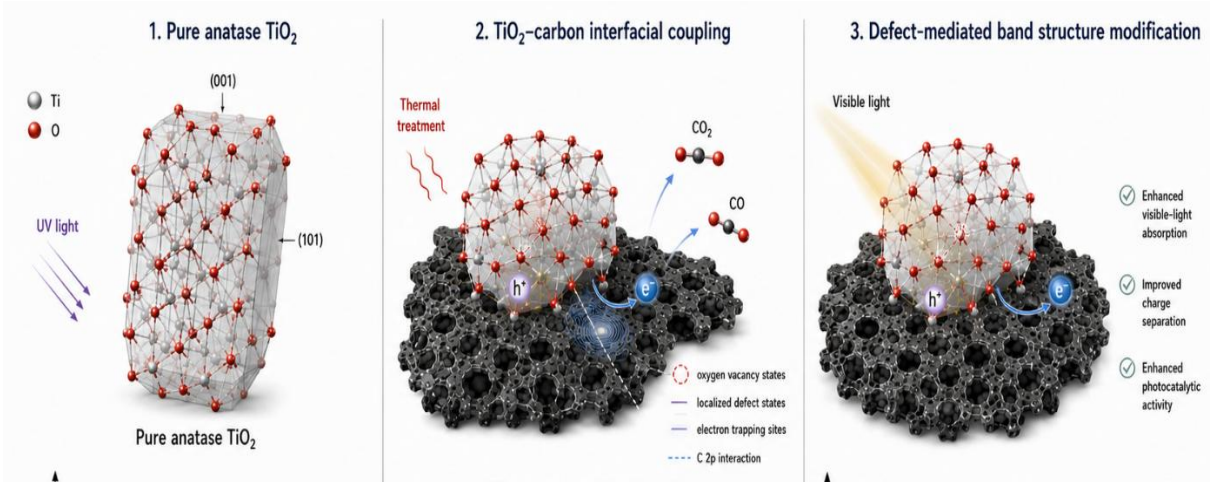

Figure 4. 6 Schematic illustration of oxygen vacancy formation and Ti–O–C interfacial interaction in TiO_2-AC composite

Figure 4.6 illustrates the reduction in the TiO_2-AC band gap before and after synthesis, which can occur due to the formation of oxygen vacancies during the heating process, where TiO_2 reacts with the activated carbon surface. When heated, the Ti-O bonds weaken and break (Guan et al., 2023). Under these conditions, some oxygen atoms in the TiO_2 structure can be released and react with carbon to form CO or CO_2, creating crystal defects in the form of oxygen vacancies in the crystal lattice. The presence of these oxygen vacancies can create new energy levels within the band gap, thereby reducing the energy required to excite electrons from the valence band to the conduction band. Additionally, the interaction between TiO_2 and activated carbon enables the formation of Ti–O–C bonds and surface interactions, which can also influence changes in the energy band structure (Zheng et al., 2022). This enhances visible-light absorption by lowering the excitation energy required for the electron transition. Furthermore, incorporating activated carbon can improve the dispersion of TiO_2 particles on the composite surface, thereby promoting more uniform light exposure. The porous structure of activated carbon may also enhance light harvesting by providing a larger interfacial area between the photocatalyst and the surrounding medium. These characteristics are commonly reported as beneficial factors in TiO_2-based composite photocatalysts.

4.5 Analysis of TiO_2-Activated Carbon Functional Groups Using Attenuated Total Reflectance–Fourier Transform Infrared (ATR-FTIR)

The analysis of composites using ATR-FTIR is intended to identify and evaluate the functional groups present in activated carbon, TiO_2, and TiO_2-AC. Additionally, the ATR-FTIR instrument is used to investigate the stretching-bending interactions at the surface of each sample. This analysis is important for understanding the interactions and changes in functional groups on the composite surface following impregnation synthesis.

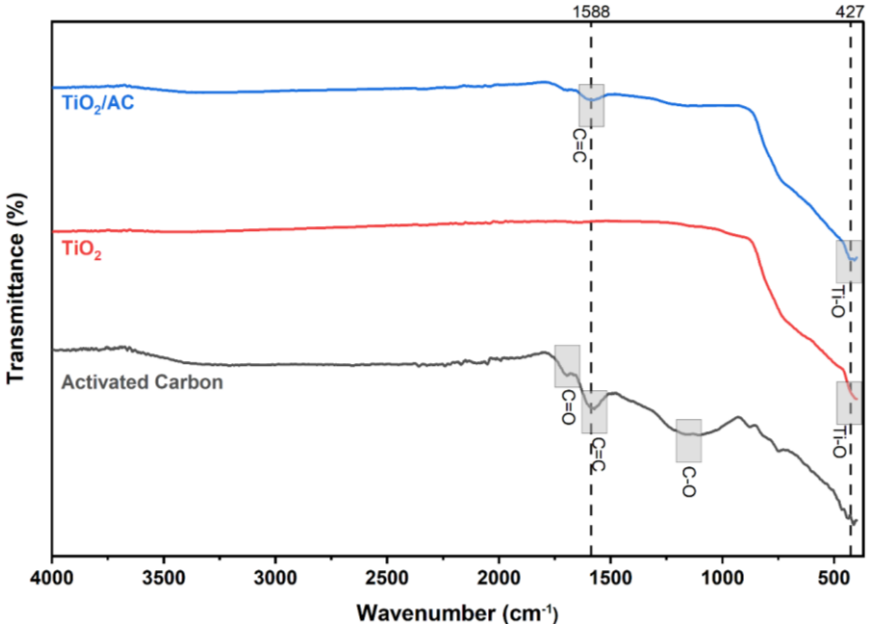

Figure 4. 7 ATR-FTIR spectra of activated carbon, TiO_2, and TiO_2-activated carbon composite.

Figure 4.7 shows a comparison of the absorption spectra of activated carbon, TiO_2, and TiO_2-AC. In these spectra, the activated carbon absorption shows several peaks at 3163, 1697, 1577, and 1155. Meanwhile, in TiO_2, absorption was detected only at 425, whereas in TiO_2-AC, two absorption peaks were observed at 1588 and 420. The FTIR analysis results indicate that several absorption peaks persist in the TiO_2-AC composite after synthesis, namely the C=C absorption band around 3337 cm^{-1} and the Ti-O fingerprint band around 400 cm^{-1}.

The FTIR spectrum of the TiO_2-AC composite does not show all the characteristic absorption bands of activated carbon and TiO_2 with the same intensity, even though the initial composition ratio was 1:1. This may occur because FTIR analysis reflects the vibrational behavior and chemical environment around functional groups, rather than the actual mass composition of the material. TiO_2 remains highly intense after composite formation, indicating that Ti–O vibrations still dominate in the TiO_2-AC system (Shaban et al., 2018). Metal oxide modification can cause shifts and changes in FTIR peak intensity due to interactions at the material interface (Lestari et al., 2026). A'srai et al. (2023) also explain that the decrease in peak intensity in composite photocatalysts can be attributed to chemical interactions occurring during nanocomposite synthesis. Therefore, the weakening or disappearance of some activated carbon absorption bands in this study suggest related to thermal treatment and interfacial interactions between TiO_2 and activated carbon during the composite formation process.

Table 4. 5 ATR-FTIR band assignments of activated carbon, TiO_2, and TiO_2-activated carbon.

Sample	Wavenumber (cm^{-1})	Functional Group	Vibration Type
Activated Carbon (KA)	3163	O–H	Stretching
	1697	C=O	Stretching
	1577	C=C (aromatic)	Stretching
	1155	C–O	Stretching
	875	C–H (aromatic)	Bending
	745	C–H (aromatic)	Bending
TiO_2	3337	O–H	Stretching
	420	Ti-O	Stretching
TiO_2-KA Composite	1588	C=C (aromatic)	Stretching
	427	Ti–O	Stretching

Table 4.5 compares functional groups and their interactions in activated carbon, TiO_2, and TiO_2-AC. In activated carbon, numerous distinct absorption peaks are observed, primarily those indicating interactions between carbon, oxygen, and hydrogen. The 3163 cm^{-1} absorption peak in activated carbon represents the stretching interaction of the O-H group on the activated carbon surface the 1697 cm^{-1} peak indicates C=O stretching, while the 1577 cm^{-1} peak reflects C=C stretching in aromatic groups, and the 1157 cm^{-1} peak corresponds to C-O stretching. Additionally, several carbon-hydrogen interactions were detected at the 875 and 745 cm^{-1} absorption peaks, which correspond to the C–H bending region. The FTIR data show C–O and O–H absorption bands in the activated carbon material, indicating that it can adsorb polar compounds such as RBBR in water (Mendame et al., 2021).

The presence of oxygen-containing functional groups on the activated carbon surface is important because these groups contribute to the surface chemistry and adsorption properties of the material. Hydroxyl, carbonyl, and ether groups can act as active sites for interactions with pollutant molecules through hydrogen bonding, electrostatic attraction, or other surface interactions. Furthermore, these functional groups may facilitate the anchoring of TiO_2 particles during composite synthesis, promoting better contact between activated carbon and TiO_2. Such interactions are advantageous for photocatalytic applications, as they can enhance pollutant adsorption and improve the accessibility of contaminants to the photocatalytically active sites.

FTIR analysis revealed the presence of aromatic C=C vibrations, indicating that activated carbon forms aromatic and graphite-like carbon structures during the carbonization and activation processes. The decrease in FTIR absorption peaks following carbonization indicates the formation of aromatic compounds in activated carbon (Handika et al., 2018)). Aromatic C=C vibrations are also associated with a basic graphite structure consisting of a conjugated hexagonal carbon layer (Elina et al., 2023). Therefore, the activated carbon produced in this study has an amorphous carbon structure containing aromatic carbon domains. Additionally, O–H and C–O functional groups can result in a more polar carbon

surface (Wibowo et al., 2011). Surface groups containing oxygen also contribute to adsorption through hydrogen bonding and electrostatic interactions with organic molecules (Muhsinun & Hidayat, 2025). Therefore, the O–H and C–O functional groups on the activated carbon surface help adsorb RBBR molecules through surface interactions in aqueous solution.

The FTIR spectrum of TiO_2 shows a dominant absorption peak at 3337 cm^{-1}, which corresponds to the O–H group stretching vibration on the TiO_2 surface. This absorption may occur because TiO_2 has hydrophilic and hygroscopic properties, allowing it to absorb water vapor or alcohol from the surrounding environment onto its surface (Parvathiraja et al., 2022). Besides, TiO_2 is known to have a high affinity for water molecules due to its high surface energy, which facilitates interactions between TiO_2 and water vapor, whether in its pure form or as a composite (Bermeo et al., 2020). Consequently, hydroxyl groups can form on the TiO_2 surface and appear as O–H stretching vibrations in the FTIR spectrum. Furthermore, the Ti–O fingerprint region is typically observed in the 400–800 cm^{-1} absorption range. In this study, a weak absorption peak was detected around 420 cm^{-1}. cm^{-1}, which is associated with the Ti–O stretching vibration. However, the peak intensity is relatively weak and difficult to detect clearly by FTIR. This may be related to the limitations of ATR-FTIR in detecting vibrations of metal oxide semiconductors such as TiO_2, as this material has low infrared absorption characteristics and lacks strong covalent bonds that interact effectively with infrared radiation. ATR-FTIR also has limitations in analyzing absorption bands near the lower detection range around 400 cm^{-1} (Komalasari & Sunendar, 2013).

The FTIR results for the synthesized TiO_2-AC composite in this study show two distinct, sharp absorption peaks. The ATR-FTIR spectrum reveals a combination of the C=C absorption from activated carbon at 1588 cm^{-1} and the fingerprint absorption from the stretching interaction of the Ti–O bond at the 427 cm^{-1} absorption band, which also serves as the fingerprint of TiO_2. These results indicate that the synthesis of the TiO_2-AC composite was successful because the TiO_2-AC spectrum retains the C=C absorption of the activated carbon while still exhibiting the fingerprint absorption of TiO_2 in the 400–500 cm^{-1} region, which corresponds to the oxygen-metal-oxygen bond (Parvathiraja et al., 2022). The simultaneous presence of these characteristic absorptions confirms that both TiO_2 and activated carbon coexist within the synthesized material. Furthermore, the preservation of the characteristic bands of each component suggests that the interaction between TiO_2 and activated carbon is primarily physical in nature, allowing both materials to maintain their fundamental structural features after the synthesis process. In addition, no significant shift in the major absorption bands was observed after composite formation, indicating that the crystal structure of TiO_2 and the carbon framework remained relatively stable during the synthesis process. .

4.6 Photocatalytic Degradation Performance of Remazol Brilliant Blue R (RBBR) using UV-Vis Spectrophotometry

4.6.1 Determination of Wavelength and The RBBR Standard Curve

The wavelength was determined by m

easuring the maximum wavelength of a 10 ppm RBBR solution, which was then analyzed using a UV-Vis spectrophotometer to identify the maximum wavelength of RBBR. Following the analysis, the wavelength of RBBR was found to be 591 nm.

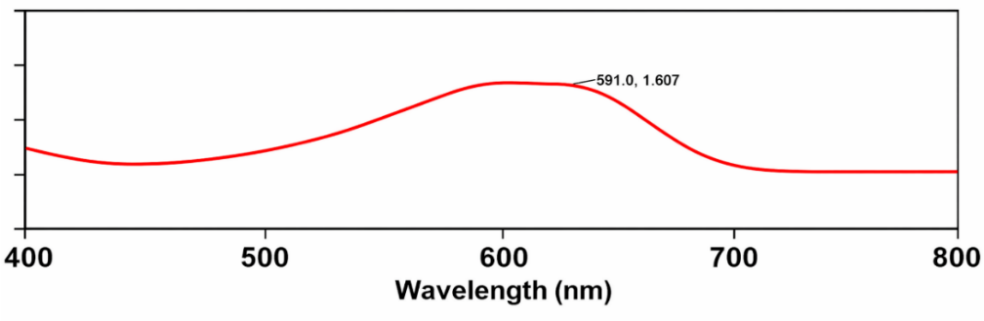

Figure 4. 8 Waveleght of RBBR

Figure 4.8 shows that the maximum wavelength of RBBR is 591 nm. This is consistent with the theory that the wavelength of RBBR lies between 590 and 595 nm (Mattle & Thampi, 2013). Next, a standard curve was prepared for RBBR to determine the R value in the RBBR sample. The standard curve was prepared by measuring RBBR at concentrations of 20, 40, 60, 80, 100, and 120 ppm.

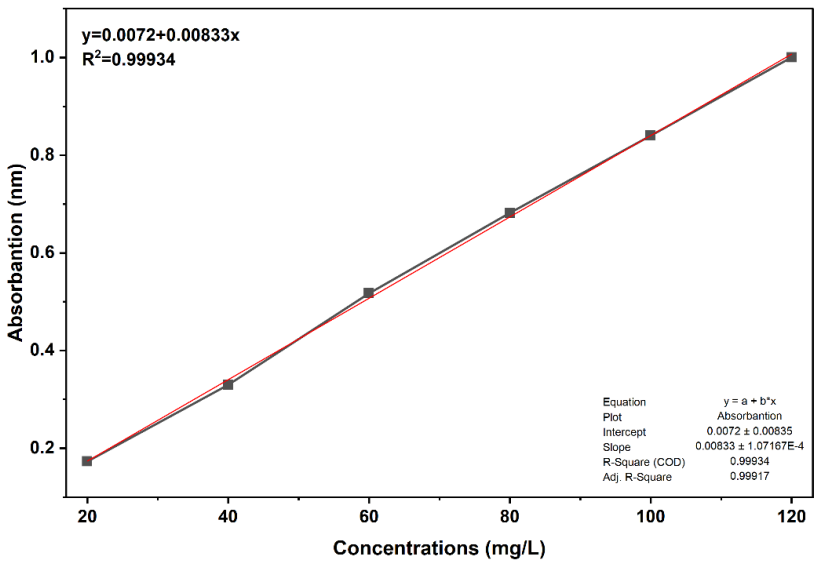

Figure 4. 9 The RBBR Standard Curve

Figure 4.9 shows the standard curve for RBBR, with an excellent R value of 0.999. The closer the R value is to 1, the more valid the data.

4.6.2 Remediation Test of Remazol Brilliant Blue R with Variations in TiO_2-Palm Shell Activated Carbon Mass

The performance of TiO_2-AC photocatalysts for wastewater remediation involves more than just photocatalytic activity. A 50:50 mixture of TiO_2 and activated carbon derived from coconut shells provides adsorption capacity within the TiO_2-AC photocatalytic system. In this study, the reduction in RBBR concentration was attributed to adsorption and photocatalytic degradation mechanisms under dark and UV-irradiated conditions. Under dark conditions, TiO_2 is not activated due to the absence of photon energy. Therefore, the reduction in RBBR concentration is attributed to adsorption on the activated carbon and the catalyst surface. Meanwhile, under UV irradiation, the decrease in dye concentration is attributed to the combined effects of adsorption and photocatalytic degradation on the catalyst surface. Thus, the contribution of degradation is determined by the difference between total remediation under UV irradiation and adsorption under dark conditions. Therefore, remediation efficiency represents the total removal of the dye, comprising both adsorption and photocatalytic degradation mechanisms. Additionally, the photocatalyst mass ratio is used to assess the increase in active sites and to optimize photocatalytic performance. The optimum photocatalyst dose was determined by varying the catalyst mass to 10, 20, 30, 40, and 50 mg in 25 mL of RBBR solution.

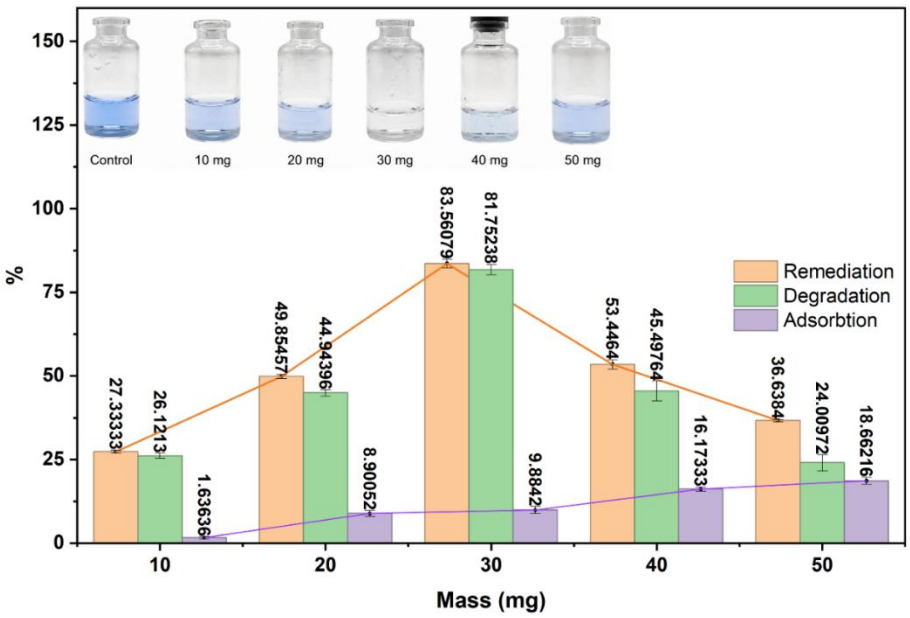

Figure 4. 10 The effect of variations in the mass of TiO_2-activated carbon photocatalyst on the adsorption efficiency, photodegradation, and visual changes of Remazol Brilliant Blue R solution.

Figure 4.10 illustrates the different adsorption and photodegradation mechanisms in the TiO_2-AC system, indicating that catalyst loading significantly influences the dominant degradation pathway. The improvement in adsorption performance at higher TiO_2-AC mass ratios is primarily due to the increased availability of active adsorption sites on the activated

carbon. The porous structure of activated carbon promotes the accumulation of RBBR molecules near the photocatalytic surface, thereby enhancing the interaction between the dye molecules and the active sites of TiO_2. This behavior indicates that activated carbon functions not only as an adsorbent but also as a support material that facilitates the transfer of pollutants to the photocatalytic center. Similar findings were reported by Foroutan et al. (2021), in which an increased adsorbent dose enhanced dye absorption due to a larger surface area and a greater number of active binding sites. On the other hand, the photodegradation mechanism indicates an optimal catalyst loading of 30 mg. At lower catalyst dosages, an increase in the TiO_2-AC mass enhances photon absorption and promotes the formation of electron-hole pairs and reactive oxidative species under UV irradiation. Furthermore, the synergistic interaction between adsorption and photocatalysis contributes to more efficient degradation because the adsorbed dye molecules are positioned closer to the reactive sites of TiO_2 (Alghamdi et al., 2022).

However, catalyst overloading reduces photocatalytic efficiency due to particle agglomeration and limited light penetration in the suspension. At higher catalyst concentrations, TiO_2-AC particles tend to overlap and shield one another, thereby reducing the amount of UV light reaching the active sites. This shielding effect inhibits the formation of electron-hole pairs and reduces the generation of reactive oxidative species responsible for dye degradation. Furthermore, overloading catalyst concentration increases turbidity and promotes light scattering, causing a portion of the incident UV irradiation to be reflected rather than absorbed by the photocatalyst surface (Safni et al., 2024). Consequently, photocatalytic activity decreases at catalyst doses above the optimal conditions.

The combined adsorption and photodegradation mechanism of the TiO_2-AC photocatalyst demonstrates effective remediation performance for RBBR wastewater. Under optimal conditions of 30 mg of catalyst in 25 mL of solution (1.2 g-L), the system achieves the highest overall remediation efficiency, indicating a balanced contribution between adsorption capacity and photocatalytic activity.

4.6.3 Evaluation of Remazol Brilliant Blue R Degradation Efficiency at Varying RBBR Concentrations and Optimal TiO_2-Activated Carbon Mass

A variation test of the initial concentration of RBBR dye was conducted to evaluate the degradation performance of the TiO_2-AC photocatalyst at progressively increasing dye concentrations and to determine the optimum concentration for the degradation system. In this study, the decrease in RBBR concentration was evaluated under dark and UV irradiated conditions. Under dark conditions, the reduction in concentration suggested a contribution from adsorption, whereas under UV irradiation, the decrease indicated the combined effects of adsorption and photocatalytic degradation. Therefore, remediation efficiency represents the total dye removal, whereas the degradation contribution was determined from the difference

between total remediation and adsorption. The evaluation was performed using the optimum TiO_2-AC mass of 30 mg with initial RBBR concentrations of 10, 20, 30, 40, and 50 ppm.

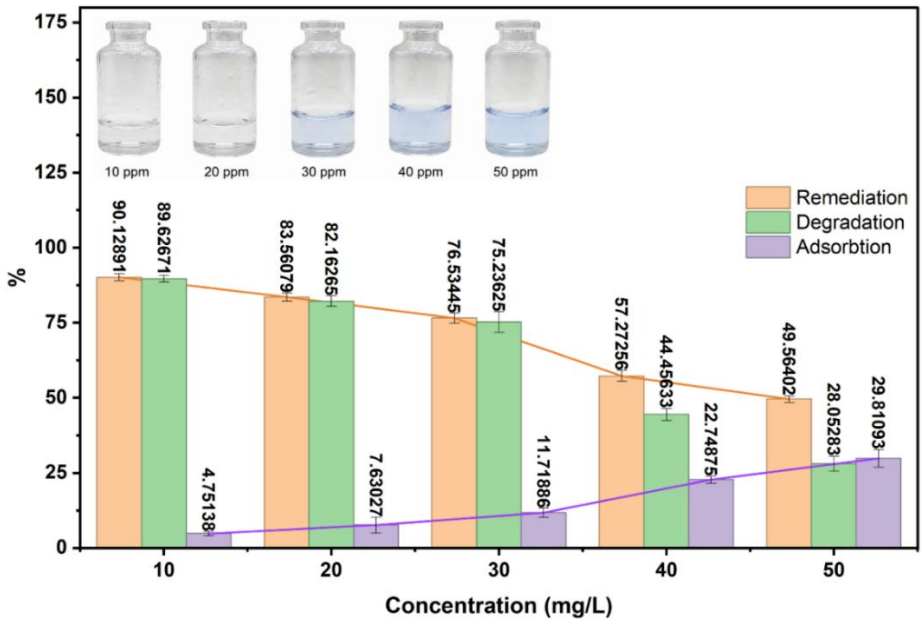

Figure 4.11 The Effect of Initial Remazol Brilliant Blue R Concentration on Adsorption Efficiency, Photodegradation, and Remediation Using TiO_2-Activated Carbon Photocatalysts.

Figure 4.11 illustrates contrasting behavior between the adsorption and photodegradation mechanisms as the initial RBBR concentration increases. Adsorption performance increases with increasing dye concentration, indicating that a higher concentration gradient enhances mass transfer from the solution to the activated carbon surface. This condition increases the probability of interaction between RBBR molecules and available adsorption sites on the porous TiO_2-AC structure. Similar behavior has been reported in activated carbon adsorption systems, where higher adsorbate concentrations provide a stronger driving force for adsorption until the surface is saturated (Rápó & Tonk, 2021).

In contrast, photocatalytic degradation efficiency decreases significantly with increasing initial dye concentration, dropping from approximately 90% at 10 ppm to below 50% at 50 ppm. This behavior indicates that excessive dye concentration limits UV penetration into the solution, as suggested by the increasingly intense color of the RBBR solution. The resulting decrease in the number of photons reaching the TiO_2 surface reduces photoactivation and inhibits the formation of electron-hole pairs (e^--h^+) capable of generating reactive oxidative species. Additionally, the accumulation of dye molecules on the catalyst surface can block active sites on TiO_2-AC and reduce photocatalytic performance. This phenomenon is generally referred to as the shielding effect, in which high concentrations of the dye solution absorb or scatter incoming UV light before it reaches the catalyst surface (Bekele & Alamnie, 2025).

4.7 Comparison of RBBR Removal Efficiency Using TiO_2, Activated Carbon, and TiO_2-Activated Carbon at Optimum Conditions under Light and Dark Conditions

A comparison of dye degradation by RBBR, TiO_2, activated carbon, and TiO_2-AC was conducted to evaluate the performance and effectiveness of each system under dark and UV conditions. This treatment was performed to distinguish the contributions of adsorption and photodegradation mechanisms in the removal of Remazol Brilliant Blue R dye. For the TiO_2-AC composite, the evaluation was conducted under optimal conditions obtained from previous experiments, namely a catalyst mass of 30 mg and an initial RBBR concentration of 10 ppm. In this study, adsorption efficiency refers to the decrease in RBBR concentration under dark conditions (non-irradiation), whereas remediation efficiency represents the total removal of the dye under UV irradiation, including contributions from adsorption and photocatalytic degradation. Meanwhile, degradation efficiency represents the photocatalytic process's contribution under UV light. All efficiencies were calculated separately from triplicate experimental data for each treatment condition.

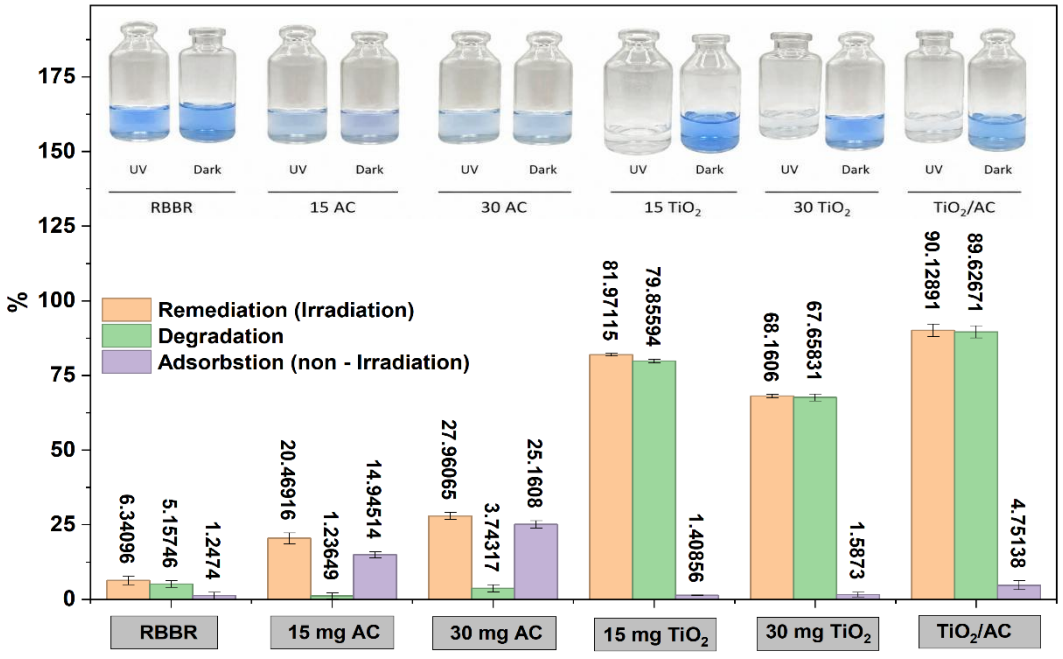

Figure 4. 12 Comparison of RBBR Degradation Effectiveness by Various Systems

Figure 4.12 illustrates a significant difference among the four samples under both irradiated and non-irradiated conditions. The TiO_2-AC composite exhibits superior effectiveness compared to the other samples. The enhanced performance of TiO_2-AC is attributed to the synergistic interaction between adsorption and photocatalytic degradation, whereby the porous active sites of activated carbon facilitate the accumulation of RBBR molecules around TiO_2 active sites, thereby improving photocatalytic efficiency (Alghamdi et al., 2022). In addition to the role of activated carbon, the relatively high SiO_2 content detected after activation also indirectly suggests an effect on the remediation performance of the TiO_2-

AC composite. Silica containing materials are known to influence the textural properties and surface characteristics of supported TiO_2 photocatalysts, potentially enhancing particle dispersion and pollutant interactions on the catalyst surface (López-Muñoz et al., 2005). However, despite its possible contribution to surface and adsorption properties, SiO_2 is not considered the primary active phase in the photocatalytic process due to its low concentration in TiO_2-AC, as indicated by the XRF analysis results in Table 4.3, since the degradation mechanism is predominantly governed by TiO_2 through electron–hole generation and reactive oxidative species formation. Although TiO_2-AC contains adsorption active sites from activated carbon, its adsorption capacity remained lower than that of pure activated carbon due to partial pore blockage by TiO_2 particles, thereby reducing its adsorption effectiveness (Ghamarpoor et al., 2024).

In addition, analyses of adsorption and degradation capacities are necessary to determine the effectiveness and dominant mechanisms of RBBR remediation using the TiO_2-AC catalyst. The adsorption capacity of the TiO_2-AC composite catalyst is relatively low, at approximately 0.430 mg-g, indicating that adsorption's contribution to dye removal is not particularly significant. This is consistent with the partial blocking of the pores of activated carbon by TiO_2 particles, which reduces the number of available adsorption sites. Nevertheless, a low adsorption capacity does not necessarily indicate suboptimal system performance; in this system, adsorption primarily serves as an initial step, facilitating the accumulation of RBBR molecules around the photocatalyst’s active sites.

Another aspect observed in Figure 4.12 is the comparison between the TiO_2-AC composite and pure TiO_2 at proportional catalyst masses. Since the TiO_2-AC composite was synthesized using a 1:1 mass ratio, the optimum dosage of 30 mg TiO_2-AC theoretically contains approximately 15 mg TiO_2 and 15 mg activated carbon. Therefore, comparison with 15 mg pure TiO_2 is necessary to evaluate whether the enhanced remediation performance was solely related to TiO_2 content or influenced by composite interactions. The TiO_2-AC composite exhibited higher remediation efficiency than 15 mg pure TiO_2, although containing a comparable TiO_2 fraction, indicating that activated carbon contributed not only as a support material but also as a component that enhanced photocatalytic performance.

This increase in activity indicates that the addition of activated carbon has enhanced TiO_2 efficiency in the composite system. A similar behavior was reported by Mondol et al. (2021), where AC-TiO_2 nanohybrids exhibited higher photocatalytic performance compared to pure TiO_2 due to synergistic interactions between adsorption and photocatalysis. Furthermore, Yue et al. (2024) reported that activated carbon can increase the local concentration of dye molecules around the TiO_2 surface, thereby promoting more effective photocatalytic degradation. These findings suggest that the superior performance of TiO_2-AC is not only due to the amount of catalyst but also to the enhanced interfacial interactions provided by the composite structure.

On the other hand, the degradation capacity (*q* deg) is much higher, at approximately 7.730 mg-g, indicating that the photocatalytic process is the primary mechanism for dye removal. Under irradiation conditions, TiO_2 is capable of generating electron hole pairs (e^--h^+), which subsequently form reactive species such as hydroxyl radicals (•OH) that play a role in degrading dye molecules. Overall, the remediation capacity of TiO_2-AC is approximately 8.160, based on the combined adsorption and degradation capabilities. A significant difference between the *q* (ads) and *q* (deg) values confirms that the process occurring is not merely adsorption but is dominated by degradation reactions that proceed continuously on the photocatalyst surface (Alghamdi et al., 2022).

4.8 Reusability Performance of TiO_2 and TiO_2-AC Photocatalyst

The reusability of TiO_2-AC and TiO_2 photocatalysts was evaluated under optimal operating conditions to assess their stability during repeated use. Reusability testing was conducted to determine the practical applications and operational sustainability of photocatalytic materials for wastewater treatment. After each cycle, the photocatalysts were separated, washed, dried, and reused for the subsequent remediation process. The remediation efficiency achieved in each reuse cycle is shown in Figure 4.13.

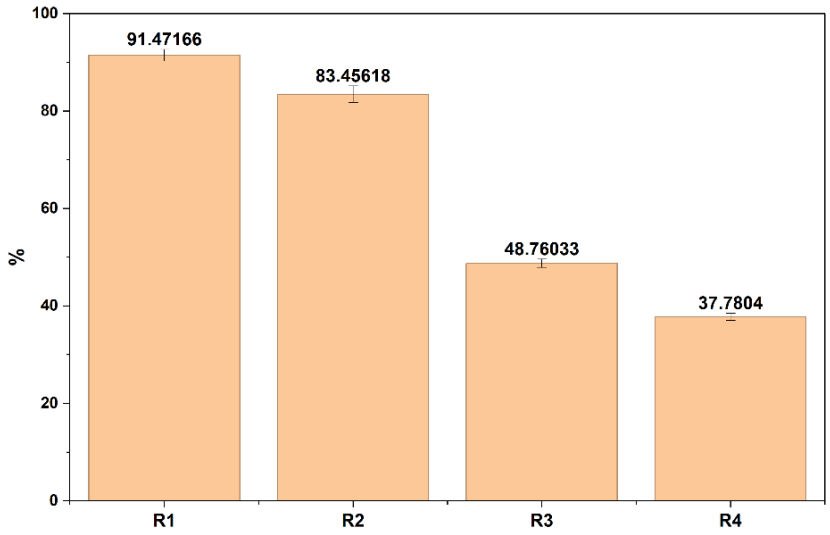

Figure 4.13 Reusability Performance of TiO_2-AC Photocatalyst

Figure 4.13 illustrates that the TiO_2-AC photocatalyst exhibits a decline in remediation efficiency during successive reuse cycles, indicating a partial loss of photocatalytic activity after prolonged operation. The decline in performance becomes more significant after the second cycle, indicating that progressive catalyst deactivation affects the remediation process during consecutive reuse. However, the photocatalyst still retains measurable remediation capacity after the fourth cycle, indicating that the TiO_2-AC composite remains partially active under repeated operational conditions.

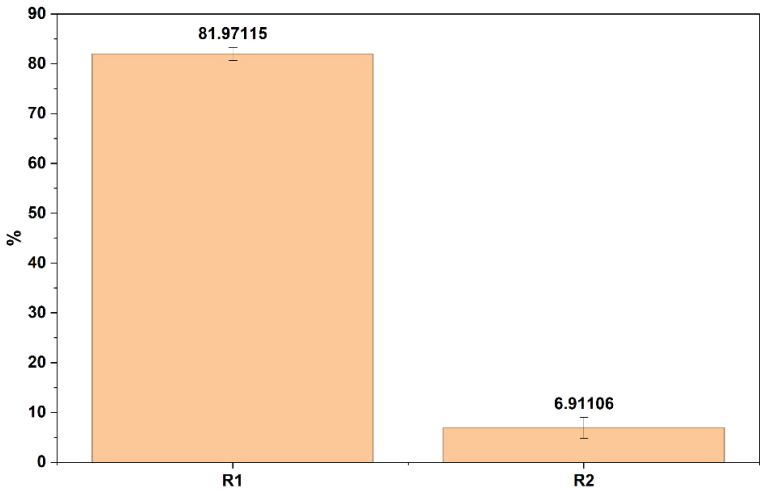

Figure 4.14 Reusability Performance of TiO_2 Photocatalyst

Figure 4.14 illustrates a significant decrease in the photocatalytic activity of pure TiO_2 after the first reuse cycle. This decrease is suggested to be related to the loss of a significant portion of the photocatalyst during the recovery process. Due to their fine particle size and high dispersibility in aqueous media, some TiO_2 particles were likely lost during the separation and washing steps, despite repeated centrifugation to recover the catalyst from the RBBR solution. The resulting reduction in catalyst mass decreased the number of active sites available for photocatalytic reactions, leading to a drastic drop in degradation efficiency during the second cycle. A similar phenomenon was reported by Mukonza et al. (2022), who observed that the degradation efficiency of pure TiO_2 decreased from 64.6% in the first cycle to 31.2%, which they attributed to a 39.2% loss of photocatalyst mass during recovery. They stated that pure TiO_2 exhibits low recovery capability due to its high dispersibility in aqueous solutions. This observation is also supported by Usman et al. (2026), who reported that the large-scale application of conventional TiO_2 nanoparticles is often hindered by poor and limited recovery capability. Aggregation, surface contamination, dissolution of active species, and structural degradation during repeated use can contribute to the progressive loss of photocatalytic performance. Due to the severe decline in activity observed during the second cycle and the insufficient amount of recovered catalyst for further applications, the reusability test of pure TiO_2 was terminated after the second cycle.

Based on Figure 4.13 and Figure 4.14, it can be seen that the reusability performance of TiO_2-AC is far superior to that of pure TiO_2. Based on the results obtained, TiO_2-AC retained approximately 83.4% of its initial activity after the second cycle, whereas pure TiO_2 retained only about 6.9% of its initial efficiency after reuse. Even after four cycles, the TiO_2-AC composite retained approximately 37.7% of its original activity, demonstrating significantly greater durability than pure TiO_2. The smaller loss of activity observed in TiO_2-AC indicates that incorporating activated carbon significantly helps maintain photocatalytic function during

repeated use. Similar improvements in stability for TiO_2-carbon-based composites have been reported in previous studies, where carbon supports were found to enhance the catalyst's resistance to deactivation and photocorrosion during cyclic operation

The decrease in remediation efficiency following repeated use indicates the gradual deactivation of the photocatalyst during prolonged operation. The observed decrease in activity suggest be related to the accumulation of degradation intermediates on the catalyst surface, which can block active sites and reduce photocatalytic activity. Additionally, repeated recovery and washing processes may lead to partial catalyst loss and particle agglomeration, thereby reducing the effective surface area exposed to UV radiation. A similar decline in recycling performance has been reported for TiO_2 based composite photocatalysts due to catalyst fouling, surface deactivation, and reduced light accessibility after repeated usage cycles. Farghaly et al. (2024) also reported that repeated photocatalytic cycles can reduce degradation efficiency due to the gradual deactivation of TiO_2 active sites and limited regeneration.

Another factor contributing to the TiO_2-AC composite's superior reusability is the role of activated carbon as a support. The presence of activated carbon helps disperse TiO_2 particles more effectively, thereby reducing particle agglomeration and minimizing catalyst loss during the separation process following the reaction. Compared to pure TiO_2 nanoparticles, which are extremely small and difficult to separate from solution, as shown by the XRD results in Table 4.2, the TiO_2 -AC composite has a larger particle size, making it easier to recover via standard filtration or sedimentation. This separation offers a significant advantage in wastewater treatment by reducing material loss, simplifying operational processes, and lowering treatment costs. Furthermore, the use of activated carbon derived from oil palm shells offers economic value and environmental benefits by utilizing biomass waste as the raw material.

4.9 Islamic Value Foundations in the Development of Environmental Technology

The development of TiO_2-activated carbon photocatalyst technology for wastewater remediation is a significant step toward protecting the environment, particularly aquatic ecosystems such as rivers, lakes, and oceans. Persistent dye wastes like RBBR, which are resistant to natural degradation, pose a substantial threat by contaminating water bodies and disrupting aquatic ecosystems, thereby endangering nearby plants, animals, and human populations. Within Islamic teachings, causing environmental harm is explicitly prohibited, as articulated in Surah al Qaṣaṣ [28]:77.

وَابْتَغِ فِيْمَآ اٰتٰىكَ اللّٰهُ الدَّارَ الْاٰخِرَةَ وَلَا تَنْسَ نَصِيْبَكَ مِنَ الدُّنْيَا وَاَحْسِنْ كَمَآ اَحْسَنَ اللّٰهُ اِلَيْكَ وَلَا تَبْغِ الْفَسَادَ فِى الْاَرْضِ ۗاِنَّ

اللّٰهَ لَا يُحِبُّ الْمُفْسِدِيْنَ

Meaning: *"And seek, through what Allah has given you, the home of the Hereafter; but do not forget your share of the world. And do good as Allah has done good to you, and do not cause corruption on the earth. Indeed, Allah does not like those who cause corruption."*

According to Tafsir Ibnu Katsir, this verse underscores the prohibition against causing harm on earth, encompassing both social and environmental destruction. Ibnu Katsir interprets 'damage' as actions that harm others, including injustice, oppression, and environmental degradation (Ramadhan, 2019). The consequences of dye waste pollution extend beyond water quality deterioration, threatening the sustainability of organisms within the ecosystem. Consistent with this perspective, Surah al Baqarah [2]:205 further addresses this issue:

وَاِذَا تَوَلّٰى سَعٰى فِى الْاَرْضِ لِيُفْسِدَ فِيْهَا وَيُهْلِكَ الْحَرْثَ وَالنَّسْلَ ۗوَ اللّٰهُ لَا يُحِبُّ الْفَسَادَ

Meaning*: "When he turns away, he strives throughout the land to cause corruption therein and destroy crops and livestock. Allah does not like corruption."*

Ibnu Katsir explains in his book Tafsir Ibnu Katsir, volume 2, that corruption on earth is a result of human actions themselves (in Hatami, 2025). The hypocrites in this verse are those who continuously commit destructive acts on earth and deliberately destroy crops. This includes fields, fruits, and livestock, which are essential for human life.

The phrase (وَ اللّٰهُ لَا يُحِبُّ الْفَسَادَ) means that Allah does not like those who cause destruction, especially those who impact society. Based on its impact, it is clear that people who intentionally dispose of waste without proper treatment, such as dye waste that can pollute aquatic ecosystems and kill aquatic organisms, fall into the category of those who cause destruction. In addition to the Qur'an, the principle of maintaining water quality is also emphasised in the hadith of the Prophet Muhammad. Hadith Shahih Muslim No. 282 - Kitab Thaharah

وَحَدَّثَنِي زُهَيْرُ بْنُ حَرْبٍ، حَدَّثَنَا جَرِيرٌ، عَنْ هِشَامٍ، عَنِ ابْنِ سِيرِينَ، عَنْ أَبِي هُرَيْرَةَ، عَنِ النَّبِيِّ صلى الله عليه وسلم قَالَ " لاَ يَبُولَنَّ أَحَدُكُمْ فِي الْمَاءِ الدَّائِمِ ثُمَّ يَغْتَسِلُ مِنْهُ".

Meaning: *"Shahih Muslim No. 282: Zuhair bin Harb narrated to me; Jarir informed us, from Hisham, from Ibn Sirin, from Abu Hurairah reported: The Messenger said: 'None of you should urinate in stagnant water and then bathe in it.'"*

Based on the hadith above, it can be understood that the Prophet forbade his people from urinating in still water, including ponds and bathing places. This indicates that humans must maintain the quality and cleanliness of water. For a Muslim, water is not only a necessity for consumption but also a means for purification when performing worship. 'Ma' (ماء) is singular, with plural forms 'amwah' (أمواه) and 'miyah' (مياه), which mean 'water' and 'liquid substances'. In the Qur'an, this word appears only in the singular form and not in its plural forms. It is mentioned 63 times in 41 surahs. If the qiyas paradigm is applied in understanding this verse, it can be concluded that urinating carelessly is prohibited because it can damage or pollute water, therefore by using qiyas awlawi (a ruling in a new case is considered stronger or more deserving to be equated with the original ruling because the 'illat is more evident), water

pollution caused by waste, industrial discharge, marine pollution due to oil spills, and other pollutants that can damage the environment and water quality would certainly have a stronger prohibition (Muchlis, 2019).

This principle serves as the foundation of this study, in which dye waste such as RBBR indicates contamination that must be treated before the water can be reused. This is reinforced by the views of Islamic scholars regarding Islamic eco-theology, in which the environment is considered a vital aspect that must be collectively safeguarded and treated with full responsibility. In a broader context, these values can be understood through an eco-theological approach, a theological framework that integrates the relationship between God, humanity, and nature into a unified whole.

Ecotheology in Islam has emerged as a response to the global environmental crisis, which is viewed not merely as a technical issue but also as a moral and spiritual crisis in humanity's perception of nature (Ruswanda, 2025). From this perspective, humans are not positioned as rulers over nature but rather as stewards entrusted with the responsibility to maintain environmental balance and sustainability. The concept of eco-theology emphasizes that the relationship between humans and nature must be grounded in the value of compassion (rahmah), and rejects the anthropocentric paradigm that tends to be exploitative toward the environment. According to Nasaruddin Umar, the relationship between humans and nature (hablum min al-'alam) is one in which humans, as stewards, have the duty to maintain the balance of this relationship. Nasaruddin Umar also asserts that protecting the environment and preserving nature are part of worship and should be viewed as a divine trust, not merely as social activities (Ruswanda, 2025). Furthermore, in contemporary Islamic eco-theological studies, the 2023 MUI fatwa on eco-theology affirms that environmental stewardship is viewed as part of worship and a manifestation of faith, one that is not merely normative but must be realized through concrete actions, such as the wise management of resources and the adoption of sustainable lifestyles (Iqbal, 2025). Thus, eco-theology functions not only as a theological foundation but also as an ethical and practical framework for promoting solutions to environmental problems.

This view is further strengthened by the opinions of modern scholars regarding pollution and environmental preservation. In the modern context, water pollution does not only come from simple impurities but also from industrial waste, which has more complex and widespread impacts. Therefore, contemporary scholars provide more specific legal rulings on environmental pollution practices. As stated in the MUI fatwa (latest at the 11th National Conference in 2025), disposing of waste, especially plastic and hazardous waste, into rivers, lakes, and seas is haram. This action is considered to damage ecosystems and betray the mandate of stewardship in preserving the earth (Nuh & Husni, 2025).

Based on the explanation above, the development of photocatalytic technology in this study not only has scientific value in reducing water pollution levels but is also in line with the

objectives of Islamic law (*maqāṣid al-syarīʿah*). The treatment of dye waste, such as Remazol Brilliant Blue R (RBBR), contributes to preserving life (*ḥifẓ al-nafs*) because it can prevent diseases and health impacts due to polluted environments. In addition, proper waste management also supports preserving wealth *(ḥifẓ al-māl*) through the conservation of water resources and the prevention of economic losses due to environmental damage. This effort is also related to preserving lineage (*ḥifẓ al-nasl*), namely by ensuring that future generations can still enjoy a clean and liveable environment. Thus, the application of photocatalytic technology is not only a technical solution in environmental chemistry but also a form of implementation of Islamic values in maintaining the sustainability of life (Ramadhan, 2019).

CHAPTER V
CONCLUSIONS AND RECOMMENDATIONS

5.1 Conclusions

Based on the results and discussion of this study, the following conclusions can be drawn as follows:

1. The TiO_2-activated carbon photocatalyst derived from oil palm shells was successfully synthesized and characterized. XRD analysis confirmed the presence of the anatase phase, with a main peak at $2\theta = 25.43°$, and no evidence of rutile or brookite phases. XRF analysis indicated a TiO_2 content of 97.22%, while EDX revealed the presence of C (67.73%), Ti (23.45%), and O (8.81%), confirming the successful formation of the composite. FTIR spectra identified aromatic C=C groups at 1588 cm^{-1} and Ti–O bonds at 427 cm^{-1}, indicating the coexistence of adsorption and photocatalytic functionalities. UV–Vis DRS analysis showed a reduction in band gap energy from 3.19 eV to 2.89 eV, demonstrating enhanced light absorption and electron excitation capability.
2. The optimum mass of the TiO_2-activated carbon photocatalyst was found to be 30 mg in 25 mL of solution, achieving a degradation efficiency of 86.07% and a total remediation efficiency of 87.524%.
3. The optimum initial concentration of RBBR was 10 ppm, which resulted in the highest degradation efficiency of 91.47%.

5.2 Recommendations

Further research is recommended to conduct a more detailed evaluation of the adsorption isotherms and reaction kinetics in the photocatalytic system, as well as to comprehensively compare them with the performance of activated carbon as a single adsorbent. Additionally, the use of more effective synthesis methods, such as sonication, should be considered to improve the dispersion of TiO_2 particles on the surface of activated carbon, thereby ensuring a more uniform distribution of the active phase. Further analysis using instruments such as LC-MS is also necessary to identify degradation products and confirm that the molecular structure of the dye has been broken down into simpler compounds.

Further material development can be achieved through the optimization of the activated carbon activation process using a combination of acid and base activation to improve impurity removal, particularly silica, which is less soluble under acidic conditions. Additionally, modifying the photocatalyst through the use of a bimetallic system is recommended to evaluate the potential for increased photocatalytic activity compared to a monometallic TiO_2 system, thereby yielding a material with more optimal performance.

BIBLIOGRAPHY

Adams, F. (2005). *X-Ray Adsorption And Diffraction*. University Of Antwerp.

Aguilar, P., Bernal-Ramírez, J., Vázquez-Garza, E., Vélez-Escamilla, L. Y., Lozano, O., García-Rivas, G. D. J., & Contreras-Torres, F. F. (2023). Synthesis And Characterization Of Rutile Tio_2 Nanoparticles For The Toxicological Effect On The H9c2 Cell Line From Rats. *Acs Omega*, *8*(21), 19024–19036. Https:--Doi.Org-10.1021-Acsomega.3c01771

Ahmed, S., Shishir, Md. K. H., Islam, Md. T., Rahaman, Md. A., Aman, S., Aidid, A. R., Sadia, S. I., Rana, Md. M., & Alam, Md. A. (2025). Crystallinity Integration Of Anatase (Tio2) Nanocrystal By Whole Powder Pattern Fitting (Wppf) Method: A Rietveld Refinement Study. *Results In Materials*, *26*, 100673. Https:--Doi.Org-10.1016-J.Rinma.2025.100673

Al' Adawiyyah, H. (2022). *Pengaruh Variasi Ph Dan Konsentrasi H2o2 Terhadap Proses Fotodegradasi Zat Warna Metil Jingga Menggunakan Fotokatalis Tio2-Zeolit Alam* [Skripsi].

Alghamdi, Y. G., Krishnakumar, B., Malik, M. A., & Alhayyani, S. (2022). Design And Preparation Of Biomass-Derived Activated Carbon Loaded Tio2 Photocatalyst For Photocatalytic Degradation Of Reactive Red 120 And Ofloxacin. *Polymers*, *14*(5), 880. Https:--Doi.Org-10.3390-Polym14050880

Ali, M., Benzaouak, A., Tangarfa, M., Abrouki, Y., Belekbir, S., Hazzat, M. El., El Hamidi, A., & Abdelouahed, L. (2025). Multi-Response Optimization Of The Adsorption Properties Of Activated Carbon Produced From H2so4 Activated Sludge: Effects Of Washing With Hcl. *Case Studies In Chemical And Environmental Engineering*, *11*, 101219. Https:--Doi.Org-10.1016-J.Cscee.2025.101219

Al-Qaraddawi, Y. (2001). *Islam Agama Ramah Lingkungan*. Pustakaal-Kautsar.

An-Nawawi, I. (2014). *Syarah Shahih Muslim*. Darus Sunnah.

Anucha, C. B., Altin, I., Bacaksiz, E., & Stathopoulos, V. N. (2022). Titanium Dioxide (Tio_2)-Based Photocatalyst Materials Activity Enhancement For Contaminants Of Emerging Concern (Cecs) Degradation: In The Light Of Modification Strategies. *Chemical Engineering Journal Advances*, *10*, 100262. Https:--Doi.Org-10.1016-J.Ceja.2022.100262

A'srai, A. I. M., Amin, K. A. M., & Osman, U. M. (2023). Cuo-Tio2 Nanocomposite Photocatalyst For Efficient Mo Degradation. *Digest Journal Of Nanomaterials And Biostructures*, *18*(3), 1005–1124. Https:--Doi.Org-10.15251-Djnb.2023.183.1105

Asy-Syaukani, I. (2006). *Nailul Authar*. Pustaka Azzam.

Babatunde, E. O., Enomah, S., Akwenuke, O. M., Ibeh, M. A., Okwelum, C. O., Mundu, M. M., Adepoju, P. O., Aki, A. O., Oghenejabor, O. D., Adepoju, T. F., Ifedora, C. O., & Mabel, K. (2025). Preparation And Characterization Of Palm Kernel Shell (Pks) Based

Biocatalyst For The Transformation Of Kernel Oil To Biodiesel. *South African Journal Of Chemical Engineering*, *52*, 200–210. Https:--Doi.Org-10.1016-J.Sajce.2025.02.008

Beasley, M. M., Bartelink, E. J., Taylor, L., & Miller, R. M. (2014). Comparison Of Transmission Ftir, Atr, And Drift Spectra: Implications For Assessment Of Bone Bioapatite Diagenesis. *Journal Of Archaeological Science*, *46*, 16–22. Https:--Doi.Org-10.1016-J.Jas.2014.03.008

Bekele, T., & Alamnie, G. (2025). The Photocatalytic Degradation Of Organic Pollutants-A Comprehensive Overview. *Results In Chemistry*, *18*, 102758. Https:--Doi.Org-10.1016-J.Rechem.2025.102758

Bermeo, M., El Hadri, N., Ravaux, F., Zaki, A., Zou, L., & Jouiad, M. (2020). Adsorption Capacities Of Hygroscopic Materials Based On Nacl-Tio_2 And Nacl-Sio_2 Core-Shell Particles. *Journal Of Nanotechnology*, *2020*, 1–16. Https:--Doi.Org-10.1155-2020-3683629

Chen, S., Hu, Y., Meng, S., & Fu, X. (2014). Study On The Separation Mechanisms Of Photogenerated Electrons And Holes For Composite Photocatalysts G-C3n4-Wo3. *Applied Catalysis B: Environmental*, *150–151*, 564–573. Https:--Doi.Org-10.1016-J.Apcatb.2013.12.053

Chinta, J. P. (2017). Coinage Metal Nanoparticles Based Colorimetric Assays For Natural Amino Acids: A Review Of Recent Developments. *Sensors And Actuators B: Chemical*, *248*, 733–752. Https:--Doi.Org-10.1016-J.Snb.2017.04.028

Coronel, S., Endara, D., Lozada, A. B., Manangón-Perugachi, L. E., & De La Torre, E. (2021). Photocatalytic Study Of Cyanide Oxidation Using Titanium Dioxide (Tio2)-Activated Carbon Composites In A Continuous Flow Photo-Reactor. *Catalysts*, *11*(8), 924. Https:--Doi.Org-10.3390-Catal11080924

Diaz, E., Sanchis, I., Coronella, C. J., & Mohedano, A. F. (2022). Activated Carbons From Hydrothermal Carbonization And Chemical Activation Of Olive Stones: Application In Sulfamethoxazole Adsorption. *Resources*, *11*(5), 43. Https:--Doi.Org-10.3390-Resources11050043

Du, X., Wu, Y., Kou, Y., Mu, J., Yang, Z., Hu, X., & Teng, F. (2019). Amorphous Carbon Inhibited TiO2 Phase Transition In Aqueous Solution And Its Application In Photocatalytic Degradation Of Organic Dye. *Journal Of Alloys And Compounds*, *810*, 151917. Https:--Doi.Org-10.1016-J.Jallcom.2019.151917

Eddy, D. R., Permana, M. D., Sakti, L. K., Sheha, G. A. N., Solihudin, Hidayat, S., Takei, T., Kumada, N., & Rahayu, I. (2023). Heterophase Polymorph Of Tio2 (Anatase, Rutile, Brookite, Tio2 (B)) For Efficient Photocatalyst: Fabrication And Activity. *Nanomaterials*, *13*(4), 704. Https:--Doi.Org-10.3390-Nano13040704

Elina, R., Rori, D. C., & Khair, M. (2023). *Karakterisasi Ftir Pada Karbon Aktif Terimpregnasi Zno*. *7*.

El-Salamony, R. A., Amdeha, E., Ghoneim, S. A., Badawy, N. A., Salem, K. M., & Al-Sabagh, A. M. (2017). Titania Modified Activated Carbon Prepared From Sugarcane Bagasse:

Adsorption And Photocatalytic Degradation Of Methylene Blue Under Visible Light Irradiation. *Environmental Technology*, *38*(24), 3122–3136. Https:--Doi.Org-10.1080-21622515.2017.1290148

Farghaly, A., Maher, E., Gad, A., & El-Bery, H. (2024). Synergistic Photocatalytic Degradation Of Methylene Blue Using Tio2 Composites With Activated Carbon And Reduced Graphene Oxide: A Kinetic And Mechanistic Study. *Applied Water Science*, *14*(10), 228. Https:--Doi.Org-10.1007-S13201-024-02286-0

Farhan, A., Lauren, C. C., & Fuzain, N. A. (2023). Analisis Faktor Pencemaran Air Dan Dampak Pola Konsumsi Masyarakat Di Indonesia. *Jurnal Hukum Dan Ham Wara Sains*, *2*(12), 1095–1103. Https:--Doi.Org-10.58812-Jhhws.V2i12.803

Foroutan, R., Peighambardoust, S. J., Peighambardoust, S. H., Pateiro, M., & Lorenzo, J. M. (2021). Adsorption Of Crystal Violet Dye Using Activated Carbon Of Lemon Wood And Activated Carbon-Fe3o4 Magnetic Nanocomposite From Aqueous Solutions: A Kinetic, Equilibrium And Thermodynamic Study. *Molecules*, *26*(8), 2241. Https:--Doi.Org-10.3390-Molecules26082241

Gavenda, T. (2022). The Chemical Analysis Of Differently Prepared Glass Surfaces - The Comparison Between Edx And Xrf. *Ceramics - Silikaty*, 428–435. Https:--Doi.Org-10.13168-Cs.2022.0038

Ghamarpoor, R., Fallah, A., & Jamshidi, M. (2024). A Review Of Synthesis Methods, Modifications, And Mechanisms Of Zno-Tio_2 -Based Photocatalysts For Photodegradation Of Contaminants. *Acs Omega*, *9*(24), 25457–25492. Https:--Doi.Org-10.1021-Acsomega.3c08717

Guan, S., Cheng, Y., Hao, L., Yoshida, H., Tarashima, C., Zhan, T., Itoi, T., Qiu, T., & Lu, Y. (2023). Oxygen Vacancies Induced Band Gap Narrowing For Efficient Visible-Light Response In Carbon-Doped Tio2. *Scientific Reports*, *13*(1), 14105. Https:--Doi.Org-10.1038-S41598-023-39523-6

Habibullah, M., Ardi Adji, & Rieka Evy Mulyani. (2025). *Statisik Industri Manufaktur Produksi Statisics Of Production Manufacturing Industry: Volume 12*. Badan Pusat Statistik-Bps-Statistics Indonesia.

Hamka, H. (2015). *Tafsir Al-Azhar*. Pustaka Nasional Pte Ltd Singapura.

Handika, G., Maulina, S., & Vidyanova Anggun Mentari. (2018). Karakteristik Karbon Aktif Dari Pemanfaatan Limbah Tanaman Kelapa Sawit Dengan Penambahan Aktivator Natrium Karbonat (Na2co3) Dan Natrium Klorida (Nacl). *Jurnal Teknik Kimia Usu*, *6*(4), 41–44. Https:--Doi.Org-10.32734-Jtk.V6i4.1597

Hartanto, S., & Ratnawati. (2010). Pembuatan Karbon Aktif Dari Tempurung Kelapa Sawit Dengan Metode Aktivasi Kimia. *Indonesian Journal Of Materials Science*, *12*, 12–16.

Hatami, M. H. (2025). Pendidikan Qur'ani: Kajian Tafsir Qs. Al-Qashash Ayat 77 Terhadap Nilai Dan Prinsip. *Al-Fahmu: Jurnal Ilmu Al-Qur'an Dan Tafsir*, *4*(1), 1–13. Https:--Doi.Org-10.58363-Alfahmu.V4i1.260

Hidayati, P., Kimia, J., & Hakim, J. A. R. (2024). *Adsorpsi Zat Warna Remazol Brilliant Blue R Menggunakan Nata De Coco: Optimasi Dosis Adsorben Dan Waktu Kontak*.

Iqbal, M. (2025). *Ekoteologi Islam: Mengintegrasikan Nilai-Nilai Fatwa Mui No. 86 Tahun 2023 Ke Dalam Pola Hidup Berkelanjutan*. *Vol. 2 No. 02*.

Khan, I., Saeed, K., Ali, N., Khan, I., Zhang, B., & Sadiq, M. (2020). Heterogeneous Photodegradation Of Industrial Dyes: An Insight To Different Mechanisms And Rate Affecting Parameters. *Journal Of Environmental Chemical Engineering*, *8*(5), 104364. Https:--Doi.Org-10.1016-J.Jece.2020.104364

Komalasari, M., & Sunendar, B. (2013). *Penggunaan Tio2partikelnanohasil Sintesis Berbasis Air Menggunakan Metoda Sol-Gel Pada Bahan Kapas Sebagai Aplikasi Untuk Tekstil Anti Uv*.

Kumar, R., Choudhary, R., Kolay, S., Pandey, O. P., Singh, K., & Bhargava, P. (2022). Carbon Coated Titanium Dioxide (Cc-Tio_2) As An Efficient Material For Photocatalytic Degradation. *Energy Advances*, *1*(11), 926–934. Https:--Doi.Org-10.1039-D1ya00015b

Kusdarini, E., & Budianto, A. (2022). Characteristics And Adsorption Test Of Activated Carbon From Indonesian Bituminous Coal. *Journal Of Ecological Engineering*, *23*(10), 129–138. Https:--Doi.Org-10.12911-22998993-152343

Le, P. H., Vy, T. T. T., Thanh, V. V., Hieu, D. H., Tran, Q.-T., Nguyen, N.-V. T., Uyen, N. N., Tram, N. T. T., Toan, N. C., Xuan, L. T., Tuyen, L. T. C., Kien, N. T., Hu, Y.-M., & Jian, S.-R. (2024). Facile Preparation Method Of Tio2-Activated Carbon For Photocatalytic Degradation Of Methylene Blue. *Micromachines*, *15*(6), 714. Https:--Doi.Org-10.3390-Mi15060714

Lestari, D., Masriah, I., Hasibuan, A. Y. P., & Pratiwi, P. B. (2026). *Ftir Analysis Of Zno-Functionalized Activated Carbon Derived From Oil Palm Empty Fruit Bunches For Potential Photocatalytic Applications*. *6*(1).

Li, Y., Zhang, S., Yu, Q., & Yin, W. (2007). The Effects Of Activated Carbon Supports On The Structure And Properties Of Tio2 Nanoparticles Prepared By A Sol–Gel Method. *Applied Surface Science*, *253*(23), 9254–9258. Https:--Doi.Org-10.1016-J.Apsusc.2007.05.057

López-Muñoz, M.-J., Grieken, R. V., Aguado, J., & Marugán, J. (2005). Role Of The Support On The Activity Of Silica-Supported Tio2 Photocatalysts: Structure Of The Tio2-Sba-15 Photocatalysts. *Catalysis Today*, *101*(3–4), 307–314. Https:--Doi.Org-10.1016-J.Cattod.2005.03.017

Manh, D. H., Ngoc Nha, T. T., Hong Phong, L. T., Nam, P. H., Thanh, T. D., & Phong, P. T. (2023). Determination Of The Crystalline Size Of Hexagonal La_{1-X} Sr_X Mno_3 (X = 0.3) Nanoparticles From X-Ray Diffraction – A Comparative Study. *Rsc Advances*, *13*(36), 25007–25017. Https:--Doi.Org-10.1039-D3ra04018f

Manurung, M. (2019). Sintesis Dan Karakterisasi Arang Dari Limbah Bambu Dengan Aktivator Zncl2. *Cakra Kimia (Indonesian E-Journal Of Applied Chemistry)*, *7*, 69–77.

Marczewska, A. D., Swiatkowski, A., Trykowski, G., & Biniak, S. (2025). The Effect Of Oxidative Modification Of Activated Carbon On Adsorption Of Aromatic Compounds From Aqueous Solutions. *Molecules*, *30*(18), 3810. Https:--Doi.Org-10.3390-Molecules30183810

Martínez, C., García-Domínguez, Á. E., Guerrero-Robles, F., Saavedra-Díaz, R. O., Torres-Torres, G., Felipe, C., Ojeda-López, R., Silahua-Pavón, A., & Cervantes-Uribe, A. (2020). Synthesis Of Supported Metal Nanoparticles (Au-Tio2) By The Suspension Impregnation Method. *Journal Of Composites Science*, *4*(3), 89. Https:--Doi.Org-10.3390-Jcs4030089

Marwan, M., Hadijah, H., & Mulyani, S. (2022). Pengaruh Konsentrasi Enzim Papain Pada Pakan Terhadap Aktivitas Enzim Pencernaan Ikan Bandeng Chanos Chanos. *Journal Of Aquaculture And Environment*, *4*(2), 39–44. Https:--Doi.Org-10.35965-Jae.V4i2.1454

Masthura, Daulay, A. H., & Jumiati, E. (2018). Effects Of Activation Temperature On Characteristics And Microstructure Of Coconut Shell-Based Activated Carbon. *Eurasian Journal Of Analytical Chemistry*.

Matsna Afwi Nadia & M. Riyan Hidayat. (2023). Fiqh Lingkungan: Analisis Atas Qs. Ar-Rum' [30]: 41 Prespektif Maqasidi. *At-Tahfidz: Jurnal Ilmu Al-Qur'an Dan Tafsir*, *5*(1), 34–48. Https:--Doi.Org-10.53649-At-Tahfidz.V5i1.360

Mattle, M. J., & Thampi, K. R. (2013). Photocatalytic Degradation Of Remazol Brilliant Blue® By Sol–Gel Derived Carbon-Doped Tio2. *Applied Catalysis B: Environmental*, *140–141*, 348–355. Https:--Doi.Org-10.1016-J.Apcatb.2013.04.020

Mendame, L. L., Silangen, P., & Rampengan, A. (2021). Perbandingan Karakteristik Karbon Aktif Arang Tempurung Kelapa Dan Arang Tempurung Kemiri Menggunakan Scanning Electron Microscopic Dan Fourier Transform Infra Red. *Jurnal Fista : Fisika Dan Terapannya*, *2*(2), 105–108. Https:--Doi.Org-10.53682-Fista.V2i2.138

Monshi, A., Foroughi, M. R., & Monshi, M. R. (2012). Modified Scherrer Equation To Estimate More Accurately Nano-Crystallite Size Using Xrd. *World Journal Of Nano Science And Engineering*, *02*(03), 154–160. Https:--Doi.Org-10.4236-Wjnse.2012.23020

Morozzi, P., Ballarin, B., Arcozzi, S., Brattich, E., Lucarelli, F., Nava, S., Gómez-Cascales, P. J., Orza, J. A. G., & Tositti, L. (2021). Ultraviolet–Visible Diffuse Reflectance Spectroscopy (Uv–Vis Drs), A Rapid And Non-Destructive Analytical Tool For The Identification Of Saharan Dust Events In Particulate Matter Filters. *Atmospheric Environment*, *252*, 118297. Https:--Doi.Org-10.1016-J.Atmosenv.2021.118297

Moyo, S., Makhanya, B., & Zwane, P. (2022). Use Of Bacterial Isolates In The Treatment Of Textile Dye Wastewater. *Heliyon*, *8*.

Muchlis, M. (2019). Pelestarian Lingkungan Hidup Dalam Perspektif Hadis: Studi Analisis Hadits Tentang Qadha' Al-Haajah. *Tajdid: Jurnal Pemikiran Keislaman Dan Kemanusiaan*, *3*(2), 163–173. Https:--Doi.Org-10.52266-Tadjid.V3i2.293

Muhsinun, M., & Hidayat, S. (2025). Potensi Karbon Aktif Dari Kulit Durian Dengan Aktivator Hcl Untuk Immobilisasi Asam Lemak Hidroksamat. *Varied Knowledge Journal*, *3*(1), 40–47. Https:--Doi.Org-10.71094-Vkj.V3i1.128

Mukonza, S. S., Chaukura, N., & Mishra, A. K. (2022). Photocatalytic Activity And Reusability Of F, Sm3+ Co-Doped Tio2-Mwcnts Hybrid Heterostructure For Efficient Photocatalytic Degradation Of Brilliant Black Bis-Azo Dye. *Catalysts*, *13*(1), 86. Https:--Doi.Org-10.3390-Catal13010086

Munnik, P., De Jongh, P. E., & De Jong, K. P. (2015). Recent Developments In The Synthesis Of Supported Catalysts. *Chemical Reviews*, *115*(14), 6687–6718. Https:--Doi.Org-10.1021-Cr500486u

Mustafidah, M., & Ikhsan, A. N. (2022). Aplikasi Ftir Sebagai Deteksi Cepat Bahan Non-Halal Dalam Campuran Produk Olahan. *Pharmaceutical And Biomedical Sciences Journal (Pbsj)*, *4*(1), 13–20. Https:--Doi.Org-10.15408-Pbsj.V4i1.24426

Nuh, M., & Husni, A. S. (2025). *Keputusan Munas Dan Konbes Nu 2025 Official*. Pengurus Besar Nahdlatul Ulama.

Nurhayati, A., Ummah, Z. I., & Shobron, S. (2018). *Kerusakan Lingkungan Dalam Al-Qur'an*.

Oko, S., Harjanto, H., Kurniawan, A., & Winanti, C. (2022). Penurunan Kadar Zat Warna Remazol Brilliant Blue R Dengan Metode Adsorpsi Menggunakan Serbuk Caco3 Dari Cangkang Telur Dan Karbon Aktif. *Metana*, *18*(1), 39–45. Https:--Doi.Org-10.14710-Metana.V18i1.45766

Oktaviani, Z., Wahyuni, D., & Nurhanisa, M. (2024). Sintesis Karbon Aktif Dari Tandan Kosong Kelapa Sawit Dengan Aktivator Gelombang Mikro Dan Pengujian Kualitas Berdasarkan Sni 06-3730-1995. *Newton-Maxwell Journal Of Physics*, *5*(1). Https:--Doi.Org-10.33369-Nmj.V5i1.33499

Omri, A., & Benzina, M. (2019). Influence Of The Origin Of Carbon Support On The Structure And Properties Of Tio2 Nanoparticles Prepared By Dip Coating Method. *Arabian Journal Of Chemistry*, *12*(8), 2926–2936. Https:--Doi.Org-10.1016-J.Arabjc.2015.06.027

Pangestuti, M. B., Witoyo, J. E., Institut Teknologi Sumatera, Kurniawan, R. Y., Institut Teknologi Sumatera, Cavendish, A., & Institut Teknologi Sumatera. (2025). Proximate Analysisand Exponential Model Of Activated Carbon From Durian (Durio Zibethinus) Peel From South Lampung. *Jurnal Keteknikan Pertanian Tropis Dan Biosistem*, *13*(3), 315–326. Https:--Doi.Org-10.21776-Ub.Jkptb.2025.013.03.06

Parvathiraja, C., Katheria, S., Siddiqui, M. R., Wabaidur, S. M., Islam, M. A., & Lai, W.-C. (2022). Activated Carbon-Loaded Titanium Dioxide Nanoparticles And Their Photocatalytic And Antibacterial Investigations. *Catalysts*, *12*(8), 834. Https:--Doi.Org-10.3390-Catal12080834

Pastor, R. L., M.G. Pinna-Hernández, J.A. Sánchez Molina, & F.G. Acién Fernández. (2025). Influence Of The Moisture And Ash Content In Flue Gases On The Performance Of Adsorption Processes Using Activated Carbons To Capture The Co2 For Reuse In

Greenhouses. *Heliyon*, *11*(1), E40346. Https:--Doi.Org-10.1016-J.Heliyon.2024.E40346

Pingmuang, K., Chen, J., Kangwansupamonkon, W., Wallace, G. G., Phanichphant, S., & Nattestad, A. (2017). Composite Photocatalysts Containing Bivo4 For Degradation Of Cationic Dyes. *Scientific Reports*, *7*(1), 8929. Https:--Doi.Org-10.1038-S41598-017-09514-5

Poluakan, M., Wuntu, A., & Sangi, M. S. (2015). Aktivitas Fotokatalitik Tio2 – Karbon Aktif Dan Tio2 – Zeolit Pada Fotodegradasi Zat Warna Remazol Yellow. *Jurnal Mipa*, *4*(2), 137. Https:--Doi.Org-10.35799-Jm.4.2.2015.9038

Ramadhan, M. (2019). *Maqasidsyari'ahdan Lingkungan Hidup*. *21*(2).

Rápó, E., & Tonk, S. (2021). Factors Affecting Synthetic Dye Adsorption; Desorption Studies: A Review Of Results From The Last Five Years (2017–2021). *Molecules*, *26*(17), 5419. Https:--Doi.Org-10.3390-Molecules26175419

Ren, W., Ai, Z., Jia, F., Zhang, L., Fan, X., & Zou, Z. (2007). Low Temperature Preparation And Visible Light Photocatalytic Activity Of Mesoporous Carbon-Doped Crystalline Tio2. *Applied Catalysis B: Environmental*, *69*(3–4), 138–144. Https:--Doi.Org-10.1016-J.Apcatb.2006.06.015

Řepecká, L., Bednárek, J., Stachurová, T., Gavlová, A., Smutná, K., Vaštyl, J., Šváb, M., & Vráblová, M. (2026). Impregnation Of Activated Carbon With Ionic Liquids For Simultaneous Removal Of Micropollutants And Antibiotic-Resistant Bacteria From Wastewater. *Emerging Contaminants*, *12*(1), 100615. Https:--Doi.Org-10.1016-J.Emcon.2025.100615

Rizkiana, J., Suyadi, A. F., Auliardi, D., Devianto, H., & Soerawidjaja, T. H. (2020). Karakterisasi Fotokatalis Untuk Fotoreduksi Karbon Dioksida Menjadi Asam Format Dalam Fasa Akuatik. *Indonesian Journal Of Chemical Research*, *8*(1), 35–42.

Ruliza, M. O., Agustina, T. E., & Mohadi, R. (2018). Impregnation Of Activated Carbon-Tio_2 Composite And Its Application In Photodegradation Of Procion Red Synthetic Dye In Aqueous Medium. *Iop Conference Series: Earth And Environmental Science*, *105*, 012024. Https:--Doi.Org-10.1088-1755-1315-105-1-012024

Ruswanda, A. S. (2025). Mengkaji Konsep Ekoteologi Menurut Nasaruddin Umar. *Jurnal Keislaman*, *8*(2), 532–545. Https:--Doi.Org-10.54298-Jk.V8i2.667

Safni, Putri, A. N., Deswati, D., & Zilfa, Z. (2024). Degradation Of Remazol Yellow Fg By Sonolysis And Photolysis With Tio2-Active Carbon Rice Husk (Tio2-Ac) Catalyst And Analysis Using Spectrophotometer Uv-Vis. *Jurnal Kimia Unand*, *13*(2), 34–40. Https:--Doi.Org-10.25077-Jku.13.2.34-40.2024

Saputra, A. D. (2018). *Impregnasi Dan Karakterisasi K-Deoiled Spent Bleaching Earth (K-Dsbe) Dengan Metode Basah*. *15*.

Shaban, M., Ashraf, A. M., & Abukhadra, M. R. (2018). Tio2 Nanoribbons-Carbon Nanotubes Composite With Enhanced Photocatalytic Activity; Fabrication, Characterization, And Application. *Scientific Reports*, *8*(1), 781. Https:--Doi.Org-10.1038-S41598-018-19172-W

Shao, X., Lu, W., Zhang, R., & Pan, F. (2013a). Enhanced Photocatalytic Activity Of Tio2-C Hybrid Aerogels For Methylene Blue Degradation. *Scientific Reports*, *3*(1), 3018. Https:--Doi.Org-10.1038-Srep03018

Shao, X., Lu, W., Zhang, R., & Pan, F. (2013b). Enhanced Photocatalytic Activity Of Tio2-C Hybrid Aerogels For Methylene Blue Degradation. *Scientific Reports*, *3*(1), 3018. Https:--Doi.Org-10.1038-Srep03018

Shihab, Q. (2002). *Tafsir-Al-Mishbah-Jilid-01-M.-Quraish-Shihab-Z-Library-1* (Vol. 15). Lentera Hati.

Simamora, C. J. K., & Sukmawati, S. (2020). Identifikasi Dan Karakterisasi Aktivitas Ekstrak Kasar Enzim Lipase Isolat Bakteri Lipolitik Lptk 19 Asal Tempe Biji Karet. *Median : Jurnal Ilmu Ilmu Eksakta*, *12*(1), 28–37. Https:--Doi.Org-10.33506-Md.V12i1.834

Siswanti, S., Oktafiana, A. H., & Putri, Y. (2023). Adsorpsi Zat Warna Remazol Brilliant Blue R Pada Limbah Industri Batik Menggunakan Adsorben Dari Mahkota Buah Nanas. *Eksergi*, *21*(1), 9. Https:--Doi.Org-10.31315-E.V21i1.10669

Skoog, D. A., Holler, F. J., & Crouch, Stanley. (2016). *Principles Of Instrumental Analysis Seventh Edition* (Vol. 88). Https:--Doi.Org-10.1515-Pac-2015-0305

Subagja, R., Royani, A., & Suharyanto, A. (2014). *Pengaruh Temperatur Dan Waktu Kalsinasi Terhadap Perubahan Fasa Tio2*.

Sugandi, D., Wahyuni, N., & Rahmalia, W. (2024). Fotocatalytic Degradation Of Methylene Blue By Floating Tio2-Coconut Fiber. *Acta Chimica Asiana*, *7*(1), 437–442. Https:--Doi.Org-10.29303-Aca.V7i1.183

Thompson, T. J. U., Gauthier, M., & Islam, M. (2009). The Application Of A New Method Of Fourier Transform Infrared Spectroscopy To The Analysis Of Burned Bone. *Journal Of Archaeological Science*, *36*(3), 910–914. Https:--Doi.Org-10.1016-J.Jas.2008.11.013

Tichapondwa, S. M., Newman, J. P., & Kubheka, O. (2020). Effect Of Tio2 Phase On The Photocatalytic Degradation Of Methylene Blue Dye. *Physics And Chemistry Of The Earth, Parts A-B-C*, *118–119*, 102900. Https:--Doi.Org-10.1016-J.Pce.2020.102900

Tsaousi, G. M., Toli, A., Bempelou, A., Kotsanis, D., Vafeias, M., Balomenos, E., & Panias, D. (2023). Control Of Silica Gel Formation In The Acidic Leaching Of Calcium Aluminate Slags With Aqueous Hcl For Al Extraction. *Sustainability*, *15*(21), 15462. Https:--Doi.Org-10.3390-Su152115462

Ulya, L. H., Fatimah, H., & Alif, N. (2022). Photodegradation Of Indigosol Blue Dye Using Tio2-Natural Zeolite Photocatalyst. *Jurnal Kimia Valensi*, *8*(1), 54–59. Https:--Doi.Org-10.15408-Jkv.V8i1.24558

Ulya, L. H., Setiawan, A. P., Setyaputra, I. A. E., & Maghfiroh. (2025). Enhanced Photocatalytic Degradation Activity Of Methyl Violet Dyes Utilizing Tio_2 -Natural Zeolite Composite. *Iop Conference Series: Earth And Environmental Science*, *1439*(1), 012030. Https:--Doi.Org-10.1088-1755-1315-1439-1-012030

Usman, K. A. S., Buenviaje, S. C., & Edañol, Y. D. G. (2026). Nano-Sodalite Immobilization Enables Processable And Reusable Titanium Dioxide Photocatalysts. *Nano Select*, *7*(5), E70153. Https:--Doi.Org-10.1002-Nano.70153

Vargas, R., & Núñez, O. (2009). Hydrogen Bond Interactions At The Tio2 Surface: Their Contribution To The Ph Dependent Photo-Catalytic Degradation Of P-Nitrophenol. *Journal Of Molecular Catalysis A: Chemical*, *300*(1–2), 65–71. Https:--Doi.Org-10.1016-J.Molcata.2008.10.029

Wang, W., Lemaire, R., Bensakhria, A., & Luart, D. (2022). Review On The Catalytic Effects Of Alkali And Alkaline Earth Metals (Aaems) Including Sodium, Potassium, Calcium And Magnesium On The Pyrolysis Of Lignocellulosic Biomass And On The Co-Pyrolysis Of Coal With Biomass. *Journal Of Analytical And Applied Pyrolysis*, *163*, 105479. Https:--Doi.Org-10.1016-J.Jaap.2022.105479

Wang, Y., Li, L., Huang, X., Li, Q., & Li, G. (2015). New Insights Into Fluorinated Tio_2 (Brookite, Anatase And Rutile) Nanoparticles As Efficient Photocatalytic Redox Catalysts. *Rsc Advances*, *5*(43), 34302–34313. Https:--Doi.Org-10.1039-C4ra17076h

Wibowo, S., Syafi, W., & Pari, G. P. (2011). Karakterisasi Permukaan Arang Aktif Tempurung Biji Nyamplung. *Makara Of Technology Series*, *15*(1). Https:--Doi.Org-10.7454-Mst.V15i1.852

Xia, T., Zhang, W., Wang, Z., Zhang, Y., Song, X., Murowchick, J., Battaglia, V., Liu, G., & Chen, X. (2014). Amorphous Carbon-Coated Tio2 Nanocrystals For Improved Lithium-Ion Battery And Photocatalytic Performance. *Nano Energy*, *6*, 109–118. Https:--Doi.Org-10.1016-J.Nanoen.2014.03.012

Yankovych, H. B., Abreu-Jaureguí, C., Farrando-Perez, J., Melnyk, I., Václavíková, M., & Silvestre-Albero, J. (2024). Advanced Removal Of Dyes With Tuning Carbon-Tio2 Composite Properties. *Nanomaterials*, *14*(3), 309. Https:--Doi.Org-10.3390-Nano14030309

Yue, Y., Yue, X., Tang, X., Han, L., Wang, J., Wang, S., & Du, C. (2024a). Synergistic Adsorption And Photocatalysis Study Of Tio2 And Activated Carbon Composite. *Heliyon*, *10*(10), E30817. Https:--Doi.Org-10.1016-J.Heliyon.2024.E30817

Yue, Y., Yue, X., Tang, X., Han, L., Wang, J., Wang, S., & Du, C. (2024b). Synergistic Adsorption And Photocatalysis Study Of Tio2 And Activated Carbon Composite. *Heliyon*, *10*(10), E30817. Https:--Doi.Org-10.1016-J.Heliyon.2024.E30817

Yue, Y., Yue, X., Tang, X., Han, L., Wang, J., Wang, S., & Du, C. (2024c). Synergistic Adsorption And Photocatalysis Study Of Tio2 And Activated Carbon Composite. *Heliyon*, *10*(10), E30817. Https:--Doi.Org-10.1016-J.Heliyon.2024.E30817

Yuliusman, Nasruddin, Afdhol, M. K., Amiliana, R. A., & Hanafi, A. (2017). Preparation Of Activated Carbon From Palm Shells Using Koh And $Zncl_2$ As The Activating Agent. *Iop Conference Series: Earth And Environmental Science*, *75*, 012009. Https:--Doi.Org-10.1088-1755-1315-75-1-012009

Zaaboul, F., Canle, M., Haoufazane, C., Santaballa, J. A., Hammouti, B., Azzaoui, K., Jodeh, S., Hadjadj, A., & El Hourch, A. (2024). Sunlight-Driven Photodegradation Of Rb49 Dye Using Tio2-P25 And Tio2-Uv100: Performance Comparison. *Coatings*, *14*(10), 1270. Https:--Doi.Org-10.3390-Coatings14101270

Zaleska, A. (2008). Doped-Tio2: A Review. *Recent Patents On Engineering*, *2*(3), 157–164. Https:--Doi.Org-10.2174-187221208786306289

Žerjav, G., Žižek, K., Zavašnik, J., & Pintar, A. (2022). Brookite Vs. Rutile Vs. Anatase: What`S Behind Their Various Photocatalytic Activities? *Journal Of Environmental Chemical Engineering*, *10*(3), 107722. Https:--Doi.Org-10.1016-J.Jece.2022.107722

Zheng, H., Jiang, X., Gao, Y., & Tong, A. (2022). *Chemical Looping Reforming: Process Fundamentals And Oxygen Carriers*. *2*. Https:--Doi.Org-Https:--Doi.Org-10.1007-S43938-022-00012-3

Zheng, H., Jiang, X., Gao, Y., Tong, A., & Zeng, L. (2022). Chemical Looping Reforming: Process Fundamentals And Oxygen Carriers. *Discover Chemical Engineering*, *2*(1), 5. Https:--Doi.Org-10.1007-S43938-022-00012-3

Zulkania, A., Iqbal, M., & Syamsumarlin, S. (2020). Characterization Of Adsorbents Derived From Palm Fiber Waste And Its Potential On Methylene Blue Adsorption. *Key Engineering Materials*, *841*, 273–277. Https:--Doi.Org-10.4028-Www.Scientific.Net-Kem.841.273

APPENDICES

Appendix 1 Research Design

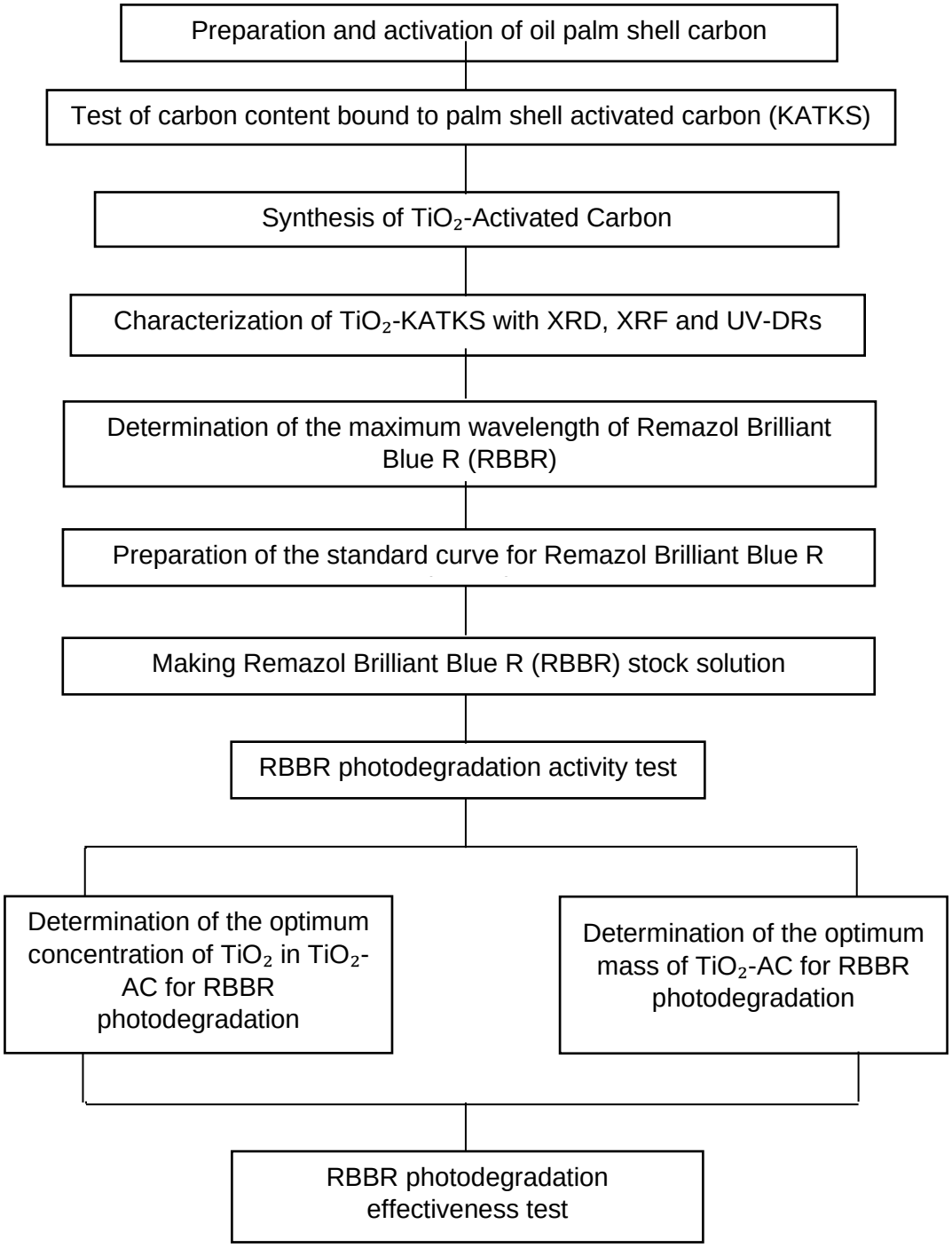

Appendix 2 Research Flowchart

L.2.1 Preparation and Activation of Carbon from Palm Oil Shells

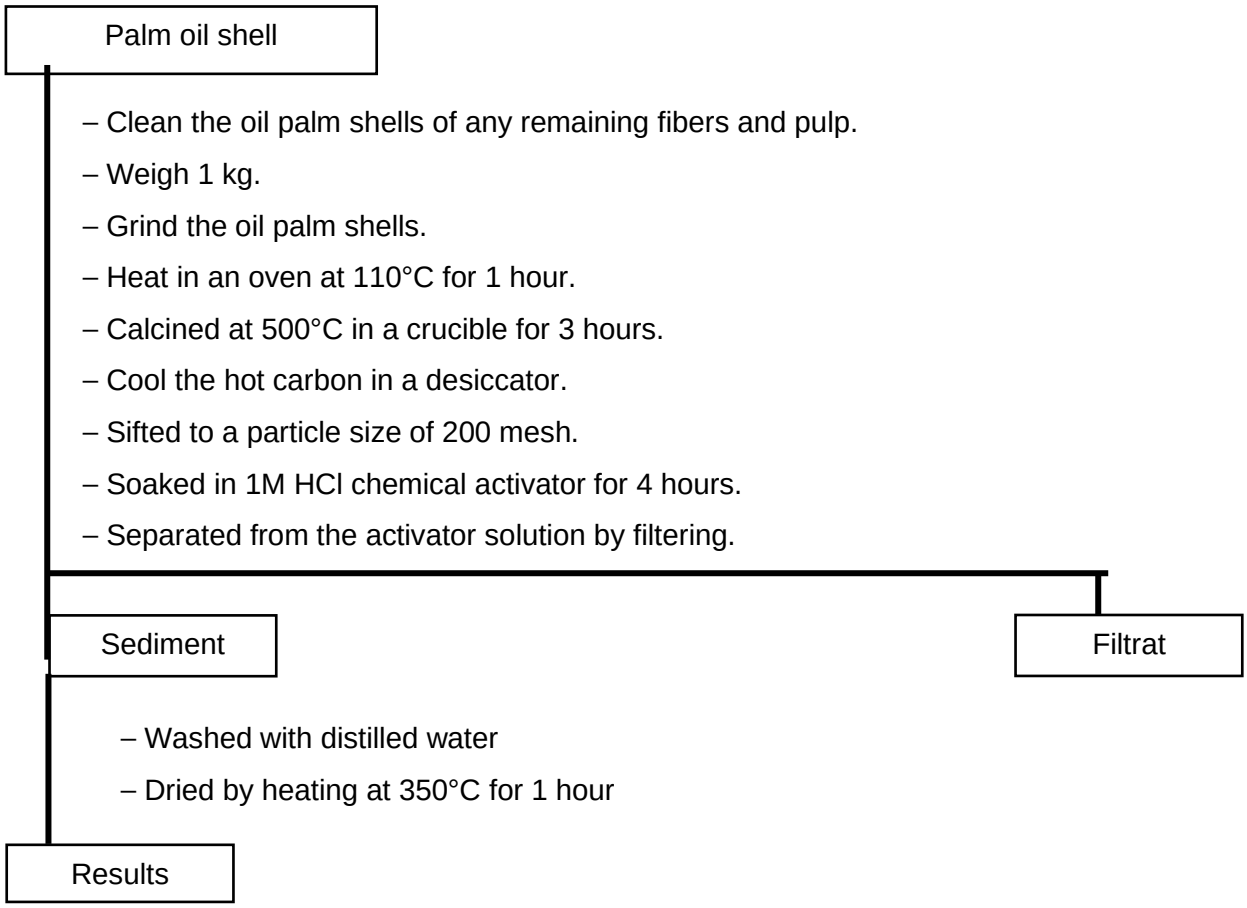

L.2.2 Palm Shell Activated Carbon Water Content Test

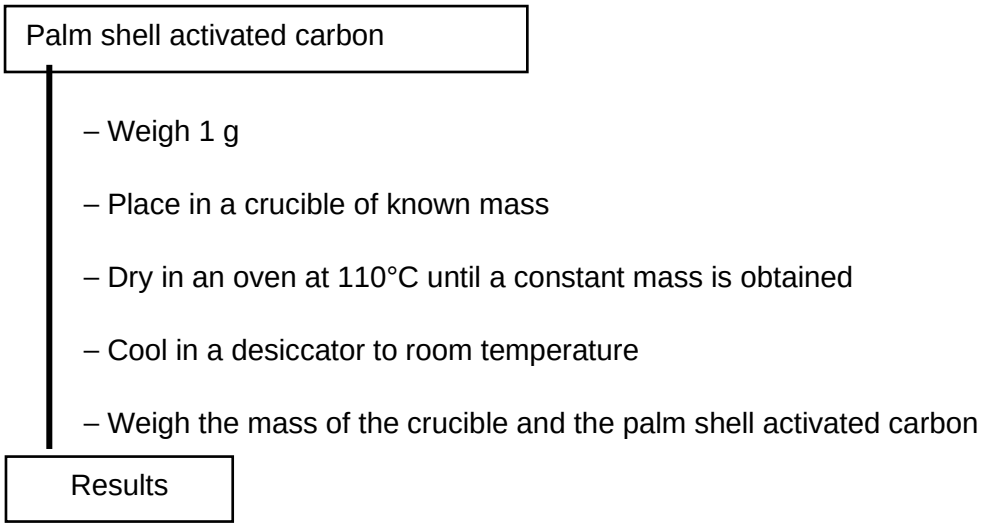

L.2.3 Test for Volatile Substance Contents of Palm Shell Activated Carbon

Palm shell activated carbon

– Weigh the palm shell activated carbon that has been tested for moisture content
– Heat it in a 900°C furnace for 15 minutes
– Cool it in a desiccator to room temperature
– Weigh the mass of the crucible and the palm shell activated carbon

Results

L.2.4 Palm Oil Shell Activated Carbon Ash Content Test

Palm shell activated carbon

– Weigh the palm shell activated carbon that has been tested for moisture and volatile matter content.
– Incinerate in a furnace at 900°C for 4 hours.
– Cool in a desiccator to room temperature.
– Weigh the mass of the crucible and the ash of the palm shell activated carbon formed.

Results

L.2. 5 Test of Bound Carbon Content of Palm Oil Shell Activated Carbon

Palm shell activated carbon

– Calculate the difference between the results of the process of reducing water content, volatile matter content, and total ash content.

Results

L.2.6 Synthesis of TiO_2-Palm Shell Activated Carbon Using the Impregnation Method

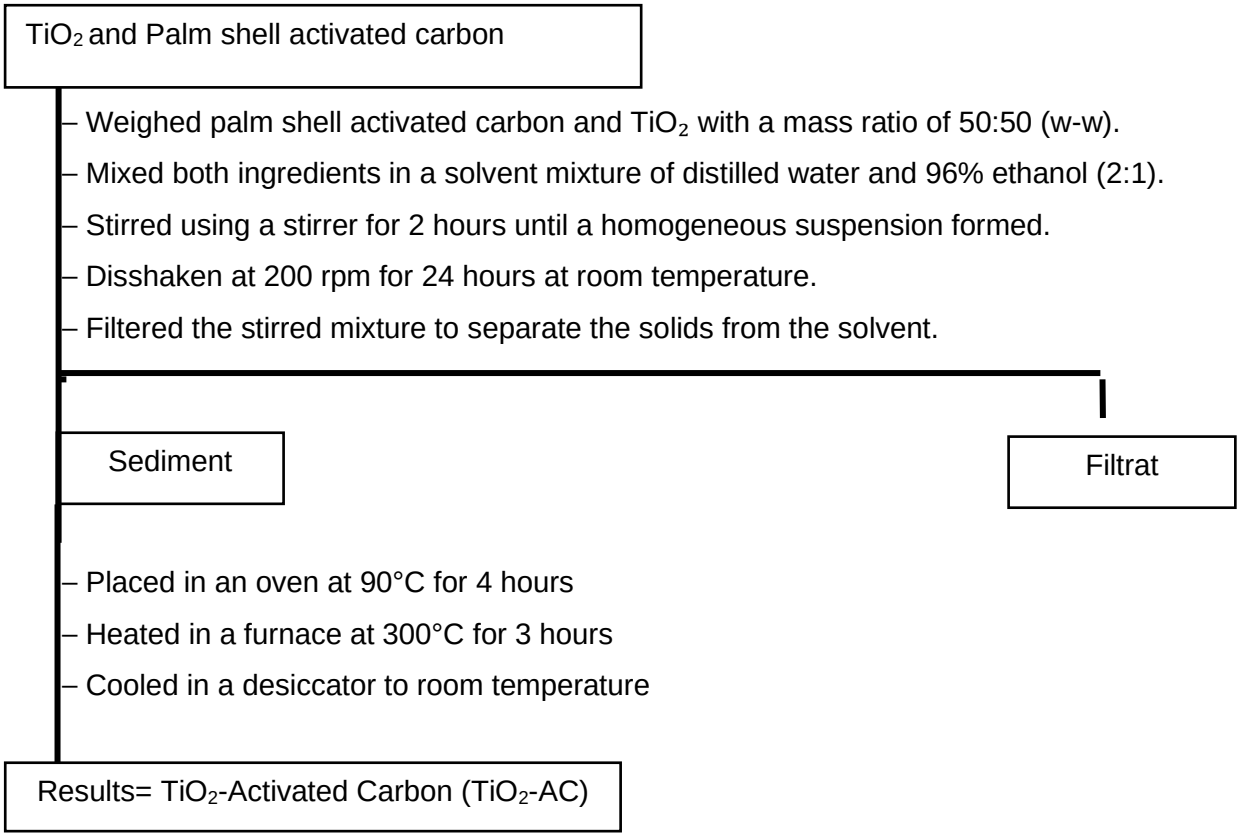

L.2.7 Identification of the Crystal Structure of TiO2 Photocatalyst-Palm Shell Activated Carbon Using X-Ray Diffraction (XRD)

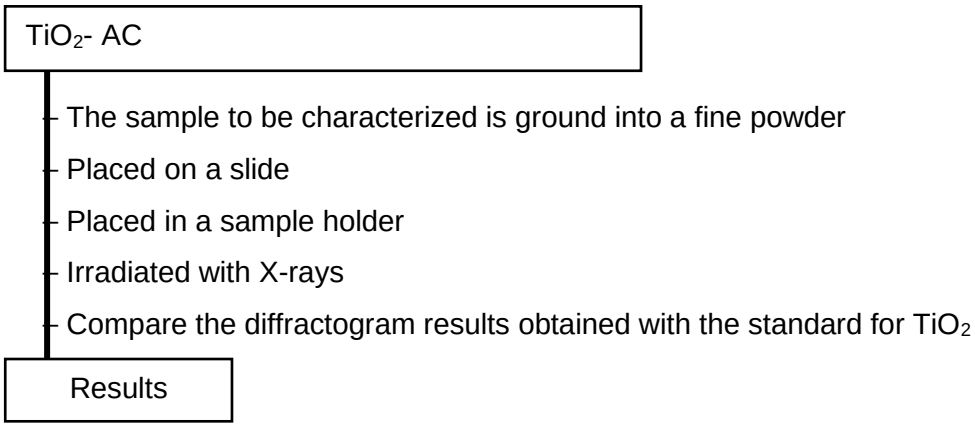

L.2.8 Identification of the Elemental Composition of TiO_2 Photocatalyst-Palm Shell Activated Carbon Using X-Ray Fluorescence (XRF)

TiO_2-AC

– A photocatalyst sample was prepared in the form of a fine powder.
– The powder sample was placed in the sample holder of the XRF instrument.
– The sample was irradiated with X-rays to strike the electrons of the constituent atomic nuclei.
– The fluorescence emission emitted by the atoms in the sample was detected.
– The sample was tested with a 1200-volt voltage source using Cu radiation at a voltage of 40 kV and a current of 25 mA.
– The fluorescence spectrum was obtained, which was analyzed to determine the percentage of the constituent elements of the material.

Results

L.2.9 Identification of the Elemental Composition of TiO_2-Palm Shell Activated Carbon Photocatalyst Using UV-Vis DRS

TiO_2-AC

– Prepare a photocatalyst sample in the form of a fine powder
– Place the sample in the sample holder of the UV-Vis DRS instrument
– Measure the reflectance of the sample in the wavelength range of 200–800 nm
– Transform the reflectance data using the Kubelka-Munk equation
– Plot the transformed data onto a Tauc plot [F(R)·hv]n[F(R)·hv]^n[F(R)·hv]n against the photon energy (hv)
– Determine the band gap energy value from the intersection of the linear curve with the photon energy axis

Results

L.2.10 Photodegradation of Remazol Brilliant Blue R with Variations in Remazol Brilliant Blue R Solution Concentration

Remazol Brilliant Blue R Solution

– Remazol Brilliant Blue R solution was taken with varying initial concentrations of 10, 20, 30, 40, and 50 ppm into a test tube.

– TiO_2-AC photocatalyst with an optimum mass of 0.1 g was added.

– The solution mixture was placed in a photoreactor and irradiated with UV light for 120 minutes.

– The degradation solution was filtered and centrifuged for 20 minutes.

Filtrat

Supernatan

– The absorbance was measured using a UV-Vis Spectrophotometer at its maximum wavelength

– Performed in triplicate

Results

L.2.10 Photodegradation of Remazol Brilliant Blue R with Variation of TiO_2-Activated Carbon Mass

TiO_2-AC

– Take 25 mL of Remazol Brilliant Blue R 10 ppm solution

– Place in 5 different test tubes

– Add TiO_2-AC photocatalyst with varying masses of 0.05 g, 0.1 g, 0.2 g, 0.3 g, and 0.4 g

– Place the solution mixture into a photoreactor and irradiate it with UV light for 120 minutes

– Filter and centrifuge the degradation solution for 20 minutes

Filtrat

Supernatan

– The absorbance was measured using a UV-Vis Spectrophotometer at its maximum wavelength

– Performed in triplicate

Results

L.2.11 Effectiveness Test Against Degradation of Remazol Brilliant Blue R with Optimum Composition and Mass

TiO_2-AC, RBBR, TiO_2, Activated Carbon

— A 25 mL solution of Remazol Brilliant Blue R 10 ppm was taken into a 100 mL glass beaker.

— The effectiveness was tested with 5 variations of sample conditions, namely:

- The RBBR solution was irradiated with UV light for 120 minutes (control)
- The RBBR solution was supplemented with TiO_2 (optimum mass 0.1 g) and irradiated with UV light for 120 minutes
- The RBBR solution was supplemented with activated carbon (0.1 g) and irradiated with UV light for 120 minutes
- The RBBR solution was supplemented with TiO_2-AC photocatalyst (optimum mass 0.03 g; optimum concentration 10 ppm) and irradiated with UV light for 120 minutes

— Place all beakers into the photoreactor

— Irradiate with UV light according to the treatment variations for 120 minutes

– Filter and centrifuge the photodegradation solution for 20 minutes

Filtrat

Supernatan

– The absorbance was measured using a UV-Vis Spectrophotometer at the maximum wavelength (λmax) of RBBR

– Performed in triplicate to obtain valid results

– Performed in triplicate

Results

Appendix 3 Calculation of Raw Material Solution Preparation

L.3.1 Preparation of 1 M HCl Solution.

The commercial HCl concentration is known to be 37% w-w

Molecular Weight of HCl: 36.46 g-mol

ρ HCl: 1,18 g-ml

M $: \frac{10\ x\ \%\ konsentration\ x\ density}{Molecular\ Weight}$

M $: \frac{10\ x\ 37\%\ x\ 1{,}18\ g-ml}{Berat\ 36{,}46\ g-mol}$ = 12 M

Preparation of 100 ml of 1 M HCl

Given:

M1=12 M2=1

V1=? V2=100 ml

M1.V1 = M2.V2

12.X = 1.100

X= $\frac{1x100}{12}$ = 8,3 ml

L.3.2 Preparation of RBBR Stock Solution (100 ppm, 250 mL)

Given:

Concentration of RBBR = 100 ppm = 100 mg-L

Volume (V) = 250 mL = 0.25 L

Using the formula:

Concentration = Mass - Volume (mg-L)

Mass = Concentration × Volume

Mass = 100 mg-L × 0.25 L

Mass = **25 m**

L.3.3 Preparation of RBBR Standard Solutions (10, 20, 30, 40, and 50 ppm)

L.3.3.1 Standard Solution 10 ppm

$M_1V_1 = M_2V_2$

100 ppm × V_1 = 10 ppm × 100 mL

V_1 = 10 mL

L.3.3.2 Standard Solution 20 ppm

$M_1V_1 = M_2V_2$

100 ppm × V_1 = 20 ppm × 100 mL

V_1 = 20 mL

L.3.3.3 Standard Solution 30 ppm

$M_1V_1 = M_2V_2$

100 ppm × V_1 = 30 ppm × 100 mL

V_1 = 30 mL

L.3.3.4 Standard Solution 40 ppm

$M_1V_1 = M_2V_2$

100 ppm × V_1 = 40 ppm × 100 mL

V_1 = 40 mL

L.3.3.5 Standard Solution 50 ppm

$M_1V_1 = M_2V_2$

100 ppm × V_1 = 50 ppm × 100 mL

V_1 = 50 mL

L.3.4 Preparation of RBBR Solution (10 ppm, 100 mL)

$M_1V_1 = M_2V_2$

100 ppm × V_1 = 10 ppm × 100 mL

V_1 = 10 mL

Appendix 4 Raw Research Data

L.4.1 XRD

A. XRD Karbon Aktif

Peak List

General information

Analysis date	2026/01/22 23:39:26		
Sample name		Measurement date	2026/01/22 23:21:51
File name	Karbon Aktif.ras	Operator	administrator
Comment			

Peak list

No.	2-theta(deg)	d(ang.)	Height(cps)	FWHM(deg)	Int. I(cps deg)	Int. W(deg)	Asym. factor
1	22.90(6)	3.881(11)	1501(112)	10.01(6)	17030(117)	11.3(9)	1.23(3)
2	41.8(3)	2.161(15)	80(26)	2.1(5)	268(138)	3(3)	1.1(9)
3	45.6(6)	1.99(2)	106(30)	8.6(10)	1621(156)	15(6)	0.50(15)

Measurement profile

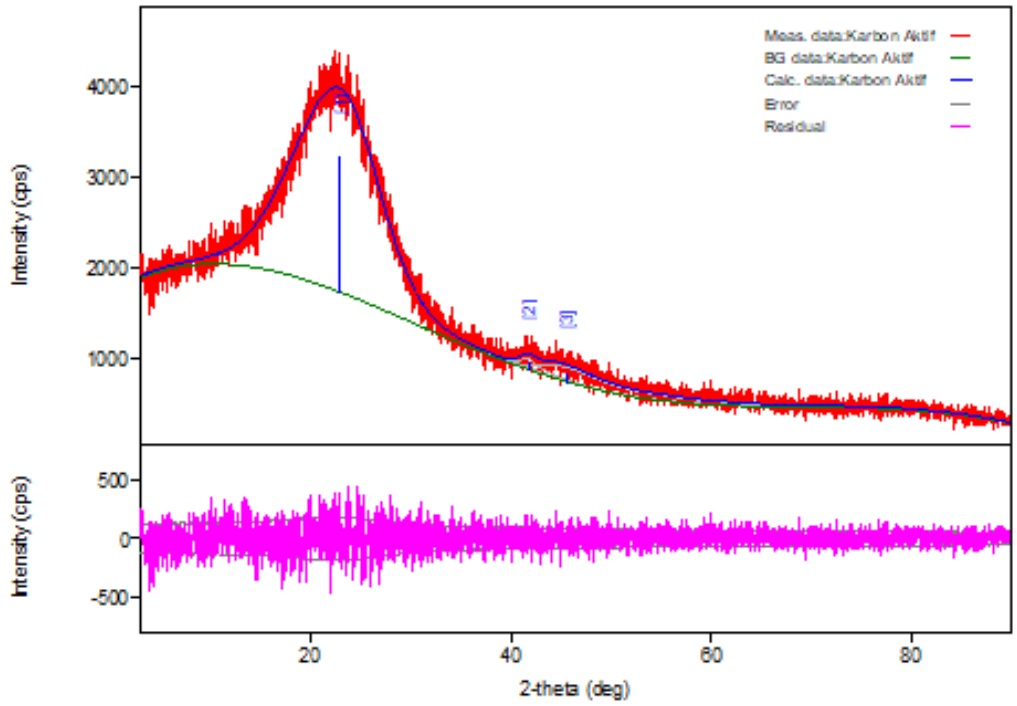

B. XRD TiO_2

Peak List

General information

Analysis date	2026/01/22 23:18:41		
Sample name		Measurement date	2026/01/22 22:45:15
File name	TiO2 anatase.ras	Operator	administrator
Comment			

Peak list

No.	2-theta(deg)	d(ang.)	Height(cps)	FWHM(deg)	Int. I(cps deg)	Int. W(deg)	Asym. factor
1	25.414(4)	3.5019(6)	6659(236)	0.236(3)	1989(18)	0.299(13)	1.43(11)
2	37.018(6)	2.4265(4)	523(66)	0.17(3)	136(10)	0.26(5)	0.6(5)
3	37.918(13)	2.3709(8)	1595(115)	0.230(10)	467(15)	0.29(3)	1.5(4)
4	38.65(3)	2.3276(18)	470(63)	0.23(3)	146(11)	0.31(7)	0.9(5)
5	48.161(9)	1.8879(3)	2440(143)	0.215(8)	708(10)	0.29(2)	1.6(3)
6	54.023(10)	1.6961(3)	1508(112)	0.225(11)	453(9)	0.30(3)	1.8(4)
7	55.192(10)	1.6629(3)	1519(113)	0.225(11)	451(9)	0.30(3)	1.7(3)
8	62.234(10)	1.4905(2)	310(51)	0.16(2)	70(6)	0.23(6)	1.4(3)
9	62.812(9)	1.47821(19)	1228(101)	0.210(13)	370(9)	0.30(3)	1.4(3)
10	68.881(16)	1.3620(3)	550(68)	0.23(2)	181(6)	0.33(5)	1.5(5)
11	70.405(13)	1.3362(2)	599(71)	0.228(15)	170(6)	0.28(4)	1.3(3)
12	75.167(11)	1.26295(16)	877(85)	0.221(12)	263(7)	0.30(4)	1.6(4)
13	76.138(18)	1.2492(3)	312(51)	0.13(3)	68(4)	0.22(5)	1.4(10)
14	80.891(13)	1.18740(15)	65(23)	0.17(5)	12(3)	0.18(12)	5(8)
15	82.27(2)	1.1710(3)	77(25)	0.20(6)	21(6)	0.28(16)	1.7(10)
16	82.791(15)	1.16490(17)	414(59)	0.23(2)	131(9)	0.32(7)	1.7(10)
17	83.269(16)	1.15943(19)	200(41)	0.22(4)	61(8)	0.31(10)	1.7(10)
18	87.88(5)	1.1101(5)	38(18)	0.12(9)	7(2)	0.19(15)	5(15)

Measurement profile

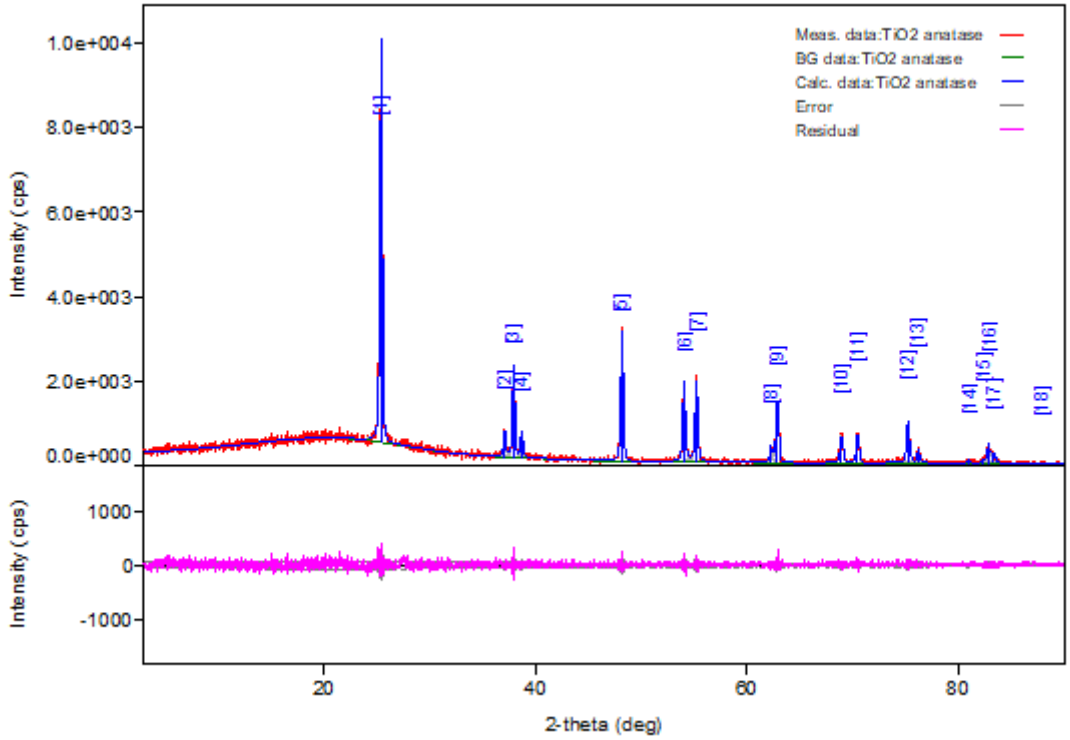

C. XRD TiO_2-AC

Peak List

General information

Analysis date	2026/01/22 23:19:32		
Sample name		Measurement date	2026/01/22 22:55:44
File name	TiO2_KA.ras	Operator	administrator
Comment			

Peak list

No.	2-theta(deg)	d(ang.)	Height(cps)	FWHM(deg)	Int. I(cps deg)	Int. W(deg)	Asym. factor
1	25.432(5)	3.4994(6)	8683(269)	0.193(4)	2233(19)	0.257(10)	2.3(3)
2	37.035(13)	2.4254(8)	600(71)	0.154(19)	132(9)	0.22(4)	0.6(2)
3	37.906(9)	2.3715(5)	2207(136)	0.169(10)	525(12)	0.24(2)	1.4(3)
4	38.668(12)	2.3266(7)	768(80)	0.144(18)	161(8)	0.21(3)	1.3(5)
5	48.149(5)	1.88834(18)	3539(172)	0.152(6)	765(10)	0.216(13)	1.32(19)
6	53.993(7)	1.69692(19)	2052(131)	0.165(9)	495(9)	0.24(2)	1.1(2)
7	55.174(6)	1.66336(16)	2202(135)	0.153(7)	468(9)	0.213(17)	1.5(3)
8	62.204(9)	1.49120(19)	345(54)	0.158(19)	75(5)	0.22(5)	0.85(16)
9	62.780(7)	1.47889(14)	1594(115)	0.166(8)	362(8)	0.23(2)	0.85(16)
10	68.842(15)	1.3627(3)	578(69)	0.184(16)	158(6)	0.27(4)	1.0(4)
11	70.383(10)	1.33661(16)	732(78)	0.174(10)	163(6)	0.22(3)	1.1(3)
12	74.16(4)	1.2775(5)	64(23)	0.16(6)	15(4)	0.23(15)	2(2)
13	75.127(9)	1.26352(13)	1102(96)	0.177(9)	289(8)	0.24(3)	0.8(2)
14	76.155(17)	1.2490(2)	358(55)	0.148(18)	75(6)	0.21(5)	2.7(19)
15	80.82(4)	1.1883(5)	48(20)	0.22(9)	14(4)	0.3(2)	1(2)
16	82.33(3)	1.1702(3)	78(26)	0.19(6)	20(7)	0.26(17)	1.8(7)
17	82.774(14)	1.16510(17)	478(63)	0.187(16)	122(12)	0.25(6)	1.8(7)
18	83.21(3)	1.1600(3)	155(36)	0.31(9)	65(14)	0.42(19)	1.8(7)

Measurement profile

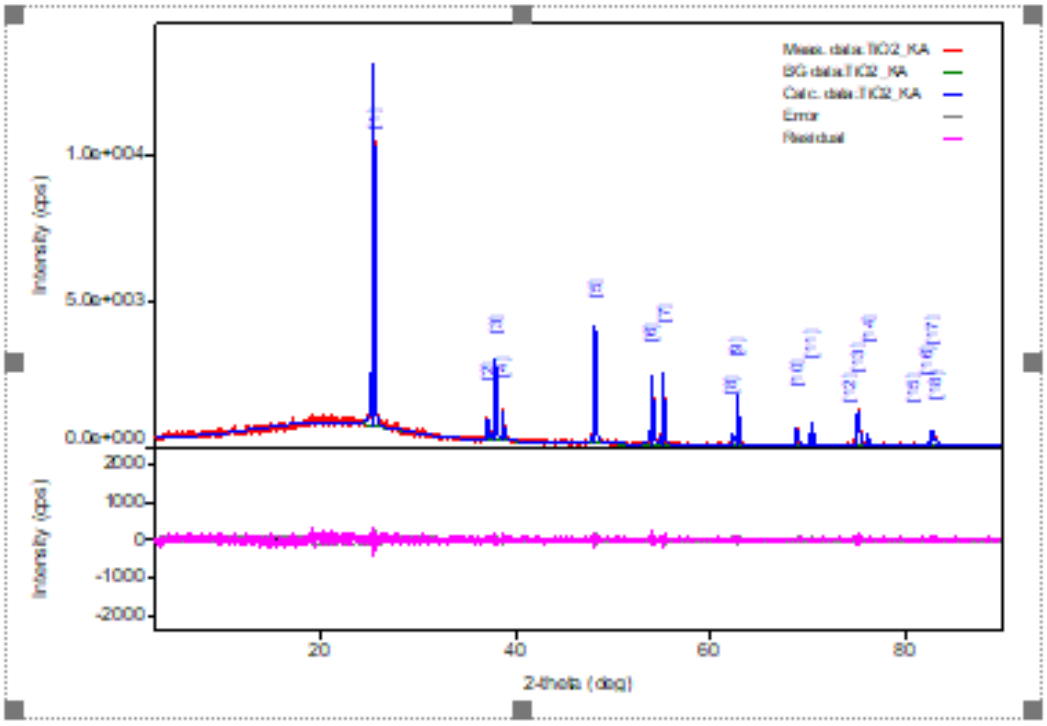

L.4.2 XRF

27-jan-2026 10:58:51

Sample results

Sample ident
XRF 36

Application	<Standardless>
Sequence	1 of 1
Measurement time	27-jan-2026 10:08:29
Position	3

Compound	SiO2	P2O5	K2O	CaO	TiO2	Cr2O3	MnO	Fe2O3	NiO	CuO	ZnO	Yb2O3
Conc	51	7,9	2,5	9,61	0,58	0,56	0,44	20,4	0,6	2,0	0,3	1
Unit	%	%	%	%	%	%	%	%	%	%	%	%

Compound	Re2O7
Conc	3
Unit	%

27-jan-2026 10:58:41

Sample results

Sample ident
XRF 35

Application	<Standardless>
Sequence	1 of 1
Measurement time	27-jan-2026 10:06:28
Position	2

Compound	SiO2	P2O5	K2O	CaO	TiO2	Cr2O3	MnO	Fe2O3	NiO	CuO	Yb2O3	Au
Conc	18	5,2	32,6	22,8	0,35	0,39	0,61	17,4	0,3	0,89	0,6	1,1
Unit	%	%	%	%	%	%	%	%	%	%	%	%

27-jan-2026 10:58:28

Sample results

Sample ident
XRF 34

Application	<Standardless>
Sequence	1 of 1
Measurement time	27-jan-2026 09:56:23
Position	12

Compound	SiO2	P2O5	K2O	CaO	TiO2	Fe2O3	Ta2O5	WO3	OsO4	PtO2
Conc	0,7	0,30	0,13	0,21	97,22	0,23	0,1	0,26	0,75	0,1
Unit	%	%	%	%	%	%	%	%	%	%

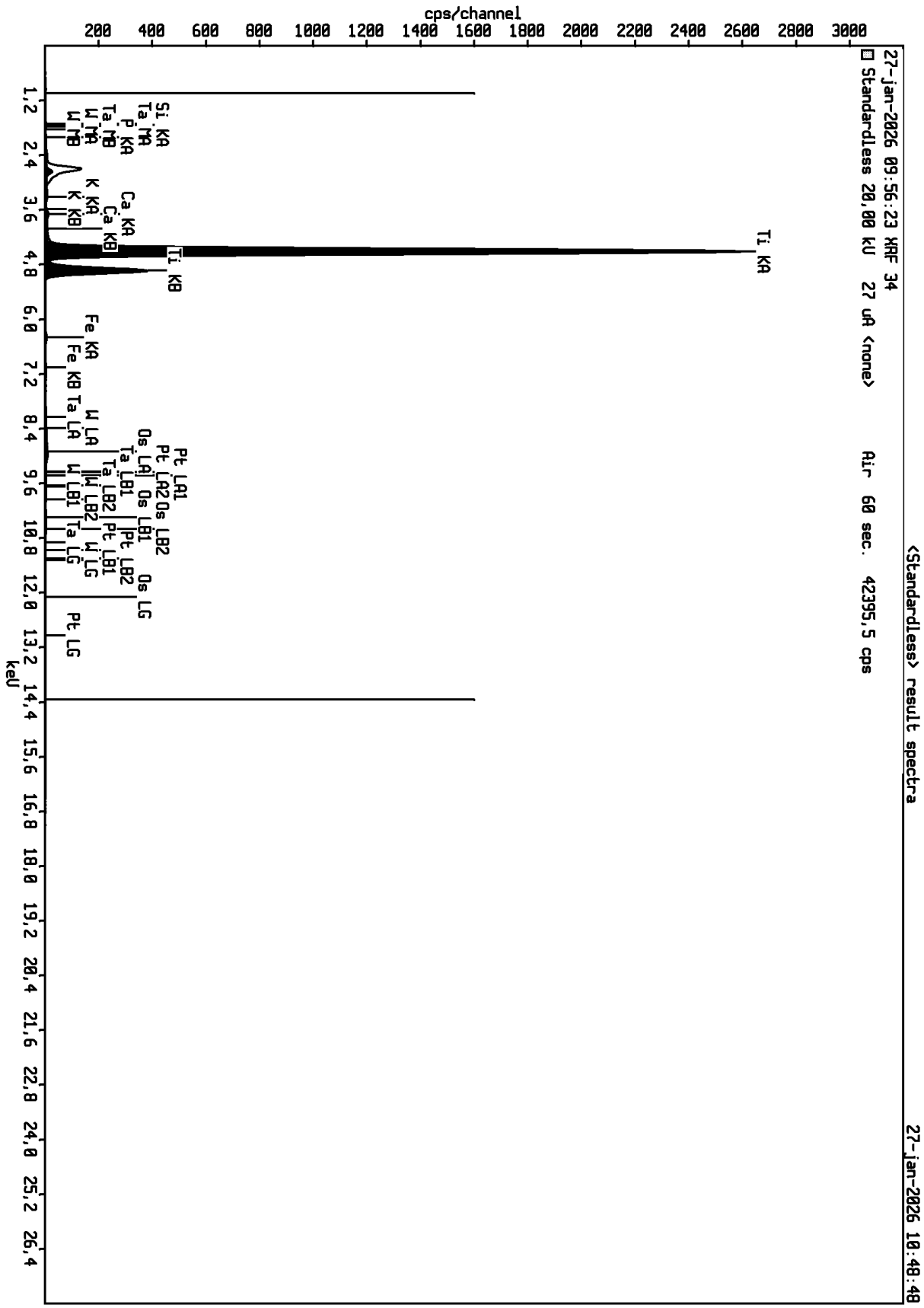
cps/channel
200 400 600 800 1000 1200 1400 1600 1800 2000 2200 2400 2600 2800 3000
27-jan-2026 09:56:23 XRF 34
Standardless 20,00 kV 27 uA <none> Air 60 sec. 42395,5 cps
<Standardless> result spectra
27-jan-2026 10:48:48
keV
1,2 2,4 3,6 4,8 6,0 7,2 8,4 9,6 10,8 12,0 13,2 14,4 15,6 16,8 18,0 19,2 20,4 21,6 22,8 24,0 25,2 26,4
Si KA
Ta MA
P KB
Ta MB
W MA
W MB
K KA
K KB
Ca KA
Ca KB
Ti KA
Ti KB
Fe KA
Fe KB
Ta LA
W LA
Pt LA1
Pt LA2
Os LA
Ta LB1
W LB2
W LB1
Os LB1
Os LB2
Ta LB2
Pt LB1
Pt LB2
Ta LG
W LG
Os LG
Pt LG

27-jan-2026 10:48:28

Sample results

Sample ident
XRF 34

Application	<Standardless>
Sequence	1 of 1
Measurement time	27-jan-2026 09:56:23
Position	12

Compound	Si	P	K	Ca	Ti	Fe	Ta	W	Os	Pt
Conc	0,4	0,18	0,15	0,22	96,99	0,29	0,2	0,38	1,0	0,2
Unit	%	%	%	%	%	%	%	%	%	%

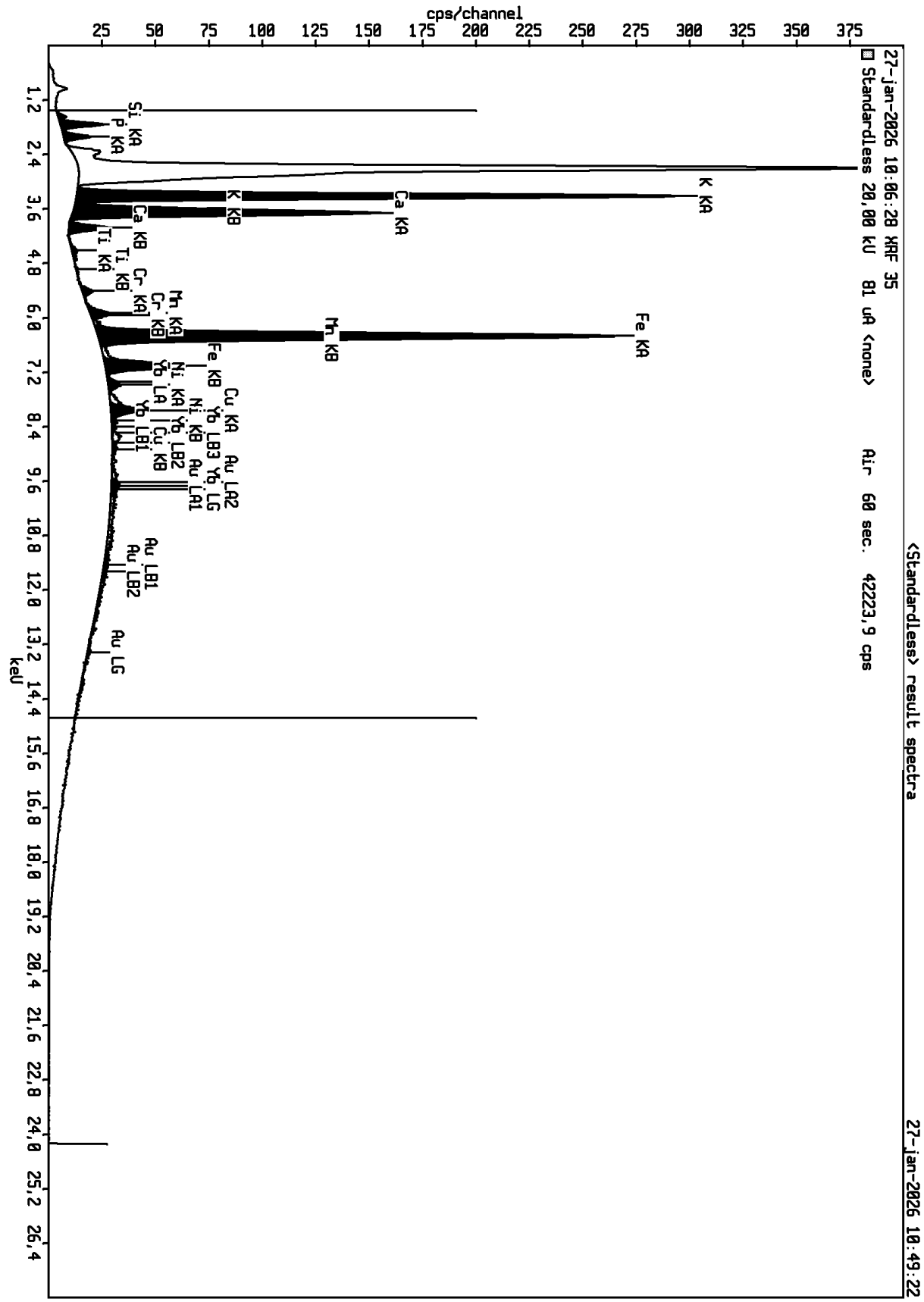
cps/channel
25 50 75 100 125 150 175 200 225 250 275 300 325 350 375
27-jan-2026 10:06:28 XRF 35
Standardless 20,00 kV 81 uA <none> Air 60 sec. 42223,9 cps
<Standardless> result spectra
27-jan-2026 10:49:22
keV
1,2 2,4 3,6 4,8 6,0 7,2 8,4 9,6 10,8 12,0 13,2 14,4 15,6 16,8 18,0 19,2 20,4 21,6 22,8 24,0 25,2 26,4
Si KA
P KA
K KA
K KB
Ca KA
Ca KB
Ti KA
Ti KB
Cr KA
Cr KB
Mn KA
Mn KB
Fe KA
Fe KB
Ni KA
Ni KB
Cu KA
Cu KB
Yb LA
Yb LB1
Yb LB2
Yb LB3
Yb LG
Au LA1
Au LA2
Au LB1
Au LB2
Au LG

27-jan-2026 10:48:56

Sample results

Sample ident
XRF 35

Application	<Standardless>
Sequence	1 of 1
Measurement time	27-jan-2026 10:06:28
Position	2

Compound	Si	P	K	Ca	Ti	Cr	Mn	Fe	Ni	Cu	Yb	Au
Conc	10	2,9	37,9	24,5	0,31	0,40	0,73	19,0	0,3	1,1	0,9	1,6
Unit	%	%	%	%	%	%	%	%	%	%	%	%

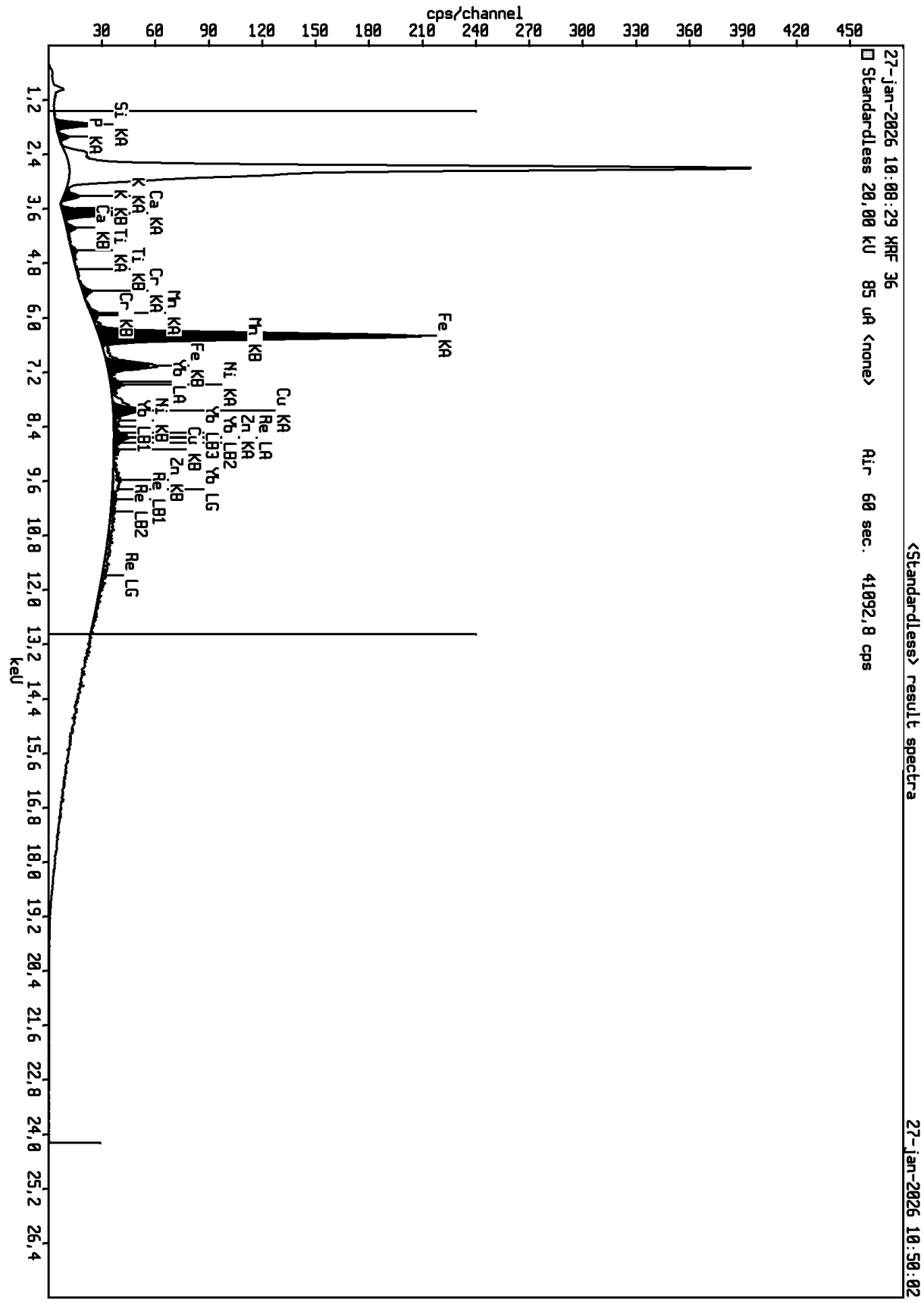
cps/channel
30 60 90 120 150 180 210 240 270 300 330 360 390 420 450
27-jan-2026 10:00:29 XRF 36
Standardless 20,00 kV 85 uA <none> Air 60 sec. 41092,8 cps
<Standardless> result spectra
27-jan-2026 10:50:02
keV
1,2 2,4 3,6 4,8 6,0 7,2 8,4 9,6 10,8 12,0 13,2 14,4 15,6 16,8 18,0 19,2 20,4 21,6 22,8 24,0 25,2 26,4
Si KA
P KA
K KA
K KB
Ca KA
Ca KB
Ti KA
Ti KB
Cr KA
Cr KB
Mn KA
Mn KB
Fe KA
Fe KB
Ni KA
Ni KB
Cu KA
Cu KB
Zn KA
Zn KB
Re LA
Re LB1
Re LB2
Re LG
Yb LA
Yb LB1
Yb LB2
Yb LB3
Yb LG

27-jan-2026 10:49:44

Sample results

Sample ident
XRF 36

Application	<Standardless>
Sequence	1 of 1
Measurement time	27-jan-2026 10:08:29
Position	3

Compound	Si	P	K	Ca	Ti	Cr	Mn	Fe	Ni	Cu	Zn	Yb	Re
Conc	36	5,7	3,6	12,3	0,65	0,72	0,68	28,5	1,0	3,3	0,7	2	4
Unit	%	%	%	%	%	%	%	%	%	%	%	%	%

L.4.3 UV-DRS

UIN MAULANA MALIK IBRAHIM MALANG

Settings information

Item	Value
Workbook file	D:\UV PADAT\2026\26-01-2026 sampel Hanik\26.iwbk
Accessories	Accessory: ISA-220 Integrating Sphere Accessory Accessory: ISA-220 Integrating Sphere Accessory
Software	INSIGHT: 2.1.175
Firmware	3.0.0.109
Application	Scan - Scan
Method Description	sampel Ika
Data Format	%Reflectance
Smooth Level	None
Derivative Order	None
Start Wavelength	800.00 nm
Stop Wavelength	200.00 nm
Scan Speed	120.00 nm/min
Data Interval	0.50 nm
Integration Time	0.250 sec
Bandwidth	1 nm
Baseline Correction	100 %T
Result Type	Peak Pick

#	Sample ID	User Name	Date and Time
1	sampel TiO	ASUS	1/26/2026 9:43:08 AM

Peaks:

nm	%R
326.993	22.428

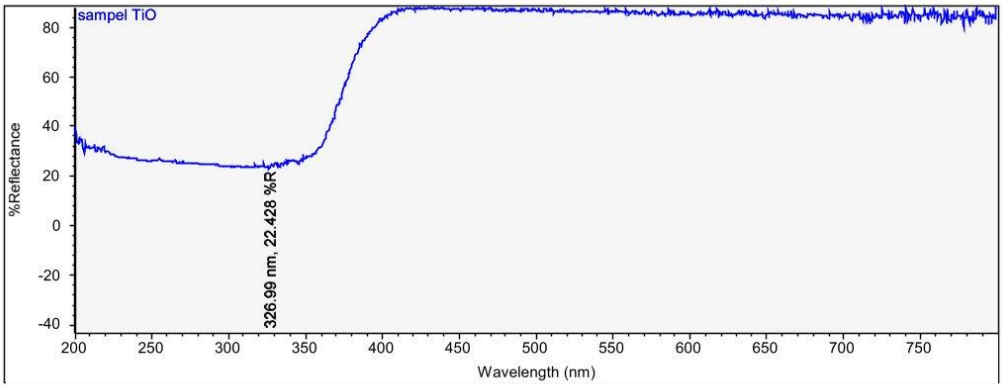

Settings information

Item	Value
Workbook file	D:\UV PADAT\2026\26-01-2026 sampel Hanik\26.iwbk
Accessories	Accessory: ISA-220 Integrating Sphere Accessory Accessory: ISA-220 Integrating Sphere Accessory
Software	INSIGHT: 2.1.175
Firmware	3.0.0.109
Application	Scan - Scan
Method Description	sampel Ika
Data Format	%Reflectance
Smooth Level	None
Derivative Order	None
Start Wavelength	800.00 nm
Stop Wavelength	200.00 nm
Scan Speed	120.00 nm/min
Data Interval	0.50 nm
Integration Time	0.250 sec
Bandwidth	1 nm
Baseline Correction	100 %T
Result Type	Peak Pick

#	Sample ID	User Name	Date and Time
2	sampel TiO KATKS	ASUS	1/26/2026 9:52:19 AM

Peaks:

nm	%R
325.340	21.516

UIN MAULANA MALIK IBRAHIM MALANG

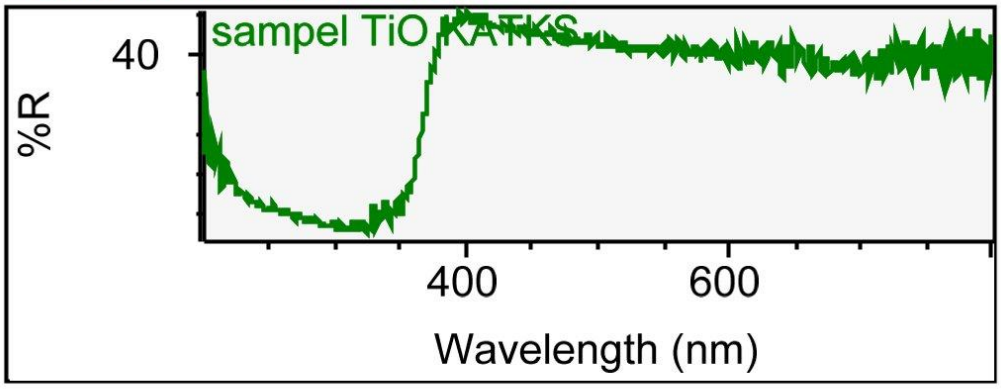

L.4.4 FTIR

FTIR Model : IRSpirit - T

SHIMADZU

12/02/2026 15:09:13

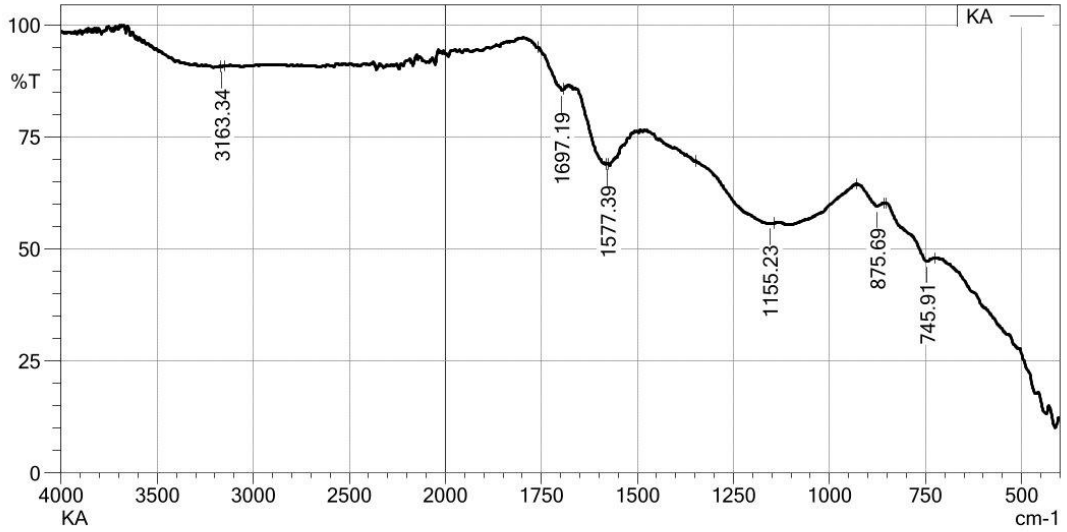

	Item	Value
	Acquired Date&Time	12/02/2026 15:04:22
	Filename	G:\FILES 2025\S-3\Erwan\12 feb\KA.ispd
	Measure Parameter File	
	Report Template	
	Spectrum name	KA
	Sample name	KA
	Sample ID	KA
	Option	
	Comment	KA
	No. of Scans	10
	Resolution	4 [cm-1]
	Apodization	Happ-Genzel

	Peak	Intensity	Corr. Intensity	Base (H)	Base (L)	Area	Corr. Area	Comment
1	745.91	47.16	2.71	852.87	725.94	5997.811	167.956	
2	875.69	59.45	1.79	929.89	858.58	2738.184	51.861	
3	1155.23	55.64	0.79	1349.20	1145.25	7858.060	246.009	
4	1577.39	68.90	0.04	1580.24	1575.96	132.956	0.135	
5	1697.19	85.28	1.23	1758.52	1691.49	679.720	31.778	
6	3163.34	90.57	0.18	3170.47	3149.08	199.241	1.567	

FTIR Model : IRSpirit - T

SHIMADZU

12/02/2026 15:12:37

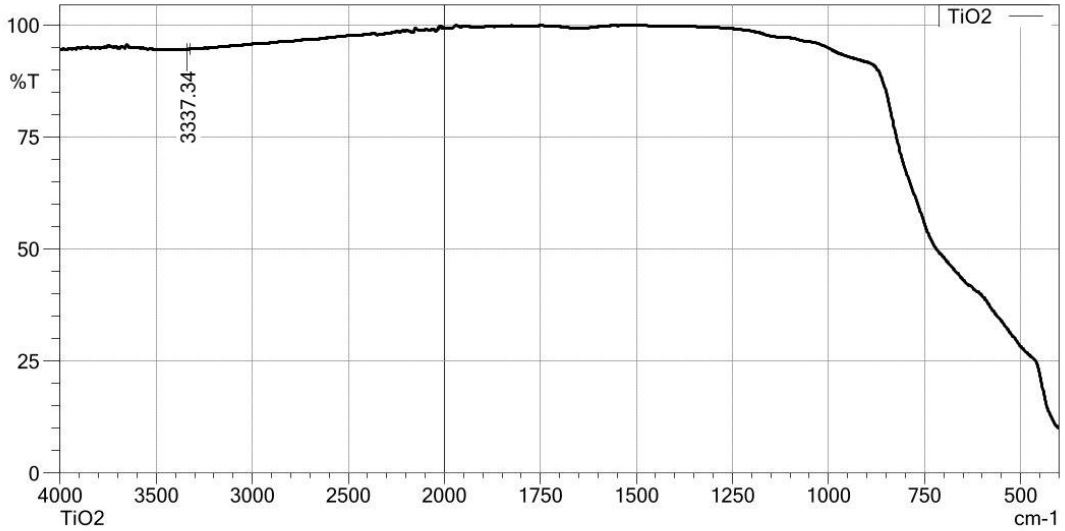

	Item	Value
	Acquired Date&Time	12/02/2026 14:57:30
	Filename	G:\FILES 2025\S-3\Erwan\12 feb\TiO2.ispd
	Measure Parameter File	
	Report Template	
	Spectrum name	TiO2
	Sample name	TiO2
	Sample ID	TiO2
	Option	
	Comment	TiO2
	No. of Scans	10
	Resolution	4 [cm-1]
	Apodization	Happ-Genzel

	Peak	Intensity	Corr. Intensity	Base (H)	Base (L)	Area	Corr. Area	Comment
1	3337.34	94.51	0.01	3338.76	3323.07	85.461	0.037	

FTIR Model : IRSpirit - T

SHIMADZU

12/02/2026 15:10:18

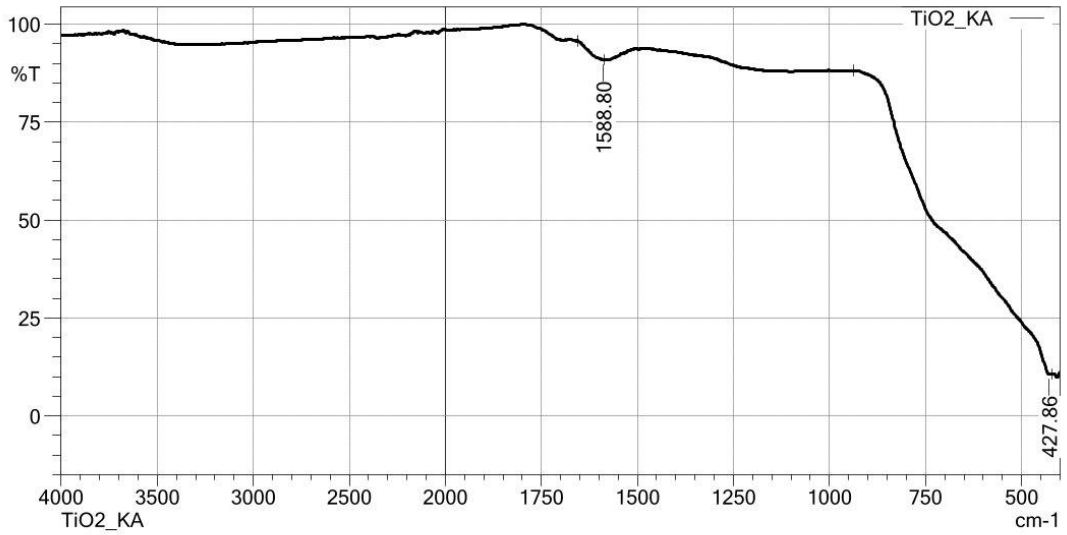

	Item	Value
	Acquired Date&Time	12/02/2026 15:01:40
	Filename	G:\FILES 2025\S-3\Erwan\12 feb\TiO2_KA.ispd
	Measure Parameter File	
	Report Template	
	Spectrum name	TiO2_KA
	Sample name	TiO2_KA
	Sample ID	TiO2_KA
	Option	
	Comment	TiO2_KA
	No. of Scans	10
	Resolution	4 [cm-1]
	Apodization	Happ-Genzel

	Peak	Intensity	Corr. Intensity	Base (H)	Base (L)	Area	Corr. Area	Comment
1	427.86	10.67	0.92	937.02	422.16	26357.240	339.780	
2	1588.80	90.93	0.24	1655.83	1585.95	498.307	34.959	

L.4.4 EDX

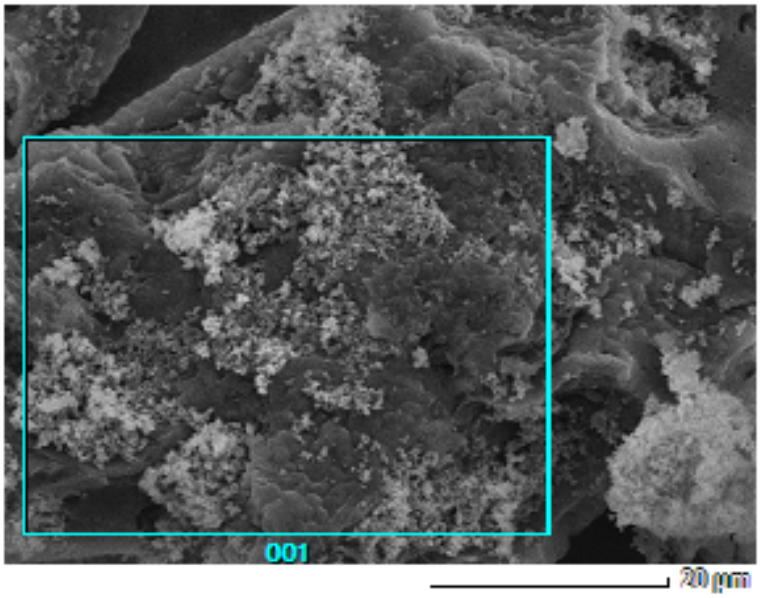

Title : IMG1[1/1]

Instrument : 6510 (LA)

Volt : 15.00 kV

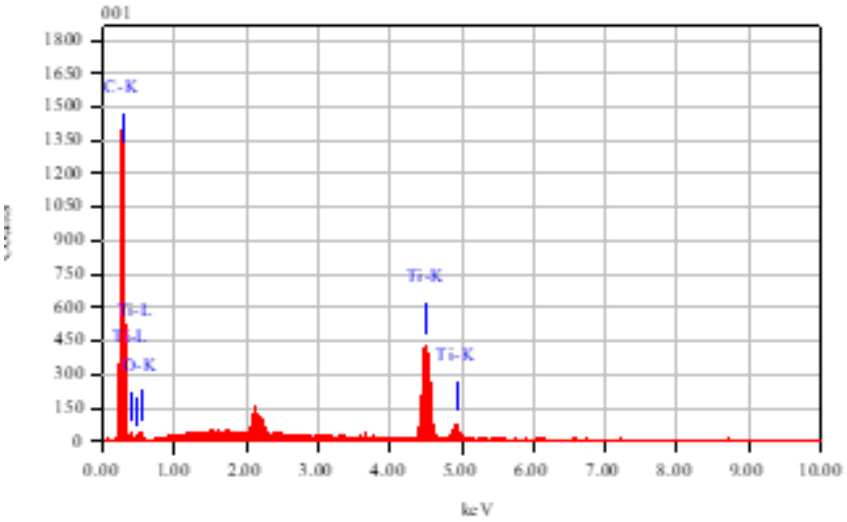

Acquisition Parameter

Instrument : 6510 (LA)

Acc. Voltage : 15.0 kV

Probe Current: 1.00000 nA

PHA mode : T3

Real Time : 31.35 sec

AF Method Standardless Quantitative Analysis

itting Coefficient : 0.2945

lement	(keV)	Mass%	Error%	Atom%	Compound	Mass%	Cation	K
C K	0.277	67.73	0.05	84.42				66.3347
O K	0.525	8.81	0.49	8.25				3.7309
i K	4.508	23.45	0.28	7.33				29.9344
otal		100.00		100.00				

Appendix 5 Data Calculation Results

100

Calibration Curve Equation

Y = 0.0072 + 0.00833x

x = (Y - 0.0072) - 0.00833

A. MASS VARIATION

A. MASS VARIATION										
NAME	ABSORBANTION		CONSENTRATION		% ADSORBTION	% DEGRADATION	% REMEDIATION	AVERAGE	STDV	%RSD
	Dark/control	Iridiation	Gelap	Iridiasi						
mass 10 mg	0.1722		19.80792317							
A	0.1704	0.1260	19.59183673	14.26170468	1.090909091	27.20588235	28		0.4720534	0.017270246
B	0.1693	0.1276	19.45978391	14.45378151	1.757575758	25.7248612	27.03030303	27.3333333		
C	0.1688	0.1277	19.3997599	14.46578631	2.060606061	25.43316832	26.96969697			
mass 20 mg	0.1791		20.6362545							
A	0.1661	0.0958	19.07563025	10.6362545	7.562536358	44.24166142	48.45840605		0.3887907	0.008042494
B	0.1624	0.0953	18.63145258	10.57623049	9.714950553	43.23453608	48.74927283	48.3420593		
C	0.1629	0.0969	18.69147659	10.76830732	9.42408377	42.38921002	47.81849913			
mass 30 mg	0.1684		19.3517407							
A	0.1501	0.0351	17.15486194	3.349339736	11.35235732	80.47585724	82.69230769		1.31693	0.015760142
B	0.1544	0.0353	17.67106843	3.37334934	8.684863524	80.91032609	82.56823821	83.560794		
C	0.1529	0.0307	17.4909964	2.821128451	9.615384615	83.87096774	85.42183623			
mass 40 mg	0.1605		18.40336134							
A	0.1333	0.0811	15.13805522	8.871548619	17.74298761	41.39571768	51.79386823		1.3861602	0.025935521
B	0.1366	0.0759	15.53421369	8.24729892	18.95321174	46.90880989	55.18590998	53.4464014		
C	0.1452	0.0787	16.56662665	8.583433373	11.82380216	48.1884058	53.35942596			
50 mg	0.1685		19.3637455							
A	0.1358	0.1048	15.43817527	11.71668667	15.31308122	24.10575428	36.33398565		0.3853021	0.010516347
B	0.1306	0.1047	14.81392557	11.70468187	23.2503888	20.98865478	36.39921722	36.6383997		
C	0.139	0.1035	15.82232893	11.56062425	17.42301459	26.93474962	37.18199609			

1. Mass 10 mg

C0 = (0.1722 - 0.0072) - 0.00833 = 0.1650 - 0.00833 = 19.8079 ppm

Ct1 = (0.1260 - 0.0072) - 0.00833 = 14.2617 ppm

Ct2 = (0.1276 - 0.0072) - 0.00833 = 14.4538 ppm

Ct3 = (0.1277 - 0.0072) - 0.00833 = 14.4658 ppm

%R1 = ((19.8079 - 14.2617) - 19.8079) ×100% = 28.00%

%R2 = ((19.8079 - 14.4538) - 19.8079) ×100% = 27.03%

%R3 = ((19.8079 - 14.4658) - 19.8079) ×100% = 26.97%

Σ = 27.33%

2. Mass 20 mg

C0 = (0.1791 - 0.0072) - 0.00833 = 0.1719 - 0.00833 = 20.6363 ppm

Ct1 = (0.0924 - 0.0072) - 0.00833 = 10.2281 ppm

Ct2 = (0.0949 - 0.0072) - 0.00833 = 10.5282 ppm

Ct3 = (0.0929 - 0.0072) - 0.00833 = 10.2881 ppm

%R1 = ((20.6363 - 10.2281) - 20.6363) ×100% = 50.44%

%R2 = ((20.6363 - 10.5282) - 20.6363) ×100% = 48.99%

%R3 = ((20.6363 - 10.2881) - 20.6363) ×100% = 50.15%

Σ = 49.86%

3. Mass 30 mg

C0 = (0.1684 - 0.0072) - 0.00833 = 0.1612 - 0.00833 = 19.3517 ppm

Ct1 = (0.0351 - 0.0072) - 0.00833 = 3.3493 ppm

Ct2 = (0.0353 - 0.0072) - 0.00833 = 3.3733 ppm

Ct3 = (0.0307 - 0.0072) - 0.00833 = 2.8211 ppm

%R1 = ((19.3517 - 3.3493) - 19.3517) ×100% = 82.69%

%R2 = ((19.3517 - 3.3733) - 19.3517) ×100% = 82.57%

%R3 = ((19.3517 - 2.8211) - 19.3517) ×100% = 85.42%

Σ = 83.56%

4. Mass 40 mg

C0 = (0.1605 - 0.0072) - 0.00833 = 0.1533 - 0.00833 = 18.4034 ppm

Ct1 = (0.0811 - 0.0072) - 0.00833 = 8.8715 ppm

Ct2 = (0.0759 - 0.0072) - 0.00833 = 8.2473 ppm

Ct3 = (0.0787 - 0.0072) - 0.00833 = 8.5834 ppm

%R1 = ((18.4034 - 8.8715) - 18.4034) ×100% = 51.79%

%R2 = ((18.4034 - 8.2473) - 18.4034) ×100% = 55.18%

%R3 = ((18.4034 - 8.5834) - 18.4034) ×100% = 53.36%

Σ = 53.44%

5. Mass 50 mg

C0 = (0.1685 - 0.0072) - 0.00833 = 0.1613 - 0.00833 = 19.3637 ppm

Ct1 = (0.1048 - 0.0072) - 0.00833 = 11.7167 ppm

Ct2 = (0.1047 - 0.0072) - 0.00833 = 11.7047 ppm

Ct3 = (0.1035 - 0.0072) - 0.00833 = 11.5606 ppm

%R1 = ((19.3637 - 11.7167) - 19.3637) ×100% = 39.49%

%R2 = ((19.3637 - 11.7047) - 19.3637) ×100% = 39.55%

%R3 = ((19.3637 - 11.5606) - 19.3637) ×100% = 40.29%

Σ = 39.78%

B. CONCENTRATION VARIATION

CONCENTRATION VARIATIONi										
NAME	ABSORBANTION		CONSENTRATION		% ADSORBTION	% DEGRADATION	% REMEDIATION	AVERAGE	STDV	%RSD
	Dark/control	Iridiation	Gelap	Iridiasi						
10 pm	0.0977		10.86434574	10.86434574						
A	0.0924	0.0157	10.22809124	1.020408163	5.856353591	90.02347418	90.60773481		1.1774856	0.01306446
B	0.0949	0.0151	10.52821128	0.948379352	3.093922652	90.99201824	91.27071823	90.1289134		
e	0.0929	0.0176	10.28811525	1.2484994	5.303867403	87.86464411	88.50828729			
20 ppm	0.1684		19.3517407	19.3517407	0					
A	0.1586	0.0351	18.17527011	3.349339736	6.079404467	81.57199472	82.69230769		1.31693	0.015760142
b	0.1501	0.0353	17.15486194	3.37334934	11.35235732	80.33589923	82.56823821			
d	0.1596	0.0307	18.29531813	2.821128451	5.459057072	84.58005249	85.42183623	83.560794		
30 ppm	0.2467		28.7515006	28.7515006	0					
A	0.2142	0.0674	24.84993998	7.226890756	13.56993737	70.9178744	74.86430063		1.6701461	0.021822149
b	0.2187	0.0594	25.39015606	6.266506603	11.69102296	75.31914894	78.2045929	76.5344468		
c	0.223	0.0515	25.90636255	5.318127251	9.895615866	79.47173309	81.50313152			
40 ppm	0.3670		43.19327731	43.19327731	0					
A	0.2899	0.1658	33.93757503	19.03961585	21.42857143	43.89812522	55.91995553		1.8348203	0.032036638
B	0.2804	0.1516	32.79711885	17.33493397	24.06892718	47.14494876	59.86659255	57.2725588		
C	0.2815	0.1654	32.92917167	18.99159664	23.76320178	42.32592052	56.0311284			
50 ppm	0.3933		46.35054022	46.35054022	0					
A	0.2687	0.1959	31.39255702	22.65306122	32.27143227	27.83938815	51.12665113		1.1074259	0.022343345
B	0.2716	0.2053	31.74069628	23.78151261	31.52033152	25.07564297	48.69204869	49.5640162		
C	0.2943	0.2046	34.46578631	23.69747899	25.64102564	31.24346917	48.87334887			

1. 10 ppm

C0 = (0.0977 - 0.0072) - 0.00833 = 0.0905 - 0.00833 = 10.8643 ppm

Ct1 = (0.0157 - 0.0072) - 0.00833 = 1.0204 ppm

Ct2 = (0.0151 - 0.0072) - 0.00833 = 0.9484 ppm

Ct3 = (0.0176 - 0.0072) - 0.00833 = 1.2485 ppm

%R1 = ((10.8643 - 1.0204) - 10.8643) ×100% = 90.61%

%R2 = ((10.8643 - 0.9484) - 10.8643) ×100% = 91.27%

%R3 = ((10.8643 - 1.2485) - 10.8643) ×100% = 88.51%

Σ = 90.13%

2. 20 ppm

C0 = (0.1684 - 0.0072) - 0.00833 = 0.1612 - 0.00833 = 19.3517 ppm

Ct1 = (0.0351 - 0.0072) - 0.00833 = 3.3493 ppm

Ct2 = (0.0353 - 0.0072) - 0.00833 = 3.3733 ppm

Ct3 = (0.0307 - 0.0072) - 0.00833 = 2.8211 ppm

%R1 = ((19.3517 - 3.3493) - 19.3517) ×100% = 82.69%

%R2 = ((19.3517 - 3.3733) - 19.3517) ×100% = 82.57%

%R3 = ((19.3517 - 2.8211) - 19.3517) ×100% = 85.42%

Σ = 83.56%

3. 30 ppm

C0 = (0.2467 - 0.0072) - 0.00833 = 0.2395 - 0.00833 = 28.7515 ppm

Ct1 = (0.0674 - 0.0072) - 0.00833 = 7.2269 ppm

Ct2 = (0.0594 - 0.0072) - 0.00833 = 6.2665 ppm

Ct3 = (0.0515 - 0.0072) - 0.00833 = 5.3181 ppm

%R1 = ((28.7515 - 7.2269) - 28.7515) ×100% = 74.86%

%R2 = ((28.7515 - 6.2665) - 28.7515) ×100% = 78.20%

%R3 = ((28.7515 - 5.3181) - 28.7515) ×100% = 81.50%

Σ = 78.19%

4. 40 ppm

C0 = (0.3670 - 0.0072) - 0.00833 = 0.3598 - 0.00833 = 43.1933 ppm

Ct1 = (0.1658 - 0.0072) - 0.00833 = 19.0396 ppm

Ct2 = (0.1516 - 0.0072) - 0.00833 = 17.3349 ppm

Ct3 = (0.1654 - 0.0072) - 0.00833 = 18.9916 ppm

%R1 = ((43.1933 - 19.0396) - 43.1933) ×100% = 55.92%

%R2 = ((43.1933 - 17.3349) - 43.1933) ×100% = 59.87%

%R3 = ((43.1933 - 18.9916) - 43.1933) ×100% = 56.03%

Σ = 57.27%

5. 50 ppm

C0 = (0.3933 - 0.0072) - 0.00833 = 0.3861 - 0.00833 = 46.3505 ppm

Ct1 = (0.1959 - 0.0072) - 0.00833 = 22.6531 ppm

Ct2 = (0.2053 - 0.0072) - 0.00833 = 23.7815 ppm

Ct3 = (0.2046 - 0.0072) - 0.00833 = 23.6975 ppm

%R1 = ((46.3505 - 22.6531) - 46.3505) ×100% = 51.13%

%R2 = ((46.3505 - 23.7815) - 46.3505) ×100% = 48.69%

%R3 = ((46.3505 - 23.6975) - 46.3505) ×100% = 48.87%

Σ = 49.56%

C. EFFECTIVENESS TEST

C. EFFECTIVENESS TEST										
NAME	ABSORBANTION		CONSENTRATION		% ADSORBTION	% DEGRADATION	% REMEDIATION	AVERAGE	STDV	%RSD
	Dark/control	Iridiation	Gelap	Iridiasi						
TiO2	0.0786		8.571428571							
A	0.0777	0.0307	8.463385354	2.821128451	1.260504202	66.66666667	67.08683473	68.1605976	1.4206465	0.020842636
B	0.0764	0.0285	8.307322929	2.557022809	3.081232493	69.21965318	70.16806723			
C	0.0783	0.0306	8.535414166	2.809123649	0.420168067	67.08860759	67.22689076			
AC	0.0953		10.57623049							
A	0.0739	0.073	8.007202881	7.899159664	24.29057889	1.349325337	25.31214529	27.9606508	1.875068	0.067060956
B	0.0736	0.0694	7.971188475	7.466986795	24.63110102	6.325301205	29.3984109			
C	0.0719	0.0696	7.767106843	7.490996399	26.56072645	3.554868624	29.17139614			
TiO2/AC	0.0977		10.86434574	10.86434574						
A	0.0924	0.0157	10.22809124	1.020408163	5.856353591	90.02347418	90.60773481		1.1774856	0.01306446
B	0.0949	0.0151	10.52821128	0.948379352	3.093922652	90.99201824	91.27071823	90.1289134		
e	0.0929	0.0176	10.28811525	1.2484994	5.303867403	87.86464411	88.50828729			
RBBR	0.1034		11.54861945							
A	0.1021	0.0977	11.39255702	10.86434574	1.351351351	4.636459431	5.925155925		0.4491158	0.070827767
B	0.1023	0.0967	11.41656663	10.74429772	1.143451143	5.888538381	6.964656965	6.34095634		
C	0.1022	0.0975	11.40456182	10.84033613	1.247401247	4.947368421	6.133056133			

1. TiO_2

C0 = (0.0977 - 0.0072) - 0.00833 = 0.0905 - 0.00833 = 10.8643 ppm

Ct1 = (0.0307 - 0.0072) - 0.00833 = 2.8211 ppm

Ct2 = (0.0285 - 0.0072) - 0.00833 = 2.5570 ppm

Ct3 = (0.0306 - 0.0072) - 0.00833 = 2.8091 ppm

%R1 = ((10.8643 - 2.8211) - 10.8643) ×100% = 74.03%

%R2 = ((10.8643 - 2.5570) - 10.8643) ×100% = 76.46%

%R3 = ((10.8643 - 2.8091) - 10.8643) ×100% = 74.14%

Σ = 74.88%

2. AC

C0 = (0.0977 - 0.0072) - 0.00833 = 0.0905 - 0.00833 = 10.8643 ppm

Ct1 = (0.0371 - 0.0072) - 0.00833 = 3.5894 ppm

Ct2 = (0.0353 - 0.0072) - 0.00833 = 3.3733 ppm

Ct3 = (0.0354 - 0.0072) - 0.00833 = 3.3854 ppm

%R1 = ((10.8643 - 3.5894) - 10.8643) ×100% = 66.96%

%R2 = ((10.8643 - 3.3733) - 10.8643) ×100% = 68.95%

%R3 = ((10.8643 - 3.3854) - 10.8643) ×100% = 68.84%

Σ = 68.25%

3. TiO_2-AC

C0 = (0.0977 - 0.0072) - 0.00833 = 0.0905 - 0.00833 = 10.8643 ppm

Ct1 = (0.0157 - 0.0072) - 0.00833 = 1.0204 ppm

Ct2 = (0.0151 - 0.0072) - 0.00833 = 0.9484 ppm

Ct3 = (0.0176 - 0.0072) - 0.00833 = 1.2485 ppm

%R1 = ((10.8643 - 1.0204) - 10.8643) ×100% = 90.61%

%R2 = ((10.8643 - 0.9484) - 10.8643) ×100% = 91.27%

%R3 = ((10.8643 - 1.2485) - 10.8643) ×100% = 88.51%

Σ = 90.13%

4. RBBR

C0 = (0.1034 - 0.0072) - 0.00833 = 0.0962 - 0.00833 = 11.5486 ppm

Ct1 = (0.0977 - 0.0072) - 0.00833 = 10.8643 ppm

Ct2 = (0.0967 - 0.0072) - 0.00833 = 10.7443 ppm

Ct3 = (0.0975 - 0.0072) - 0.00833 = 10.8403 ppm

%R1 = ((11.5486 - 10.8643) - 11.5486) ×100% = 5.93%

%R2 = ((11.5486 - 10.7443) - 11.5486) ×100% = 6.96%

%R3 = ((11.5486 - 10.8403) - 11.5486) ×100% = 6.13%

Σ = 6.34%

D. Crystallite Size Calculation

TiO_2

2θ (°)	FWHM (°)	θ	Rad	1/β	cos θ	ln(β)	ln(sec θ)	sinθ	4sinθ	βcosθ
		2θ/2	B2*PI()/180	1/D2	COS(RADIANS(C2))	LN(D2)	LN(SEC(RADIANS(C2)))	SIN(RADIANS(C2))		D2*COS(RADIANS(C2))
25.414	0.236	12.707	0.004118977	242.7787268	0.975507677	-5.49215	0.024797249	0.219965387	0.879861547	0.004018094
37.018	0.17	18.509	0.00296706	337.0339971	0.948273801	-5.82018	0.053111998	0.317453615	1.269814459	0.002813585
37.918	0.23	18.959	0.004014257	249.1120848	0.945751305	-5.5179	0.055775635	0.324891472	1.299565889	0.003796489
38.65	0.23	19.325	0.004014257	249.1120848	0.943656648	-5.5179	0.0579929	0.330926172	1.323704688	0.003788081
48.161	0.215	24.0805	0.003752458	266.4919977	0.912973095	-5.58534	0.091048867	0.408019763	1.632079054	0.003425893
54.023	0.225	27.0115	0.003926991	254.6479089	0.890915385	-5.53988	0.115505823	0.454169327	1.816677308	0.003498617
55.192	0.225	27.596	0.003926991	254.6479089	0.886235921	-5.53988	0.120772087	0.463234165	1.852936661	0.00348024
62.234	0.16	31.117	0.002792527	358.098622	0.856113788	-5.88081	0.155351981	0.516787366	2.067149463	0.002390721
62.812	0.21	31.406	0.003665191	272.8370453	0.853496233	-5.60887	0.158414151	0.521099013	2.08439605	0.003128227
68.881	0.23	34.4405	0.004014257	249.1120848	0.824713941	-5.5179	0.192718692	0.565550101	2.262200402	0.003310614
70.405	0.228	35.2025	0.003979351	251.2972786	0.817119746	-5.52664	0.201969627	0.57646797	2.305871881	0.003251606
75.167	0.221	37.5835	0.003857178	259.2569209	0.79246532	-5.55782	0.232606535	0.609916976	2.439667902	0.00305668
76.138	0.13	38.069	0.002268928	440.7367655	0.787268755	-6.08845	0.239185595	0.616610012	2.466440048	0.001786256
80.891	0.17	40.4455	0.00296706	337.0339971	0.761023379	-5.82018	0.2730912	0.648724453	2.594897812	0.002258002
82.27	0.2	41.135	0.003490659	286.4788976	0.753161684	-5.65766	0.283475354	0.657835449	2.631341795	0.00262903
82.791	0.23	41.3955	0.004014257	249.1120848	0.750163007	-5.5179	0.287464754	0.66125295	2.645011799	0.003011347
83.269	0.22	41.6345	0.003839724	260.4353614	0.747398179	-5.56235	0.291157198	0.66437637	2.657505481	0.002869803
87.88	0.12	43.94	0.002094395	477.4648293	0.72006685	-6.16849	0.328411224	0.693904699	2.775618795	0.001508104

TiO_2-AC

2θ (°)	FWHM (°)	θ	Rad (β)	1/β	cos θ	ln(β)	ln(sec θ)	sinθ	4sinθ	βcosθ
		2θ/2	B2*PI()/180	1/D2	COS(RADIANS(C2))	LN(D2)	LN(SEC(RADIANS(C2)))	SIN(RADIANS(C2))		D2*COS(RADIANS(C2))
25.432	0.193	12.716	0.003368485	296.8693239	0.975473113	-5.693292055	0.024832681	0.220118616	0.880474466	0.003285867
37.035	0.154	18.5175	0.002687807	372.0505163	0.948226696	-5.919029642	0.053161675	0.317594291	1.270377162	0.00254865
37.908	0.169	18.954	0.002949606	339.0282811	0.945779654	-5.826083529	0.055745661	0.324808939	1.299235755	0.002789678
38.668	0.144	19.334	0.002513274	397.8873577	0.943604654	-5.986168944	0.058047999	0.331074397	1.324297589	0.002371537
48.149	0.152	24.0745	0.0026529	376.9459178	0.913015818	-5.932101723	0.091002073	0.407924155	1.63169662	0.00242214
53.993	0.165	26.9965	0.002879793	347.2471486	0.891034255	-5.85003677	0.115372406	0.45393607	1.815744282	0.002565994
55.174	0.153	27.587	0.002670354	374.482219	0.886308675	-5.925544323	0.120689997	0.46309495	1.8523798	0.002366758
62.204	0.158	31.102	0.00275762	362.6315159	0.856249054	-5.893387211	0.155193995	0.516563218	2.066252872	0.00236121
62.78	0.166	31.39	0.002897247	345.1552983	0.853641718	-5.843994456	0.158243708	0.520860651	2.083442605	0.002473211
68.842	0.184	34.421	0.003211406	311.390106	0.824906372	-5.741046486	0.192485388	0.565269385	2.261077541	0.002649109
70.383	0.174	35.1915	0.003036873	329.2860892	0.817230405	-5.796926945	0.201834211	0.576311084	2.305244336	0.002481825
74.16	0.16	37.08	0.002792527	358.098622	0.79779444	-5.880808429	0.225904309	0.602929542	2.411718167	0.002227862
75.127	0.177	37.5635	0.003089233	323.704969	0.792678173	-5.779832511	0.232337975	0.609640316	2.438561263	0.002448767
76.155	0.148	38.0775	0.002583087	387.1336454	0.787177271	-5.95876997	0.239301807	0.616726799	2.466907196	0.002033348
80.82	0.22	40.41	0.003839724	260.4353614	0.761425178	-5.562354698	0.272563368	0.648252805	2.593011219	0.002923663
82.33	0.19	41.165	0.003316126	301.5567343	0.752817139	-5.708958172	0.283932924	0.658229713	2.632918853	0.002496436
82.774	0.187	41.387	0.003263766	306.3945429	0.750261097	-5.724873627	0.287334003	0.661141653	2.644566614	0.002448676
83.21	0.31	41.605	0.005410521	184.8250952	0.747740149	-5.219409947	0.290699756	0.663991468	2.655965871	0.004045664

The crystallite size was calculated using the Scherrer equation:

$$D=\frac{K\,\lambda}{\beta\,\cos\theta}$$

Where:

D = crystallite size (nm)

K = Scherrer constant (0.9)

λ= X-ray wavelength (Cu Kα = 0.15406 nm)

β = Full Width at Half Maximum (FWHM) in radians

θ = diffraction angle (degrees)

A. TiO_2 Anatase

Given:

2θ = 25.414°

θ = 12.707°

FWHM = 0.236°

Conversion of FWHM to radians

β = 0.236 × π-180

β = 0.00412 rad

Calculation of cos θ

cos(12.707°) = 0.9755

Substitution into the Scherrer equation

D = (0.9 × 0.15406)-(0.00412 × 0.9755)

D = 0.138654 - 0.00402

D = 34.48 nm ≈ 34.5 nm

B. TiO_2-AC Composite

Given:

2θ = 25.432°

θ = 12.716°

FWHM = 0.193°

Conversion of FWHM to radians

β = 0.193 × π-180

β = 0.00337 rad

Calculation of cos θ

cos(12.716°) = 0.9754

Substitution into the Scherrer equation

D = (0.9 × 0.15406)-(0.00337 × 0.9754)

D = 0.138654 - 0.00329

D = 42.13 nm ≈ 42.1 nm

2. Monshi–Scherrer Calculation

Monshi–Scherrer equation:

ln(β) = ln(Kλ-D) + ln(sec θ)

A. TiO_2 Anatase

Intercept = -5.82018

Step 1. Exponential calculation

e^(-5.82018) = 0.00296

Step 2. Crystallite size calculation

D = (0.9 × 0.15406)-0.00296

D = 46.8 nm

B. TiO_2-AC Composite

Intercept = -5.53988

Step 1. Exponential calculation

e^(-5.53988) = 0.00393

Step 2. Crystallite size calculation

D = (0.9 × 0.15406)-0.00393

D = 35.3 nm

Final Results

Result of TiO2 Cristalinity Size	
Scherrer	Monshi-Scherrer
D=Kλ/β cos θ	lnβ=ln(cosθ1)+ln(DKλ)
32.8377751	34.28734523
Result of TiO2/AC Cristalinity Size	
Scherrer	Monshi-Scherrer
D=Kλ/β cos θ	lnβ=ln(cosθ1)+ln(DKλ)
40.1525406	54.26211808

E. ADSORPTION CAPACITY OF TiO_2-AC

Equation:

qe = ((C0 - Ce) × V) - m

Data:

C0 = 10.8643 mg-L

Ce1 = 10.2281 mg-L

Ce2 = 10.5282 mg-L

Ce3 = 10.2881 mg-L

V = 0.025 L

m = 0.03 g

qe1 = ((10.8643 - 10.2281) × 0.025) - 0.03 = (0.6362 × 0.025) - 0.03 = 0.0159 - 0.03 = 0.5302 mg-g

qe2 = ((10.8643 - 10.5282) × 0.025) - 0.03 = (0.3361 × 0.025) - 0.03 = 0.0084 - 0.03 = 0.2801 mg-g

qe3 = ((10.8643 - 10.2881) × 0.025) - 0.03 = (0.5762 × 0.025) - 0.03 = 0.0144 - 0.03 = 0.4802 mg-g

Average adsorption capacity = Σqe = (0.5302 + 0.2801 + 0.4802) - 3 = 1.2905 - 3 = 0.4302 mg-g

F. DEGRADATION CAPACITY OF TiO_2-AC

Equation:

qt = ((Ce - Ct) × V) - m

Data:

Ce1 = 10.2281 mg-L

Ce2 = 10.5282 mg-L

Ce3 = 10.2881 mg-L

Ct1 = 1.0204 mg-L

Ct2 = 0.9484 mg-L

Ct3 = 1.2485 mg-L

V = 0.025 L

m = 0.03 g

qt1 = ((10.2281 - 1.0204) × 0.025) - 0.03 = (9.2077 × 0.025) - 0.03 = 0.2302 - 0.03 = 7.6731 mg-g

qt2 = ((10.5282 - 0.9484) × 0.025) - 0.03 = (9.5798 × 0.025) - 0.03 = 0.2395 - 0.03 = 7.9832 mg-g

qt3 = ((10.2881 - 1.2485) × 0.025) - 0.03 = (9.0396 × 0.025) - 0.03 = 0.2260 - 0.03 = 7.5330 mg-g

Average degradation capacity = Σqt = (7.6731 + 7.9832 + 7.5330) - 3 = 23.1893 - 3 = 7.7298 mg-g

G. REMEDIATION CAPACITY OF TiO_2-AC

Equation:

qr = ((C0 - Ct) × V) - m

Data:

C0 = 10.8643 mg-L

Ct1 = 1.0204 mg-L

Ct2 = 0.9484 mg-L

Ct3 = 1.2485 mg-L

V = 0.025 L

m = 0.03 g

qr1 = ((10.8643 - 1.0204) × 0.025) - 0.03 = (9.8439 × 0.025) - 0.03 = 0.2461 - 0.03 = 8.2033 mg-g

qr2 = ((10.8643 - 0.9484) × 0.025) - 0.03 = (9.9159 × 0.025) - 0.03 = 0.2479 - 0.03 = 8.2633 mg-g

qr3 = ((10.8643 - 1.2485) × 0.025) - 0.03 = (9.6158 × 0.025) - 0.03 = 0.2404 - 0.03 = 8.0132 mg-g

Average remediation capacity =

Σqr = (8.2033 + 8.2633 + 8.0132) - 3 = 24.4798 - 3 = 8.1599 mg-g

Appendix 6 Documentation

Palm Shell Activated Carbon

Palm shells

Cleaned from fibers

Ground and oven-dried at 100°C for 3 hours

Calcined at 500°C for 3 hours

Calcined at 500°C for 3 hours

Sieved at 200 mesh

Soaked in 1 M HCl solution for 4 hours

Neutralized to normal pH

Dried in the oven

Final activated carbon from palm shells

Synthesis of TiO_2-Activated Carbon

TiO_2 powder and activated carbon

Added distilled water and stirred for 6 hours

Filtered

Oven-dried at 100°C

Calcined at 300°C for 3 hours

Final TiO_2-AC composite

Activity Test

1000 ppm of RBBR

Standard curve solution

Maximum wavelength determination solution

RBBR + TiO_2-AC before degradation

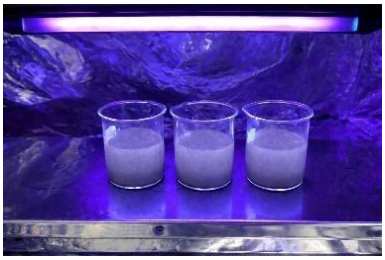

Photodegradation process

After photodegradation

Centrifuged

Filtered

Degradation results based on mass variation

Degradation results based on Concentration variation

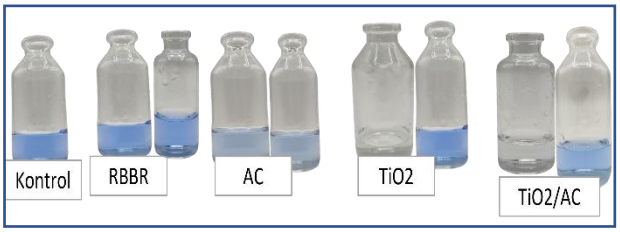

Effectiveness test results